

**Doctoral Dissertation**

**Development of Methods for Crop Growth Assessment**

**Using UAV Aerial Images**

**Ke Zhang**

Supervisor: Professor Dr. Sawahiko Shimada

Advisor: Professor Dr. Hiromu Okazawa

Associate Prof. Dr. Ayako Sekiyama

Professor Dr. Kiichiro Hayashi

20 March 2023

# Summary

## Chapter 1 Backgrounds and Objectives

Precision agriculture has been developed as a technology for more labor-saving, efficient, and precise farm management that makes full use of precise farm management plans based on sensing information and automatic control of agricultural machinery based on digital mapping development is emphasized. Spatial information about crop growth and soil conditions for each field or within a field is particularly important for promoting precision agriculture. Therefore, remote sensing by satellites and Unmanned aerial vehicles (UAVs) has been used as a method for spatially measuring crop growth and actual conditions of soil which plays a large role in precision agriculture. In the case of UAV, it is possible to achieve ultra-high resolution of several millimeters to several centimeters by appropriately selecting flight altitude and sensor specifications. Advantages to use for monitoring crop growth are UAVs filling a niche in observation scale, resolution and height between manned aerial platform and ground. Several authors have shown how to combine UAVs with lightweight sensors for crop monitoring. However, with the extremely high spatial resolution of UAV imagery, the difference of plant shapes between different crops gives significant influence of the observation result when monitoring plant height using UAV. Few studies have examined crops with different stomatal morphologies at the same time, in the same region, and under the same flight conditions. In particular, there have been no studies comparing monocotyledonous and dicotyledonous plants, which differ greatly in stomatal morphology and cultivation methods, under the same conditions. Moreover, for agricultural surveys, setting GCPs inside the crops is destructive for the growing plants and will cause disruptions to field management. It is necessary to acknowledge that in many surveying sites, only the outer edges of the subject area are available for GCP placement. Based on this reality, the current study aims to create a standard to evaluate the quality of GCP setting to provide a guideline for researchers or surveyors of UAV photogrammetry to decide the most optimal number and spatial configuration of GCPs without intruding into the subject area. To actually practice UAV remote sensing to agriculture, the problems in real sites of farmland need to be further discussed.

## **Chapter 2 Optimization of Ground Control Points Distribution for Unmanned Aerial Vehicle Photogrammetry in Farming Land**

Ground control point (GCP) is an important calibration factor when correcting position information during unmanned aerial vehicle (UAV) remote sensing. Studies of the optimal number and distribution shape of GCPs have been conducted worldwide in recent years. However, when conducting surveys at houses, construction sites, farming lands, forests, and some other locations, it is both difficult and destructive to install GCP inside the subject area. In many cases, it is only possible to install GCP at the outer edge around the area. Therefore, this study aims to suggest the optimal GCP distribution pattern, which can provide the highest accuracy, when only the outer edge of a particular area is available. In this research, 88 GCP patterns have been validated and compared at an 18 ha farm. Results show that the patterns with GCPs distributed evenly around the field provided the best calibration (RMSE = 0.15 m). If this kind of pattern is not achievable because of obstructions, patterns with GCPs distributed evenly around half of the field or forming an evenly distributed triangle can provide moderate accuracy (RMSE = 0.18 m and 0.43 m, respectively). Patterns with GCPs forming a straight line yielded the worst accuracy (RMSE = 2.10 m). This shows that GCP distributions of a two-dimensional shape, even if the surrounding area is small, are better calibrated than a long, straight line. These results strongly suggest that appropriate GCP distribution patterns in the study areas will provide satisfactory accuracy for constructing integrated monitoring systems of diverse resources.

## **Chapter 3 Monitoring of Crop Plant Height Based on DSM Data Obtained by Small UAV Considering Difference of Plant Shapes**

UAV is expected to be used in agricultural fields because it is cheaper than satellite and aerial photography and can acquire high-resolution aerial images at any time. Researches on crop height monitoring using digital surface models (DSM) based on UAV aerial images have been conducted for various crops around the world. However, there is no research that examines the difference in estimation accuracy for multiple crops with large differences in foliage morphology. While UAVs provide high-resolution aerial images, we cannot ignore the fact that structural differences in the details of the object to be photographed (such as the foliage morphology of crops in the case of crops) greatly affect the results of UAV photogrammetry. Therefore, in this study, we monitored the crop height of oat and reed canary grass, which are monocotyledonous plants, and potato and perilla, which are dicotyledonous plants, using DSM data by UAV, and compared the estimation accuracy. By doing so, we investigated the effect of foliage morphology on the estimation accuracy. As a

result, the highest estimation accuracy ( $R^2 = 0.97$ ,  $RMSE = 5$  cm) was obtained for perilla with ovate leaf blades and thick foliage. As a result of comparing the regression equations of the estimated crop height and the measured values over the entire period, the estimated values always kept a constant difference from the measured values for the monocotyledonous plants, while the estimated values for the dicotyledonous plants were lower than the measured value, approached the measured value as the crop grew, and eventually exceeded the measured value (when the crop height was 1 m or more). From these results, it was found that when estimating crop height using DSM data, it was necessary to correct the DSM value using a regression equation appropriate for the crop. In addition, this study provided the formulas for estimating the crop heights of the four common crops during the entire growing season, thereby accumulating basic data for crop growth monitoring using DSM in the future.

#### **Chapter 4 Comparison of DSM and 3D Point Clouds by UAV Imagery on Estimating Plant Height and Biomass Volume**

Plant biomass is considered as an important parameter for crop management and yield estimation, especially for grassland. Aerial photogrammetric techniques have been used for vegetation data gathering of the areas of dense vegetation fields with high research interest. Recent advances in computer vision include structure from motion and multi-view stereopsis (SfM-MVS) techniques, which can derive 3D data such as digital surface models (DSMs) and orthomosaic from overlapping photography taken from multiple angles. The difference between the DSMs of a planted field and the digital terrain model (DTM) has been referred to crop surface model (CSM). Ever since SfM-MVS has been adopted to derive plant height (PH) and above-ground biomass using CSMs in 2013, this method has become the most explored and verified approach to simulate the structure of crops all over the world. However, the complexity of crop structure is thought to be not well represented in DSMs because the DSMs have only one Z value at each 2D pixel. Besides, lacking a DTM representing the bare ground is another problem when adopting the CSM method. On the other hand, the 3D point cloud where DSMs are derived from UAV may provide the structure information in a faster and more detailed way. In this study, we compared DSM data and 3D point cloud data for estimating the crop height of reed canary grass and estimating the above-ground volume of the crop in an experimental field at Obihiro University of Agriculture and Veterinary Medicine. As a result, the 3D point cloud data obtained higher accuracy than the point cloud data in estimating the crop height ( $RMSE = 4$  cm,  $3$  cm,  $intercept = 8.8$ ,  $-0.16$ , respectively). It was found that the correction of the regression equation was unnecessary when estimating

the crop height. Therefore, it was found that 3D point cloud data is suitable when accurate crop height and lodging information is required. On the other hand, there was no significant difference between the DSM data and the 3D point cloud data for the above-ground volume estimates during the entire growth period. From this, it was found that the two types of data have the same performance in estimating the above-ground volume, and that the DSM data is appropriate in terms of practicality. It is believed that this research contributed to the practical use of UAV aerial photography in agriculture by proposing types of UAV aerial photography data for different purposes.

### **Chapter 5 Relationship between NDVI and Canopy Cover Sensed by Small UAV under Different Ground Resolution**

Canopy Cover (CC) is a significant indicator to describe the development of crops, and is used to estimate the evapotranspiration volume of crop leaves within crop simulation models. During the last three decades, monitoring of CC for crops using Normalized Difference Vegetation Index (NDVI) obtained from satellite sensor such as Landsat and Sentinel-2, has been studied world-widely. However, a few studies have estimated CC of crops using NDVI obtained from UAVs, and there is no research showing that the NDVI based on UAV imagery has the same linear regression relationship with CC as satellite imagery. One of the crucial advantages of UAV imagery is that it provides high resolution of less than 0.10m, while the resolution of satellite imagery is usually larger than 10m. Now that the UAV has become a popular method in agriculture science, it is necessary to prove the interchangeability of UAV and satellite imagery of monitoring CC.

In this study, RGB and multispectral images of a peanuts field located in the experimental field in Obihiro University of Agriculture and Veterinary Medicine were taken by small UAVs and multispectral camera. Orthomosaic and reflectance map of the farming field were constructed using the UAV imagery, and then were used to obtain CC and NDVI values with a GIS software. CC was calculated as the ratio of the green canopy area, which was extracted from the orthomosaic using a supervised classification tool within GIS. CC was compared with NDVI values under various resolutions of 0.50 m, 1.0 m, 2.5 m, 5.0 m, and 10 m.

The NDVI showed highly correlated linear relationship ( $y = ax + b$ ) with CC under each ground resolution from 0.10 m to 10 m ( $R^2$  of 0.88\*\*, 0.92\*\*, 0.94\*\*, 0.89\*\*, 0.93\*\*, respectively). The shapes of the regression equations of NDVI and CC closely resembled each other, with the slopes (a) of 1.16, 1.11, 1.09, 1.08 and 1.06, and the intercepts (b) of 0.247, 0.249, 0.250, 0.250 and 0.250, respectively. From the result of ANCOVA, the resolution of remote sensing imagery has not significant impact on the relationship between

NDVI and CC. Although with the increasing ground resolution, more irrelevant factors, such as soil and mulching seat got included within one pixel of the images, the regression equations stayed the same. This study demonstrated the possibility of using UAV multispectral imagery for CC monitoring with the same regression equations as satellite multispectral imagery. On the other hand, in each regression equation, the intercept was 0.25 even though the regression coefficient was close to 1.0. The reason for this is thought to be the low NDVI value of the plastic mulch sheets applied in the fields. From this, it was found that features other than crops and soil mixed in the same pixel had an adverse effect on obtaining an accurate relationship between NDVI and CC. In the future research, it is important to use the high-resolution characteristics of UAV aerial images and determine the features in the farmland in order to accurately measure the growth evaluation index of crops.

## **Chapter 6 Assessment of Three Automated Identification Methods for Ground Objects Based on UAV Imagery**

Identification and monitoring of diverse resources or wastes on ground is important for integrated resource management. Remote sensing application is of great significance for identification of ground objects due to its rapid and accurate assessment. Among remote sensing platforms, the unmanned aerial vehicle (UAV) with its high resolution and facility is the optimal tool to monitor ground objects accurately and efficiently. However, few studies have compared different classification methods using UAV imagery. This study compared three classification methods: A. NDVI threshold, B. RGB image-based machine learning, and C. object-based image analysis (OBIA). Method A was the least time-consuming and could identify vegetation and soil with high accuracy (user's accuracy > 0.80), but had poor performance at classifying dead vegetation, plastic, and metal (user's accuracy < 0.50). Both Methods B and C were time- and labor-consuming, but had very high accuracy in separating vegetation, soil, plastic, and metal (user's accuracy  $\geq 0.70$  for all classes). Furthermore, Method B showed a good performance at identifying objects with bright colors, such as the plastic blue-sheets, whereas Method C showed high ability at separating objects with similar visual appearance, such as soil and dead vegetation. These results help users to choose an appropriate method that suits their target, so that different wastes or multiple resources can be monitored at the same time by combining different methods, which contributes to an improved integrated resource management system.

## **Chapter 7 Conclusion and Recommendations**

The novelty of this thesis are: Developed an original index to evaluate GCP setting by both number and spatial distribution; Unraveled the reason for the deviation between DSM-derived plant height and reference value, and suggested method of moderation; Discussed the difference in restricting crop structure by different data types, and suggested the proper use for each method; Verified the linear correlation between NDVI and CC sensed by UAV under different resolutions and found out the error factor when monitoring vegetation index by UAV; and Applied the land-use classification methods on ground objects identification at farmland, and suggested the proper methods for identifying objects made from different materials. By these results, we were able to answer the questions at the introduction. Finally, the results suggested by this research could be summarized as the integrated management flow chart. RGB imagery obtained by UAV could be used to construct DSM data and point cloud data, which are useful to monitor the crop status during the early growth stage by calculating plant height or canopy volume. On the other hand, during the later growth stage, when the plant height stops to increase, the canopy cover and NDVI calculated by multispectral imagery obtained by UAV is more qualified for crop growth monitoring. Moreover, ground object identification discussed by this research could not only increase the accuracy when evaluating the crop status using canopy cover or NDVI, but also contribute to a better farmland management strategy and environment. This integrate management method for crop growth assessment and farmland management based on multiple kind of data types and analysis methods is thought to be the novelty of this research.

## Summary in Japanese

### 第一章 研究背景と目的

精密農業は、センシング情報に基づく営農計画により省力化・効率化・緻密な営農を行う技術であり、デジタルマッピング開発による農業機械の自動制御が重視されている。各圃場または圃場内の作物の成長と土壌条件に関する空間情報は、精密農業を促進するために特に重要である。そこで、精密農業において大きな役割を果たしている作物の生育状況や土壌の実態を空間的に計測する方法として、人工衛星や UAV によるリモートセンシングが利用されてきた。UAV 空撮画像を用いて農作物の生育状態を把握する研究や収穫量を予測する研究は世界中で行われてきた。また、作物高、植被率および植生指数は作物の追肥時期・施肥量を決定する上で重要な指標であり、正確な生育状況の把握は農家の収入向上に繋がられる。しかし今までの研究では、伝統リモートセンシングの解析手法を UAV 画像に適用し、モニタリングの精度を衛星画像と比較検討するものが多く、UAV 画像の特徴である高解像度による独特な課題（作物の茎葉形態、圃場内の地物等は可視化され、リモートセンシングの結果に影響を及ぼす）を検討しなかった。また、高さ、植被率、または植生指数という特定の指標による生育評価が多く、作物の生育段階に応じて最適な評価方法を提案した研究はまだない。さらに、それぞれのパラメータをモニタリングする解析手法は雑多であり、各解析手法の推定精度や特性を比較検討し、異なる調査目的に相応した解析手法を確定する研究はまだ見られていない。以上を踏まえ、本研究はまず最適な UAV 空撮の前期準備として、農業地域における最適な GCP の設置方法を提案し、さらに作物高、植被率および植生指数をモニタリングする最適な解析手法を検討することにより、UAV 空撮画像に基づいた植生評価と農地管理の統合的管理手法を確立することを目的とした。なお、本論文は 7 章から構成されており、2 章では UAV 空撮に関する作成方法の検討、3 章、4 章、5 章では作物を対象として植物体の成長評価の検討、6 章では農地管理に関する UAV 画像の適合性を検討し、7 章では植生評価と農地管理を統合させた UAV 画像による統合管理手法を提案する。

### 第二章 農地における小型 UAV 写真測量のための地上基準点の最適な設置方法

地上基準点 (Ground Control Point, GCP) は、無人航空機 (Unmanned Aerial Vehicle, UAV) リモートセンシングの空撮データの位置情報を校正するための重要なキャリブレーション方法である。近年、GCP の最適な数と分布形状に関する



研究は世界中で行われてきた。しかし、住宅・建設現場・農地や森林などにおける調査では、GCP を対象地内部に設置することは困難であり、調査地内の植生や農作物を破壊する可能性がある。したがって、農地等特殊な現場では、GCP を調査対象の周辺や外縁部のみに設置するのは一般的である。この場合、既往の研究で提案された GCP の最適な設置方法は適用できない。そこで本研究では、調査対象地の外縁部のみが利用可能な場合に、最も正確的・効率的に空撮データを校正できる GCP の設置方法を提案することを目的としている。この研究では、16ha の圃場において、GCP の数・分布形状が異なる 88 個の GCP パターンの補正精度が比較検証された。その結果、GCP が圃場四週において均等分布するパターンが最良のキャリブレーション (RMSE = 0.15m) を提供できることがわかった。障害物・圃場の条件などにより上記の分布が実現できない場合には、圃場の半分において均等分布する長形状の GCP パターン、または圃場の三辺に均等分布する三角形状の GCP パターンは適度な補正精度 (それぞれ RMSE = 0.18m, 0.43m) を達成できる。一方、GCP が直線状になるパターンは、GCP の数が多いにもかかわらず最低の補正精度 (RMSE = 2.10m) をもたらした。このことから、縦横比のバランスが比較的均等的な二次元形状 (長方形・三角形等) になっている GCP パターンは、直線状の GCP パターンより補正効果が良いことがわかった。本研究はさらに、GCP 分布指数 (GCP Distribution Index, GDI) という指標を提案し、GCP の数および分布形状をともに考慮して GCP の補正精度を推定する方法を提案した。本研究の結果は、農地等内部に進入困難な調査地における UAV 空撮調査のための GCP の最適な設置方法を提案し、UAV の農業現場でのより効率的な活用に貢献したと考えられる。

### 第三章 茎葉形態を考慮した小型 UAV による DSM データに基づく作物高の推定方法

UAV は衛星・航空写真と比較して安価なコストで、随時に高解像度の空撮画像を取得できるメリットから、農業現場での活用が期待されている。UAV 空撮画像による数値表面モデル (Digital Surface Model, DSM) を用いて作物高をモニタリングする研究は今まで世界中で様々な作物に対して行われてきた。しかし、茎葉形態が大きく異なる複数の作物に対する推定精度の違いを検討する研究はまだない。UAV は高解像度の空撮画像を提供する一方、撮影対象物の細部の構造上の差異 (農作物の場合は作物の茎葉形態) は UAV 写真測量の結果を大きく影響するという特徴も無視できない。そこで本研究は、単子葉植物であるエンバクとリードカナリ

ーグラスと、双子葉植物であるバレイショとエゴマを対象に、UAVによるDSMデータを用いて全生育期間の作物高モニタリングを行い、推定精度を比較することで、作物の茎葉形態が推定精度に与える影響を検討した。その結果、葉身が卵形で茎葉が繁茂しているエゴマに対して最高な推定精度 ( $R^2 = 0.97$ ,  $RMSE = 5\text{cm}$ ) が得られ、茎葉が繁茂するほどDSMによる推定作物高の精度が高いことがわかった。全期間における推定作物高と実測値の回帰方程式を比較した結果、単子葉植物に対して推定値は常に実測値と一定の差を保つ一方、双子葉植物に対しては生育初期において推定値は実測値より低く、作物の成長につれ実測値に近付き、最終的に（作物高が1m以上）実測値と上回ることがわかった。これらの結果から、DSMデータを用いて作物高を推定する際には該当作物に適切は回帰方程式でDSM値を補正する必要があることがわかった。さらに、本研究は四種類の常用作物の全生育期間における作物高の推定式を提供することにより、今後のDSMによる作物生育モニタリングのための基礎資料を蓄積した。

#### 第四章 UAV空撮画像によるDSMデータと三次元点群データを用いた

##### 作物高と地上部体積の推定

作物高と作物の地上部体積は、UAV空撮が作物の生育度合いを反映する重要な指標である。従来のリモートセンシングではDSMデータを用いて作物の地上部形態を反映するのが一般的であるが、UAVによる高解像度の空撮画像に基づいた作物の細部の特徴を忠実に再現する三次元点群データの作物生育モニタリングへの有効利用が期待されている。一方、DSMデータは比較的軽量であり、一般的な地理情報システムソフトウェアで解析・共有できるメリットに対し、三次元点群データはデータ量が膨大し、可視化されるためには専用ソフトウェアが必要である等のデメリットがある。UAVの農業での効率活用のために、DSMデータと三次元点群データの農作物の作物高と地上部体積を推定する際の差異を比較検討し、調査目的に最適なデータ種類を明らかにする必要がある。そこで本研究は帯広畜産大学の実験圃場において、DSMデータと三次元点群データのリードカナリーグラスの作物高の推定精度と、作物の地上部体積の推定結果を比較した。その結果、三次元点群データは作物高の推定において点群データより高い精度（それぞれ $RMSE = 4\text{ cm}$ ,  $3\text{ cm}$ , 推定式の切片  $\text{Intercept} = 8.8, -0.16$ ）が得られ、三次元点群データを用いて作物高を推定する際には回帰方程式の補正が不要であることがわかった。したがって、作物の正確な高さや倒伏情報が必要な場合は三次元点群データが適切であることがわかった。一方、DSMデータと三次元点群データによる地上部体積の推定値は、全生育期間において有意差が確認されなかった。このことより、地上部体積の推定は二種類のデータが同じパフォーマンスを持っており、

実用性を考慮すると DSM データが適切であることがわかった。本研究は異なる目的に応じた UAV 空撮データの種類を提案することにより、UAV 空撮の農業への実利用に貢献したと考えられる。

## 第五章 異なる地上解像度における小型 UAV による NDVI と植生被覆率の関係

植生被覆率は、作物の発育を表す重要な指標であり、AquaCrop 等の作物成長シミュレーションモデルにおいて作物の蒸散量を計算する基準でもある。過去において Landsat や Sentinel2 などの衛星画像による正規化植生指数 (Normalized Difference Vegetation Index, NDVI) を用いた植生被覆率のモニタリング一般的であり、衛星画像による NDVI と植生被覆率の間に強い相関関係が存在することがわかっている。近年において、小型 UAV の普及が迅速に発展しており、また多種の光学センサーが搭載可能のメリットにより、農作物の NDVI および植生被覆率のモニタリングへ利用されている。しかし、UAV 空撮画像による NDVI と植生被覆率の関係を検証した研究はまだなく、UAV 空撮画像の高解像度をもたらした新たな課題 (細かい地物が観測可能となる) が NDVI と植生被覆率の関係への影響はまだ不明である。そこで本研究は、帯広畜産大学の実験圃場内のラッカセイ畑を対象に、小型 UAV による NDVI と植生被覆率を、0.5m から 10m の五種類の地上解像度において比較し、異なる地上解像度における NDVI と植生被覆率の関係を検討した。その結果、NDVI は 0.5m, 1.0m, 2.5m, 5.0m, および 10m の地上解像度において植生被覆率と強い相関関係 (それぞれ  $R^2 = 0.88^{**}, 0.92^{**}, 0.94^{**}, 0.89^{**}, 0.93^{**}$ ) を持つことがわかった。また、ANACOVA の結果により、NDVI と植生被覆率の回帰方程式は各種地上解像度において有意差がないこともわかった。以上より、空撮画像の地上解像度は NDVI と植生被覆率の関係に顕著な影響を与えず、NDVI による植生被覆率の推算には衛星画像と UAV 空撮画像の併用性があることが示唆された。一方、各回帰方程式において、回帰係数は 1.0 に近いにもかかわらず、切片は 0.25 であったことから、植生被覆率の値が 0 のときに NDVI の値がマイナスであることが示された。その原因は、圃場内に施用されているプラスチック製のマルチシートが低い NDVI 値を持っていたからと考えられる。このことから、同じピクセル内に混在する作物と土壌以外の地物は NDVI と CC との正確な関係を求める際に悪影響になることがわかった。今後の研究では、UAV 空撮画像の高解像度の特性と十分に利用し、作物の生育評価指標を正確に計測するために農地内の地物判別が重要な課題となっている。

## 第六章 UAV 空撮画像に基づく三種類の地物自動判別方法の比較検証

植生・資源や廃棄物等多様な地上物の自動判別は、農地や農村地域の環境および統合資源管理の上重要である。また、空撮画像により作物の生育を評価する際、植生と土壌以外の地物はノイズとなるため、農地内の地物判別は UAV リモートセンシングを農業に実利用する際に重要な課題である。今までの UAV 空撮画像分類手法は、主には土地利用・土地被覆マップの作成のために用いられており、UAV 空撮画像と衛星画像による土地利用マップの精度を比較する研究は一般的であった。衛星や大型航空機による空撮画像のメリットは広域なデータを取得できることである一方、UAV 空撮画像のメリットは低空飛行による局所の高解像度データの取得である。そのため、画像分類手法の UAV リモートセンシングへの利用は、地域規模の土地利用マップの作成ではなく、単一農地等の局部調査地の地物分類に注目するべきと考えられる。そのため本研究は帯広畜産大学の実験圃場において小型 UAV により空撮を行い、RGB 画像およびマルチスペクトル画像を取得し、三種類の自動分類方法（A.NDVI 閾値法；B.RGB 画像機械学習法；C.オブジェクトベース画像解析（OBIA）法）により地物判別を行い、それぞれの方法が適す対象地物を検討した。その結果、NDVI 閾値法は処理過程が簡単であり効率性が良く、植生と土壌を高精度で識別できたが、衰弱植生やプラスチック製品と金属製品の識別では精度が低かった。RGB 法と OBIA 法は両方とも教師あり機械学習を適応しており、画像処理にあたり時間と労力が必要だったが、植生、土壌、プラスチックおよび金属の分類に非常に高い精度が得られた。具体的に、RGB 法は全体精度が最も高く、特にプラスチック製のブルーシート等明るい色の地物の識別に優れているが、衰弱植生をそれと類似した色の土壌として分類する傾向を示した。一方、OBIA 法は近赤外域のデータを使用したため、土壌と衰弱植生等視覚的に類似した地物の識別に高いパフォーマンスを示したが、総合的な分類精度は RGB 法よりわずかに低かった。これらの結果は、UAV 地物判別の対象物に合った適切な方法を選択するのに役立ち、農地や農村地域の統合資源管理の改善に貢献できると考えられる。

## 第七章 総括

本論は農地における UAV 空撮画像の最適な位置補正方法、作物高と地上部体積の推定方法の検討と比較、植生指数と作物被覆率の関係、そして農地内の地物判別という四つの視点から、UAV 空撮画像の農地への利用方法を統合的に検討した。その結果、農地における UAV 空撮には圃場を囲む 6 個以上の GCP は十分であり、6 個以下を使用場合には GDI により補正精度を予測し、GDI が 3 以上の場合には農地調査に適す補正精度が得られることがわかった。作物高を推定するため、DSM を使用する場合には作物の茎葉形態が推定精度に影響を与え、対象作物に適した

回帰モデルを使用することがわかった。一方、点群データは作物の細部の特徴を忠実に復元し、倒伏判別等のために特定位置の詳細な作物高を抽出するに適している。作物の地上部体積を推定する際に、DSM と点群データは同様な推定結果を提供するため、通用性が高く処理が比較的簡単な DSM が適すことがわかった。また、空撮画像の地上解像度は NDVI と CC の関係に有意な影響を与えないため、NDVI と CC の換算に異なるプラットフォームによる空撮画像を使用することが可能であることがわかった。さらに、農地内の植生と土壌以外の地物は NDVI による作物生育評価に悪影響を与え、農地内の地物判別が重要であるため、本研究は RGB 画像またはマルチスペクトル画像による地物分類方法を比較検討し、異なる地物の判別に最適な分類方法を提案した。以上のことから、UAV 空撮画像の利点である高解像度の画像と点群データを活用することで、作物の成育ステージに応じた成育評価を行うことが可能であることが明らかになった。また、圃場の管理をする上で、対象物に応じた画像の選択を行うことが重要であることが示された。

この論文の新規性は：GCP 設定を数と空間分布の両方で評価するための独自の指標を開発したこと；DSM から得られた草丈と基準値との偏差の理由を解明し、緩和方法を提案したこと；さまざまなデータ型によるクロープ構造の制限の違いについて説明し、各方法の適切な使用法を提案したこと；さまざまな解像度で UAV によって検出された NDVI と CC の間の線形相関を検証し、UAV によって植生指数を監視する際のエラー要因を解明したこと；土地利用分類法を農地での地上物体の識別に適用し、異なる材料で作られた物体を識別するための適切な方法を提案したことである。これらの結果により、導入時の質問に答えることができた。この研究によって示唆された結果は、統合管理のフローチャートとして要約することができる。UAV によって取得された RGB 画像を使用して DSM データとポイントクラウドデータを構築でき、これらのデータは、植物の高さまたはキャノピー ボリュームを計算することにより、初期の成長段階で作物の状態を監視するのに役立つ。一方、成長の後期段階では、草丈の増加が止まると、UAV によって取得されたマルチスペクトル画像によって計算されたキャノピー カバーと NDVI は、作物の成長の監視に適している。さらに、この研究で議論された地表オブジェクトの識別は、キャノピーカバーまたは NDVI を使用して作物の状態を評価する際の精度を高めるだけでなく、より良い農地管理戦略と環境にも貢献する可能性がある。

## **Acknowledgement**

In the beginning, I would like to acknowledge my supervisor, Prof. Dr. Hiromu Okazawa for guiding me, inspiring me, and supporting me throughout my doctoral course. It was his intelligence, diligence, gentleness, tolerance and dedication that helped me completed this research work. No matter how busy he was, or how crazy his schedule was, he always made time for me and my research. When I wanted to try new study topics, he was always there to encourage me and used every kind of resource to let them happen. When I faced difficulties, he did everything he could to help me. When I made mistakes, he let me know what the right thing is to do patiently and reasonably. When I was broken the most and lost my purpose, he did not abandon me but tried his best to get me on my feet again. Like so many international students, we have no family in this country, but my professor has made me feel that I have a home here. I could never have finished my doctoral research without his kind heart and thoughtful help. For that I can never ever thank him enough.

Apart from my supervisor, I would like to thank my committee members, Prof. Dr. Sawahiko Shimada, Associate Prof. Dr. Ayako Sekiyama and Prof. Dr. Kiichiro Hayashi for giving me the encouragement and sharing insightful suggestions.

I need to thank the Doctoral Research Grant Program of Tokyo University of Agriculture and “Establishment of a Sustainable Community Development Model based on Integrated Natural Resource Management System in Lake Malawi National Park (IntNRMS) Project” under the Science and Technology Research Partnership for Sustainable Development (SATREPS) program supported by the Japan Science and Technology Agency (JST) and Japan International Cooperation Agency (JICA), for funding this research.

I am really grateful to Dr. Sarvesh Maskey, Dr. Lameck Fiwa, Dr. Tamano Hayashi, Prof. Dr. Tetsu Sato and Dr. Eri Maai, who have been selflessly helping me even though they did not have to. They have not only showed me what it looked like to be a researcher, but also the light of humanity. Maskey sensei, Lameck, Tamano sensei, I will always miss the good time we had together. We will always be good fellows even separated. Maai sensei, it means a lot to me that I’ve got to meet you. Maybe it doesn’t make much sense to you but, I just want to say thank you so much for being here.

I am so thankful to my dear fellow lab mates, especially Perez Fuentes Antonio and Dickson Mgangathweni Mazibuko from the doctoral course, Kiseki Kurashina, Kazuha Wakasugi, Masamune Takahashi, Huan Uego and Xiaoming Zhang from the master course, and Hiyori Iseki, Keita Hidai and Masayoshi Yoshizawa from the undergraduate school. Tonio, you were there for me as a reliable friend during the darkest time of my life. I can't imagine how I could survive those days without your help. For that I will always be grateful. Kiseki and Hiyori, you were one of the most hard working students I have met. You were also the gentlest students I have ever seen. Thank you for always being here in the lab, cheering me up when I was upset, listening to me when I was troubled, and thank you for the huge amount of snacks that kept me from starvation at night. There is so much else that I should say thank you for. I wish you two the brightest future. Kazuha, you are such a cheerful lad and you made me felt like I had a little brother which I never really have. It shocked me too when we were counting how many days we had left to see each other, but I guess this is life. I won't be that far away though; I will see you around. Masa, you are the one that I talked to the most. We know the anguish of each other, and we have been trying to help each other solve them. But you will be on your own from now on. Don't keep the worries to yourself, share them with sensei and your fellows, trust me, they will all be willing to listen. Remember sensei's words, the secret of getting things down is to act. I have faith in you. Same for all my senior and junior mates, every one of you helped me a lot, taught me a lot and gave me a lot in your own special way. I have so much to say to you guys, but I guess just like the song, "I will tell you all about it when I see you again". I will never forget you guys.

Finally, I would like to thank my parents, for bringing me to this world, and supporting me all the way through. I am so, so sorry that I couldn't become what you had expected me to be, that I have to be far away from your side. I wish you all the best back home. Your healthy and happy lives is what I wish the most in this world.

There is an old saying in my mother tongue – Do not say thank you to the greatest favor. It has been a long ride, the doctoral course, long enough to change my entire personality and the creed of my whole life. It's never easy to change, but in the end, I am glad that I have got the chance to give my best try. There has been tears, and there has been suffering, but there has also been a rebirth. I have not only learnt how to be a researcher, but also learnt how to be a person. To that I shall not say "thank you". I will use the rest of my life, to prove that your efforts were not in vain.

## Table of Contents

<b>Summary</b> .....	I
<b>Summary in Japanese</b> .....	VII
<b>Acknowledgement</b> .....	XIII
<b>Table of contents</b> .....	XV
<b>List of Figures</b> .....	XIX
<b>List of Tables</b> .....	XXII
<b>Chapter 1 Backgrounds and Objectives</b> .....	<b>1</b>
1.1 Backgrounds .....	1
1.2 Research Problems and Aims of This Study .....	3
1.3 Outline .....	5
Reference of this chapter .....	6
<b>Chapter 2 Optimization of Ground Control Point Distribution for Unmanned Aerial</b> .....	<b>12</b>
<b>Vehicle Photogrammetry in Farming Land</b> .....	<b>12</b>
2.1 Introduction .....	12
2.2 Methodology .....	14
2.2.1 Study site .....	14
2.2.2 Data collection.....	15
2.2.3 Data Processing .....	18
2.3. Results .....	21
2.3.1. Relationship between GCP Error and Check Point Error .....	21
2.3.2. Relationship between GCP Number and Check Point Error.....	24
2.3.3. Relationship between GCP Configuration Type and Check Point Error .....	25
2.3.4. Describing the Calibration Ability of GCPs by GDI .....	28
2.3.5. Relationship between the Position of Check Point Distance and Check Point Error.....	30
2.4 Discussion .....	32
4.5 Conclusions of this chapter .....	36



Reference.....	37
<b>Chapter 3 Monitoring of Crop Plant Height Based on DSM Data Obtained by Small UAV Considering the Difference of Plant Shapes.....</b>	<b>41</b>
3.1 Introduction .....	41
3.2 Methodology .....	43
3.2.1 Study site .....	43
3.2.2 UAV surveys .....	45
3.2.3 Ground surveys.....	46
3.2.4 Data analysis.....	46
3.3 Results and Discussion.....	47
3.3.1 Accuracy of estimated plant height for Perilla.....	47
3.3.2 Accuracy of estimated plant height for Potato .....	48
3.3.3 Accuracy of estimated plant height for Reed .....	50
3.3.4 Accuracy of estimated plant height for Oat.....	51
3.3.5 Accuracy of estimated plant height for Barley.....	53
3.3.6 Correction of estimated plant height by canopy cover.....	55
3.4 Conclusions of this chapter .....	56
Reference of this chapter.....	57
<b>Chapter 4 Comparison of DSM and 3d Point Cloud by Small UAV Imagery on Estimating Plant Height and Biomass Volume .....</b>	<b>58</b>
4.1 Introduction .....	58
4.2 Methodology .....	59
4.2.1 Data collection.....	59
4.2.2 Data analysis.....	60
4.3 Results .....	61
4.3.1 Time series of the plant height estimated by point clouds and DSMs .....	61
4.3.2 Comparison of the accuracies of plant height estimated by DSM and 3D point cloud data .....	61

4.3.3 Comparison of biomass volume estimated by DSM and point cloud data .....	63
4.4 Discussion .....	64
4.5 Conclusion of this chapter .....	65
Reference of this chapter .....	66
<b>Chapter 5 Relationship between NDVI and Canopy Cover Sensed by Small UAV under Different Ground Resolution.....</b>	<b>67</b>
5.1 Introduction .....	67
5.2 Methodology .....	68
5.2.1 Data collection.....	68
5.2.2 Data analysis.....	69
5.3 Results .....	71
5.3.1 Relationship between NDVI and canopy cover under different ground resolution .....	71
5.3.2 Accuracy of predicted canopy cover by NDVI.....	73
5.4 Discussion .....	74
5.5 Conclusion of this chapter.....	74
Reference of this chapter .....	75
<b>Chapter 6 Assessment of Three Automated Identification Methods for Ground Objects Based on UAV Imagery.....</b>	<b>76</b>
6.1 Introduction .....	76
6.2 Methodology .....	79
6.2.1 Study site .....	79
6.2.2 Data collection.....	81
6.2.3 Classification procedures .....	85
6.2.4 Accuracy evaluation of the classification methods .....	87
6.3 Results .....	88
6.3.1. UAV Mapping Products.....	88
6.3.2. Comparison of Classification Results .....	91
6.3.3. Accuracy Evaluation of the Classification Methods .....	93

6.4 Discussion .....	96
6.5 Conclusion of this chapter.....	98
Reference of this chapter.....	99
<b>Chapter 7 Conclusion and Recommendations.....</b>	<b>104</b>
<b>Appendix .....</b>	<b>106</b>

## List of Figures

Figure 2.1 Study site location.....	15
Figure 2.2 Distribution of GCPs and check points inside the study site.....	16
Figure 2.3 Anti-aircraft signals (Left: For GCPs; Right: For check points).....	16
Figure 2.4 RTK-GNSS (TOPCON HiperV) measuring.....	17
Figure 2.5 UAV photography with Inspire2 at the study site.....	17
Figure 2.6 Data process workflow.....	18
Figure 2.7 Typical GCP patterns of each group and each configuration type.....	20
Figure 2.8 Relationship between GCP error and check point error: (a) Horizontal error; (b) Vertical error (**: $p$ -value < 0.01; *: $0.01 \leq p$ -value < 0.05).....	24
Figure 2.9 Relationship between GCP number and mean check point error.....	25
Figure 2.10 Horizontal error of each GCP pattern in the 3-GCP Group, 4-GCP Group, and 5-GCP Group.....	26
Figure 2.11 GCP patterns with above-1.0 m-horizontal error: (a) Pattern 05, 3-GCP Group; (b) Pattern 07, 3-GCP Group; (c) Pattern 13, 4-GCP Group; (d) Pattern 14, 4-GCP Group; (e) Pattern 15, 4-GCP Group; (f) Pattern 16, 4-GCP Group; (g) Pattern 01, 5-GCP Group; (h) Pattern 03, 5-GCP Group; (i) Pattern 04, 5-GCP Group.....	27
Figure 2.12 Relationship between the factors describing GCP distribution: (a) GDI; (b) Rate of area surrounded by GCPs; (c) Number of GCPs.....	29
Figure 2.13 Relationship between the horizontal error and the distance between GCPs and the check point: (a) All patterns; (b) 3-GCP-Group; (c) 4-GCP-Group; (d) 5-GCP Group; (e) 6-GCP Group; (f) 8-GCP Group; (g) Above-10-GCP Group (**: $p$ -value < 0.01; *: $0.01 \leq p$ -value < 0.05).....	31
Figure 2.14 GCP patterns and horizontal error ( $E_{horizontal}$ ) for the 3-GCP Group.....	34
Figure 3.1 Location of Study Site.....	44
Figure 3.2 (a) Time series of plant height of Perilla.....	48
Figure 3.3 (b) Relationship between the estimated plant height by DSM and measured plan height of Perilla.....	48
Figure 3.4 (a) Time series of plant height of Potato.....	49
Figure 3.4 (b) Relationship between the estimated plant height by DSM and measured plan height of Potato.....	49
Figure 3.5 (a) Time series of plant height of Potato.....	50
Figure 3.5 (b) Relationship between the estimated plant height by DSM.....	51
and measured plan height of Potato.....	51

Figure 3.6 (a) Time series of plant height of Oat .....	52
Figure 3.6 (b) Relationship between the estimated plant height by DSM and measured plan height of Oat .....	52
Figure 3.7 (a) Time series of plant height of Barley .....	53
Figure 3.7 (b) Relationship between the estimated plant height by DSM and measured plan height of Barley .....	54
Figure 3.8 Relationship between the estimated plant height by DSM and .....	54
measured plan height of Barley during different growing period: .....	54
(a) From 2019/6/19 to 6/26; (b) From 2019/7/3 to 8/4.....	54
Figure 3.9 Relationship between measured and estimated PH .....	55
corrected by Canopy Cover .....	55
Figure 4.1 Workflow of data analysis .....	60
Figure 4.2 Time series of $PH_M$ , $PH_{PC}$ and $PH_{CSM}$ .....	61
Figure 4.3 Relationship between $PH_M$ and $PH_{CSM}$ .....	62
Figure 4.4 CSM map for grass field (2019/7/24) .....	62
Figure 4.5 Relationship between $PH_M$ and $PH_{PC}$ .....	63
Figure 4.6 Comparison of $BV_{PC}$ and $BCANOPY\ COVER_{SM}$ .....	63
Figure 5.2 Classification result.....	69
(Left: RGB orthomosaic image; Right: Classified raster).....	69
Figure 5.3 Example of squared grid dividing the peanuts field (Grid size: 1.0 m).....	70
Figure 5.4 Spatial distribution of NDVI (a) and vegetation cover (b) .....	71
Figure 5.5 Relationship between NDVI and CC.....	72
Figure 5.6 Relationship between the predicted CC value and the reference CC value.....	74
Figure 6.1. Aerial image of the experimental field with the classification verification site marked by the red dotted line. ....	80
Figure 6.2. The ground objects at the study site: (a) Vegetation; (b) Dead/weakened vegetation; (c) Soil; (d) Multi-sheet and metal ; (e) Plastic blue sheet .....	81
Figure 6.3. Unmanned aerial vehicles (UAVs) used for the aerial surveys: .....	82
(a) Phantom 4 Pro (DJI); (b) Inspire 1 (DJI) with Sequoia (Parrot).....	82
Figure 6.4. Workflow for the Structure from Motion (SfM) process.....	84
Figure 6.5. Segmentation result (eCognition Developer 9.0, Trimble).....	87
Figure 6.6. One thousand assessment points used for the accuracy assessment .....	88
of the classification results .....	88

Figure 6.7. Mapping products generated from the unmanned aerial vehicle (UAV) images: (a) Red-green-blue (RGB) orthomosaic; (b) Red band orthomosaic; (c) Near-infrared orthomosaic; (d) normalized difference vegetation index (NDVI) raster; (e) Mixed image in eCognition Developer 90

Figure 6.8. Classification results: (a) Normalized difference vegetation index (NDVI) threshold method; (b) Red-green-blue (RGB) image-based machine learning method; (c) Object-based image analysis (OBIA) method.....92

Figure 6.9. Pixel percentage of the classes for each classification method.....93

## List of Tables

Table 2.1 Coordinates of GCPs and check points .....	23
Table 2.2 Reference value of GDI, area rate, and number of GCPs of each rank of horizontal.....	30
Table 2.3 Average horizontal error of check points of these three types for each GCP group (m)...	32
Table 5.1 Flight parameters.....	68
Table 5.2 Model parameters of ANCOVA .....	73
Table 6.1. Unmanned aerial vehicle (UAV) and camera specifics .....	82
Table 6.2. Normalized difference vegetation index (NDVI) threshold values for the different classes .....	86
Table 6.3(a). Confusion matrix for the normalized difference vegetation index (NDVI) threshold method .....	95
Table 6.3(b). Confusion matrix for the red-green-blue (RGB) mage-based machine learning method .....	95
Table 6.3(c). Confusion matrix for the object-based image analysis (OBIA) method .....	95

## Chapter 1 Backgrounds and Objectives

### 1.1 Backgrounds

According to the results of the agricultural labor force survey conducted by the Ministry of Agriculture, Forestry and Fisheries in 2019 [1], the agricultural working population was 1.681 million, a decrease of about 60% for 20 years ago (3.891 million). Abandoned farmland is increasing due to the drastic decrease in the number of farmers engaged in agriculture, and large-scale agriculture is progressing in Japan, such as consolidating small-scale farmlands and expanding the management area per household. In addition, the percentage of people aged 65 and over among the population working in agriculture has reached 70.2%, a marked increase from 20 years ago (20.8%), further aggravating the problem of labor shortage. Against this background, precision agriculture has been developed as a technology for more labor-saving, efficient, and precise farm management that makes full use of precise farm management plans based on sensing information, and automatic control of agricultural machinery based on digital mapping development are emphasized [2].

Compared to precision agriculture, traditional farming techniques emphasize the know-how and skills of farmers [3]. For example, the technology of diagnosing crops and soil by visual judgment, the technology of decision-making based on long-term farm management and exchanges between farmers, and the technology of work are emphasized. However, such a farming method requires long-term construction research and subjective judgment of farmers, and the hurdles are becoming higher in the current situation where the number of farmers is decreasing, and aging is progressing. On the other hand, in precision agriculture, emphasis is placed on the development and dissemination of data-based, objective, and easy-to-communicate technology [4]. For example, remote sensing technology, information communication technology, application of artificial intelligence, and the development and use of agricultural robot technology [5]. In this way, precision agriculture can improve yield and quality by optimizing production management and can save labor and materials [6].

Spatial information about crop growth and soil conditions for each field or within a field is particularly important for promoting precision agriculture [5]. As basic information for planning and making decisions on farming; or as a digital map for agricultural machinery control. In addition, it becomes an important information source as agricultural field spatial information that plays a part of big data that drives artificial intelligence [7]. Therefore, remote sensing by satellites and UAVs has been used as a method for spatially measuring crop growth and actual conditions of soil which plays a large role in precision agriculture [8].

Since World War II, satellites have been launched based on advances in the three technologies of sensors, platforms, and computers, and have become essential technologies for modern remote sensing [9]. However, satellite data cannot be obtained due to cloud cover,



and there is a possibility that we will miss the right time to observe the growth of crops. Landsat satellites, Terra satellites, and SPOT satellites used in agriculture have a ground resolution of several tens of meters [10]. Therefore, the development of new remote sensing platforms suitable for crop monitoring is an important issue in promoting smart agriculture today [11]. Since the 2010s, UAVs (Unmanned Aerial Vehicles) include Parrot (France, launched AR Drone in 2010), DJI (China, launched Phantom series in 2012), 3D Robotics (USA, launched Iris in 2013) have made dramatic progress in performance and spread around the world, and have come to be used in various applications such as disaster relief, civil engineering surveying, pesticide spraying, and infrastructure inspection [12]. Compared with satellite data, UAVs have advantages such as high maneuverability, high resolution, and low altitude flight (not affected by clouds) [13]. At present, with the development of GPS (Global Positioning System), GIS (Geographic Information System), optical sensors, information and communication technology, and the development of legal systems, UAVs are seen as a stable platform for smart agriculture [14].

As for spatial resolution, in the case of UAV, it is possible to achieve ultra-high resolution of several millimeters to several centimeters by appropriately selecting flight altitude and sensor specifications [15]. Therefore, it is also used to detect weeds in the early stages of emergence, insect pests adhering to leaves, and minute pieces such as disease symptoms [16] [17] [18]. On the other hand, unlike satellites, it is difficult to cover a wide area with a single shot [19], and in this respect, there is a conflict with spatial resolution, so there is a need for exploring in more detail about the optimal observation targets and research objectives for satellites and UAVs.

High-resolution satellite sensors are promising for the production of high-quality images on a regional scale, taking advantage of wide-area observation capabilities. On the other hand, UAV remote sensing can observe a relatively small area from a low altitude, so it is promising for smart management of many fields in farming on a scale of about less than 100 ha [19]. Compared to satellite remote sensing, one of the advantages is that it is possible to select the on-board sensor and resolution relatively flexibly [20]. Referring to the current state of the world of UAV remote sensing applications in the vegetation environment field, the majority of case studies are at the level of digital camera-equipped observation or vegetation index map creation. Therefore, at present, low-cost and simplicity are often emphasized rather than advancedness, and the reports are limited to small-scale and general reports. In fact, the lack of advancedness and novelty compared with the satellite remote sensing has become one of the main limitations for widespread use of UAV practicality in agriculture field.

Based on this background, the fully utility of the advantages of UAV remote sensing by studying the unique feature of the UAV remote sensing products has become a crucial task for applying UAV to precision agriculture. This study constructed a measurement system using various sensors on UAV, and while auditing the above restrictions, applied data collection methods and image analysis methods for actual large-scale farms, and created

diagnostic maps, an integrated evaluation method has been suggested. In this chapter, the applicability of international UAV remote sensing to precision agriculture will be discussed.

## 1.2 Research Problems and Aims of This Study

In the last decades, there has been many developments in precision agriculture for increasing the crop productivity in major fields such as geolocating, variable monitoring, strategy making and practicing [21]. However, the global agriculture production system is still facing many challenges, caused by the increasing global population [22], the climate change [23], the calorie-intensive diets, food, and biomass production for biofuel [24]. Agriculture production is affected by crop variability, soil variability, field management variability and climate variability [25]. These variabilities result in differences in crop growth that can be quantified by monitoring the physical structure or optical features of the above ground part of the crop [26]. For example, normalized difference vegetation index (NDVI) [27], leaf area index (LAI) [28], canopy cover (CC) [29], plant height (PH) [30], above ground biomass (AGB) [31], and the nitrogen status [32]. Proper timing and quantity of fertilizer and topdressing are crucial factors for the final yield of crop yield [33]. On the other hand, over topdressing can cause lodging or leggings which have significant reducing effect of crops such as the grain and horticultural crops [34], and also have impact on water quality of the agriculture area [35]. Accurate information of the crop status is important for proper application of fertilizer and pesticide.

Data for monitoring crop growth are most valuable when captured with high spatial and temporal data resolution to adequately detect variability within agricultural fields. Advantages to use Unmanned aerial vehicles (UAVs) for monitoring crop growth are UAVs filling a niche in observation scale, resolution and height between manned aerial platform and ground [36]. High resolution data can be collected due to the short distance from the detection target, Minimizes atmospheric effects in the image. The mayor's advantage over satellite imagery is fast data acquisition with cloud pendency and revisit times and real-time capabilities [37]. In addition, high flexibility provides high temporal resolution of data acquisition [38]. These characteristics make the UAV very suitable for many agricultural applications [39][40]. An example is spraying from unmanned helicopters, which is most prevalent in Japan. More than 10% of his paddy fields have been sprayed using this technique [41].

Several authors have shown how to combine UAVs with lightweight sensors for crop monitoring. Crop health is the most popular topic in this regard [42]. For example, proposed by HUANG et al. (2010) for cotton fields, NEBIKER et al. (2008) for vineyards, and CALDERÓN et al. (2014) for Poppies [43][44][45]. Further research investigated water stress Irrigation by using thermal and multispectral sensors [46][47][48]. Existing research

on drone-based crop growth monitoring includes assessment of biomass and nitrogen status [49], and derivation of a vegetation index to correlate it with LAI or nitrogen uptake [50][51][52]. However, with the high spatial resolution of UAV imagery, the ground objects other than vegetation and soil with various spatial features and reflectance characteristics give significant influence on the observation result when monitoring LAI, NDVI and other vegetation indices. In the other hand, in the case of traditional remote sensing such as satellite imagery, these influences could be ignored since the observation scale is large. The high spatial resolution contributes to a more precise observation but need more study and analysis procedures to be fully used as an advancement. In addition, plant height is an important parameter for crop growth monitoring. With the extremely high spatial resolution of UAV imagery, the difference of plant shapes between different crops gives significant influence of the observation result when monitoring plant height using UAV. Few studies have examined crops with different stomatal morphologies at the same time, in the same region, and under the same flight conditions. In particular, there have been no studies comparing monocotyledonous and dicotyledonous plants, which differ greatly in stomatal morphology and cultivation methods, under the same conditions.

The precise and accurate geolocation information is another important factor for both the remote sensing and the strategy practicing for precision agriculture. Direct georeferenced using Ground Control Point (GCP) is currently the most common method to calibrate the position information of UAV imagery. Before the UAV photography is conducted, anti-aircraft signs are placed on the GCPs, so that the points can be identified from the UAV photographs. The position information of the photographs is corrected afterwards during the bundle adjustment within the Structure-from-Motion (SfM) software by inputting the correct coordinates of the GCP [52]. Many previous studies of the influence on the GCP setting to the horizontal or vertical accuracy of the SfM products. Evaluating the quality of GCP setting is a complex task because many variables have to be taken into consideration. Over the years, various studies have analyzed the effect of the number and spatial configurations of the GCPs used for indirect georeferencing [53][54][55][56]. However, for agricultural surveys, setting GCPs inside the crops is destructive for the growing plants and will cause disruptions to field management. It is necessary to acknowledge that in many surveying sites, only the outer edges of the subject area are available for GCP placement. Based on this reality, the current study aims to create a standard to evaluate the quality of GCP setting to provide a guideline for researchers or surveyors of UAV photogrammetry to decide the most optimal number and spatial configuration of GCPs without intruding into the subject area.

To actually practice UAV remote sensing to agriculture, the problems in real sites of farmland need to be further discussed. Therefore, in conclusion, the key research questions for this thesis are:

1. What is the optimal way to set GCPs during UAV survey at a farmland with growing crop?

2. What caused the estimation error when monitoring plant height of crops using UAV-based DSMs, and what is the solution?
3. What is the difference between the DSM data and the point cloud data when monitoring plant height and canopy volume of crops?
4. What is the relationship between NDVI and canopy cover sensed by UAV, and what caused the difference between the theoretical result and the observation result?
5. What procedure contributes to more accurately observe NDVI or canopy cover of crop using UAV?

### **1.3 Outline**

At this thesis, Chapter 2 examines the preparation method for UAV aerial photography. Chapter 3 to Chapter 5 examined the growth evaluation of crops, Chapter 6 examines the suitability of UAV images for farmland management, and, and Chapter 7 proposes an integrated management method using UAV images that integrates vegetation evaluation and farmland management. This paper presents four perspectives: optimum position correction method for UAV aerial images in farmland, study and comparison of methods for estimating crop height and ground volume, relationship between vegetation index and coverage rate, and discrimination of features in farmland.

The utilization of UAV aerial images for farmland was investigated in an integrated manner. As a result, it was found that 6 or more GCPs surrounding the field are the most sufficient, but when less GCPs are used, suitable accuracy could be obtained if GDI is above 3 for UAV aerial photography in farmland.

When using DSM to estimate crop height, it was found that the foliage morphology of the crop affected the estimation accuracy, and regression models suitable for the target crops were necessary. On the other hand, point cloud data is suitable for extracting detailed crop heights at specific positions for determining the lodging of crops, as it faithfully reproduces the details of the crops. It was found that DSM, which has high versatility and is relatively easy to process, is suitable for estimating above-ground volume of crops.

Also, since the ground resolution of aerial imagery does not significantly affect the relationship between NDVI and CC, it is possible to use aerial imagery from different platforms for conversion between NDVI and CC. In addition, features other than vegetation and soil in farmland adversely affect crop growth evaluation by NDVI, and feature discrimination in farmland is important.

In this study, a comparative study of different vegetation indices was carried out, and the optimal classification method for distinguishing different features was proposed. From the above, it became clear that it is possible to perform growth evaluation according to the growth stage of crops by utilizing the high resolution and point cloud data, which are the advantages of UAV aerial images. By performing integrated crop evaluation and field management using UAV that integrates these results, we were able to establish a more precise evaluation method using UAV aerial images.

### Reference of this chapter

1. Ministry of Agriculture, Forestry and Fisheries, Japan. Current Situation and Future Projections for Rural Areas and Villages, Section 1: Current Situation of Rural Areas and Movement of Rural Development, FY2019 Summary of the Annual Report on Food-Agriculture and Rural Areas in Japan. Available online: [https://www.maff.go.jp/j/wpaper/w\\_maff/r1/r1h/trend/part1/pdf/c3\\_1\\_00.pdf](https://www.maff.go.jp/j/wpaper/w_maff/r1/r1h/trend/part1/pdf/c3_1_00.pdf)
2. Inoue, Y. & Yokoyama M., (2017). Drone-based Remote Sensing of Crops and Soils and its Application to Smart Agriculture. *Journal of The Remote Sensing Society of Japan* Vol. 37 No. 3 (2017) pp.224-235
3. Abdullahi, H. S., Mahieddine, F., & Sheriff, R. E. (2015, July). Technology impact on agricultural productivity: A review of precision agriculture using unmanned aerial vehicles. In *International conference on wireless and satellite systems* (pp. 388-400). Springer, Cham.
4. Liaghat, S., & Balasundram, S. K. (2010). A review: The role of remote sensing in precision agriculture. *American journal of agricultural and biological sciences*, 5(1), 50-55.
5. Zhang, C., & Kovacs, J. M. (2012). The application of small unmanned aerial systems for precision agriculture: a review. *Precision agriculture*, 13(6), 693-712.
6. Swinton, S. M., & Lowenberg-Deboer, J. (2001, June). Global adoption of precision agriculture technologies: Who, when and why. In *Proceedings of the 3rd European Conference on Precision Agriculture* (Vol. 2, pp. 557-562). Citeseer.
7. Ampatzidis, Y., Partel, V., & Costa, L. (2020). Agroviz: Cloud-based application to process, analyze and visualize UAV-collected data for precision agriculture applications utilizing artificial intelligence. *Computers and Electronics in Agriculture*, 174, 105457.

8. Radoglou-Grammatikis, P., Sarigiannidis, P., Lagkas, T., & Moscholios, I. (2020). A compilation of UAV applications for precision agriculture. *Computer Networks*, *172*, 107148.
9. Mulla, D. J. (2013). Twenty five years of remote sensing in precision agriculture: Key advances and remaining knowledge gaps. *Biosystems engineering*, *114*(4), 358-371.
10. Khaliq, A., Comba, L., Biglia, A., Ricauda Aimonino, D., Chiaberge, M., & Gay, P. (2019). Comparison of satellite and UAV-based multispectral imagery for vineyard variability assessment. *Remote Sensing*, *11*(4), 436.
11. Maes, W. H., & Steppe, K. (2019). Perspectives for remote sensing with unmanned aerial vehicles in precision agriculture. *Trends in plant science*, *24*(2), 152-164.
12. Kapustina, L., Izakova, N., Makovkina, E., & Khmelkov, M. (2021). The global drone market: Main development trends. In *SHS Web of Conferences* (Vol. 129, p. 11004). EDP Sciences.
13. Emilien, A. V., Thomas, C., & Thomas, H. (2021). UAV & satellite synergies for optical remote sensing applications: A literature review. *Science of remote sensing*, *3*, 100019.
14. Hunt Jr, E. R., Hively, W. D., Fujikawa, S. J., Linden, D. S., Daughtry, C. S., & McCarty, G. W. (2010). Acquisition of NIR-green-blue digital photographs from unmanned aircraft for crop monitoring. *Remote Sensing*, *2*(1), 290-305.
15. Turner, D., Lucieer, A., & Wallace, L. (2013). Direct georeferencing of ultrahigh-resolution UAV imagery. *IEEE Transactions on Geoscience and Remote Sensing*, *52*(5), 2738-2745.
16. Kaivosoja, J., Hautsalo, J., Heikkinen, J., Hiltunen, L., Ruuttunen, P., Näsi, R., ... & Salonen, J. (2021). Reference measurements in developing UAV Systems for detecting pests, weeds, and diseases. *Remote Sensing*, *13*(7), 1238.
17. Roosjen, P. P., Kellenberger, B., Kooistra, L., Green, D. R., & Fahrentrapp, J. (2020). Deep learning for automated detection of *Drosophila suzukii*: potential for UAV - based monitoring. *Pest Management Science*, *76*(9), 2994-3002.
18. Albetis, J., Duthoit, S., Guttler, F., Jacquin, A., Goulard, M., Poilvé, H., ... & Dedieu, G. (2017). Detection of Flavescence dorée grapevine disease using unmanned aerial vehicle (UAV) multispectral imagery. *Remote Sensing*, *9*(4), 308.
19. Matese, A., Toscano, P., Di Gennaro, S. F., Genesio, L., Vaccari, F. P., Primicerio, J., ... & Gioli, B. (2015). Intercomparison of UAV, aircraft and satellite remote sensing platforms for precision viticulture. *Remote Sensing*, *7*(3), 2971-2990.

20. Emilien, A. V., Thomas, C., & Thomas, H. (2021). UAV & satellite synergies for optical remote sensing applications: A literature review. *Science of remote sensing*, 3, 100019.
21. Mogili, UM Rao, and B. B. V. L. Deepak. "Review on application of drone systems in precision agriculture." *Procedia computer science* 133 (2018): 502-509.
22. Ehrlich, Paul R., and John P. Holdren. "Impact of Population Growth: Complacency concerning this component of man's predicament is unjustified and counterproductive." *Science* 171.3977 (1971): 1212-1217.
23. McMichael, Anthony J., et al. "Food, livestock production, energy, climate change, and health." *The lancet* 370.9594 (2007): 1253-1263.
24. Ravindranath, N. H., Lakshmi, C. S., Manuvie, R., & Balachandra, P. (2011). Biofuel production and implications for land use, food production and environment in India. *Energy policy*, 39(10), 5737-5745.
25. Steduto, P., Hsiao, T. C., Raes, D., & Fereres, E. (2009). AquaCrop—The FAO crop model to simulate yield response to water: I. Concepts and underlying principles. *Agronomy Journal*, 101(3), 426-437.
26. Bendig, J., Yu, K., Aasen, H., Bolten, A., Bennertz, S., Broscheit, J., ... & Bareth, G. (2015). Combining UAV-based plant height from crop surface models, visible, and near infrared vegetation indices for biomass monitoring in barley. *International Journal of Applied Earth Observation and Geoinformation*, 39, 79-87.
27. Hassan, M. A., Yang, M., Rasheed, A., Yang, G., Reynolds, M., Xia, X., ... & He, Z. (2019). A rapid monitoring of NDVI across the wheat growth cycle for grain yield prediction using a multi-spectral UAV platform. *Plant science*, 282, 95-103.
28. Peng, X., Han, W., Ao, J., & Wang, Y. (2021). Assimilation of LAI derived from UAV multispectral data into the SAFY model to estimate maize yield. *Remote Sensing*, 13(6), 1094.
29. Yu, D., Zha, Y., Shi, L., Jin, X., Hu, S., Yang, Q., ... & Zeng, W. (2020). Improvement of sugarcane yield estimation by assimilating UAV-derived plant height observations. *European Journal of Agronomy*, 121, 126159.
30. Ballesteros, R., Ortega, J. F., Hernandez, D., & Moreno, M. A. (2018). Onion biomass monitoring using UAV-based RGB imaging. *Precision agriculture*, 19(5), 840-857.
31. Michez, A., Bauwens, S., Brostaux, Y., Hiel, M. P., Garré, S., Lejeune, P., & Dumont, B. (2018). How far can consumer-grade UAV RGB imagery describe crop production? A 3D and multitemporal modeling approach applied to zea mays. *Remote Sensing*, 10(11), 1798.

32. Hunt, E. R., Horneck, D. A., Spinelli, C. B., Turner, R. W., Bruce, A. E., Gadler, D. J., ... & Hamm, P. B. (2018). Monitoring nitrogen status of potatoes using small unmanned aerial vehicles. *Precision agriculture*, 19(2), 314-333.
33. Chen, Y., Peng, J., Wang, J., Fu, P., Hou, Y., Zhang, C., ... & Huang, J. (2015). Crop management based on multi-split topdressing enhances grain yield and nitrogen use efficiency in irrigated rice in China. *Field Crops Research*, 184, 50-57.
34. Zhang, W., Wu, L., Wu, X., Ding, Y., Li, G., Li, J., ... & Wang, S. (2016). Lodging resistance of japonica rice (*Oryza Sativa* L.): morphological and anatomical traits due to top-dressing nitrogen application rates. *Rice*, 9(1), 1-11.
35. Côté, D., Michaud, A., Tran, T. S., & Bernard, C. (1999). Slurry sidedressing and topdressing can improve soil and water quality in the Lake Champlain Basin. *Water Science and Application*, 1, 225-238.
36. Dash, J. P., Watt, M. S., Paul, T. S., Morgenroth, J., & Pearse, G. D. (2019). Early detection of invasive exotic trees using UAV and manned aircraft multispectral and LiDAR data. *Remote Sensing*, 11(15), 1812.
37. Ahmad, A., Tahar, K. N., Udin, W. S., Hashim, K. A., Darwin, N., Hafis, M., ... & Azmi, S. M. (2013, November). Digital aerial imagery of unmanned aerial vehicle for various applications. In 2013 IEEE International Conference on Control System, Computing and Engineering (pp. 535-540). IEEE.
38. Zhang, C., Zhang, W., Wang, W., Yang, L., & Zhang, W. (2019). Research challenges and opportunities of UAV millimeter-wave communications. *IEEE Wireless Communications*, 26(1), 58-62.
39. Yang, G., Liu, J., Zhao, C., Li, Z., Huang, Y., Yu, H., ... & Yang, H. (2017). Unmanned aerial vehicle remote sensing for field-based crop phenotyping: current status and perspectives. *Frontiers in plant science*, 8, 1111.
40. Wang, Xu, et al. "Development of visualization system for agricultural UAV crop growth information collection." *IFAC-PapersOnLine* 51.17 (2018): 631-636.
41. SI Team. "Realization OF society 5.0 BY utilizing precision agriculture into smart agriculture IN nara, Japan." *International Workshop on ICTs for Precision Agriculture*. 2019.
42. Devi, G., Sowmiya, N., Yasoda, K., Muthulakshmi, K., & Balasubramanian, K. (2020). Review on application of drones for crop health monitoring and spraying pesticides and fertilizer. *J. Crit. Rev.*, 7(6), 667-672.



43. Huang, Y., Brand, H. J., Sui, R., Thomson, S. J., Furukawa, T., & Ebelhar, M. W. (2016). Cotton yield estimation using very high-resolution digital images acquired with a low-cost small unmanned aerial vehicle. *Transactions of the ASABE*, 59(6), 1563-1574.
44. Nebiker, S., Annen, A., Scherrer, M., & Oesch, D. (2008). A light-weight multispectral sensor for micro UAV—Opportunities for very high resolution airborne remote sensing. *Int. Arch. Photogramm. Remote Sens. Spat. Inf. Sci*, 37(B1), 1193-1200.
45. Calderón, R., Montes-Borrego, M., Landa, B. B., Navas-Cortés, J. A., & Zarco-Tejada, P. J. (2014). Detection of downy mildew of opium poppy using high-resolution multi-spectral and thermal imagery acquired with an unmanned aerial vehicle. *Precision Agriculture*, 15(6), 639-661.
46. Zhang, L., Zhang, H., Niu, Y., & Han, W. (2019). Mapping maize water stress based on UAV multispectral remote sensing. *Remote Sensing*, 11(6), 605.
47. Park, S., Ryu, D., Fuentes, S., Chung, H., Hernández-Montes, E., & O’Connell, M. (2017). Adaptive estimation of crop water stress in nectarine and peach orchards using high-resolution imagery from an unmanned aerial vehicle (UAV). *Remote Sensing*, 9(8), 828.
48. Bian, J., Zhang, Z., Chen, J., Chen, H., Cui, C., Li, X., ... & Fu, Q. (2019). Simplified evaluation of cotton water stress using high resolution unmanned aerial vehicle thermal imagery. *Remote Sensing*, 11(3), 267.
49. Ma, Y., Zhang, Q., Yi, X., Ma, L., Zhang, L., Huang, C., ... & Lv, X. (2022). Estimation of cotton leaf area index (LAI) based on spectral transformation and vegetation index. *Remote Sensing*, 14(1), 136.
50. Jiang, J., Cai, W., Zheng, H., Cheng, T., Tian, Y., Zhu, Y., ... & Yao, X. (2019). Using digital cameras on an unmanned aerial vehicle to derive optimum color vegetation indices for leaf nitrogen concentration monitoring in winter wheat. *Remote Sensing*, 11(22), 2667.
51. Yang, S., Hu, L., Wu, H., Ren, H., Qiao, H., Li, P., & Fan, W. (2021). Integration of crop growth model and random forest for winter wheat yield estimation from UAV hyperspectral imagery. *IEEE Journal of Selected Topics in Applied Earth Observations and Remote Sensing*, 14, 6253-6269.
52. Taddia, Y.; Stecchi, F.; Pellegrinelli, A. Coastal mapping using DJI Phantom 4 RTK in post-processing kinematic mode. *Drones* **2020**, 4, 9.
53. Nagendran, S.K.; Tung, W.Y.; Ismail, M.A.M. Accuracy assessment on low altitude UAV-borne photogrammetry outputs influenced by ground control point at different altitude. In *IOP Conference Series: Earth and Environmental Science, Proceedings of*

*the 9th IGRSM International Conference and Exhibition on Geospatial & Remote Sensing (IGRSM 2018), Kuala Lumpur, Malaysia, 24–25 April 2018*; IOP Publishing: Bristol, UK; Volume 169, p. 012031.

54. Park, J.W.; Yeom, D.J. Method for establishing ground control points to realize UAV-based precision digital maps of earthwork sites. *J. Asian Archit. Build. Eng.* **2022**, *21*, 110–119.
55. Awasthi, B.; Karki, S.; Regmi, P.; Dhimi, D.S.; Thapa, S.; Panday, U.S. Analyzing the Effect of Distribution Pattern and Number of GCPs on Overall Accuracy of UAV Photogrammetric Results. In *Lecture Notes in Civil Engineering, Proceedings of the International Conference on Unmanned Aerial System in Geomatics, Roorkee, India, 6–7 April 2019*; Jain, K., Khoshelham, K., Zhu, X., Tiwari, A., Eds.; Springer: Cham, Switzerland; pp. 339–354.
56. Mirko, S.; Eufemia, T.; Alessandro, R.; Giuseppe, F.; Umberto, F. Assessing the Impact of the Number of GCPS on the Accuracy of Photogrammetric Mapping from UAV Imagery. *Balt. Surv.* **2019**, *10*, 43–51.

## Chapter 2 Optimization of Ground Control Point Distribution for Unmanned Aerial Vehicle Photogrammetry in Farming Land

### 2.1 Introduction

Remote sensing employing unmanned aerial vehicles (UAVs) is becoming a popular and trustworthy technology for both users and researchers in many technical fields. UAVs have an extremely high observation resolution compared with satellite remote sensing data, and higher efficiency and utility than laser scanning remote sensing. These advantages have made UAV one of the most optimal platforms for local regional scale remote sensing. The rapid developments in both engineering and sensor technology have enabled UAVs to contribute to a variety of uses, such as constructing three-dimensional terrain models of mountainous areas [1], water bodies [2], farming land [3,4,5], forests [6,7,8,9,10], and artificial structures [11], as well as estimating biomass storage of wood or grass resources [12,13], monitoring crop growth status [14], grasping the condition of disaster areas [15], and evaluating ecosystem service [16].

When a highly accurate topographic map is required, or the photographs of a certain area taken by multi-temporal surveys need to be overlapped and compared to see dynamic changes, the position information of the UAV remote sensing data must be corrected and optimized. This is because the position information obtained by the geographic positioning system (GPS) equipped on UAV has a limited accuracy, which may be unstable due to the weather or satellite signal reception [17].

The use of ground control points (GCPs) is one of the most commonly used methods to correct the position information of UAV imagery. With this method, several GCPs are set inside or around the subject area, for which coordinates (x, y, z) are measured by precise positioning equipment such as the real-time kinematic global navigation satellite system (RTK-GNSS). Before the UAV photography is conducted, anti-aircraft signs are placed on the GCPs, so that the points can be identified from the UAV photographs. The position information of the photographs is corrected afterwards during the bundle adjustment within the Structure-from-Motion (SfM) software by inputting the correct coordinates of the GCP [18].

Although the use of GCPs contributes greatly to the accuracy of photogrammetric products (such as orthomosaic and digital surface models), settlement and measure of the GCPs are time-consuming works. Therefore, UAVs with global navigation satellite system real-time kinematic (GNSS-RTK) on board have been gathering attention [19]. Specifically, the UAV post-processed kinematic (PPK) and real-time kinematic (RTK) are two kinds of technologies that are commonly used for the direct georeferencing, and the accuracy could be very close to that of the projects using a reasonable GCP distribution [20,21,22,23].

However, the elevation error of these approaches varies significantly depending on the experimental equipment and the object surface morphology, resulting in an unstable elevation accuracy [24], and a double-grid oblique flight in differential mode is required to achieve the similar accuracy with the GCP method [25]. There are still also limitations to these approaches. For example, the network transmission (NRTK) which supports the real-time differential correction of RTK is easily affected by the long reference distance when the flight path of the UAV is long [26]. Moreover, during the SfM procedure, when the UAV data are expressed as a vertical ‘doming’ of the surface, which is caused by a combination of near-parallel imaging directions, the absence of GCPs can easily lead to a systematic broad-scale error (as known as the dome effect) [27]. Furthermore, in practice, UAVs with GNSS-RTK onboard are still costly, which restricts their wider use in developing countries or rural areas. Based on this background, the utilization of GCPs is still necessary for UAV photogrammetry to meet the requirement of sustainable resource management.

There are many previous studies of the influence on the GCP setting to the horizontal or vertical accuracy of the SfM products. Evaluating the quality of GCP setting is a complex task because many variables have to be taken into consideration. Over the years, various studies have analyzed the effect of the number and spatial configurations of the GCPs used for indirect georeferencing [28,29,30,31,32,33,34,35,36,37]. Most of the above research assumes that the higher the number of GCP used, the better the overall accuracy. For example, Mirko et al. (2019) tested the accuracy obtained from various photogrammetric workflows in 3D modeling of a coastline georeferencing. The results showed that 3 GCPs are needed for reasonable georeferencing, efficient results may be obtained using 6–7 GCPs, and more than 15 GCPs are necessary to produce accurate cartographic works [38].

However, the number of GCPs is not the only variable that affects the calibration accuracy. The position of each GCP used is also a crucial factor that needs to be considered during the surveys. For example, Oniga et al. assessed the UAV photogrammetric accuracy using different GCP settings at an urban area of about 1 ha in Romania. The results not only showed that a higher number of GCPs improves the accuracy, but also suggested the facts such as the GCPs in the corners of the study site are essential, placing the GCPs along the border of the study block is not optimal, and interior GCPs are improving the accuracy significantly [39]. Awasthi et al. (2020) discussed the accuracy of UAV-based photogrammetric products in corridor mapping and area with undulating terrain for different sets of GCP settings. The results showed that the GCPs should be established in places covering all elevations with a minimum of five GCPs in the shape of a die [40]. Cabo et al. (2021) used generalized additive models (GAMs) to analyze the relationship between the root mean squared error (RMSE) and the mean absolute error (MAE) in the Z coordinate in a group of checkpoints and in a set of covariates related to the number and spatial distribution of GCPs. As a result, among the different predictor variables (describing GCP number and distribution), the number of GCPs had the greatest influence on vertical accuracy. Other variables such as mean distance

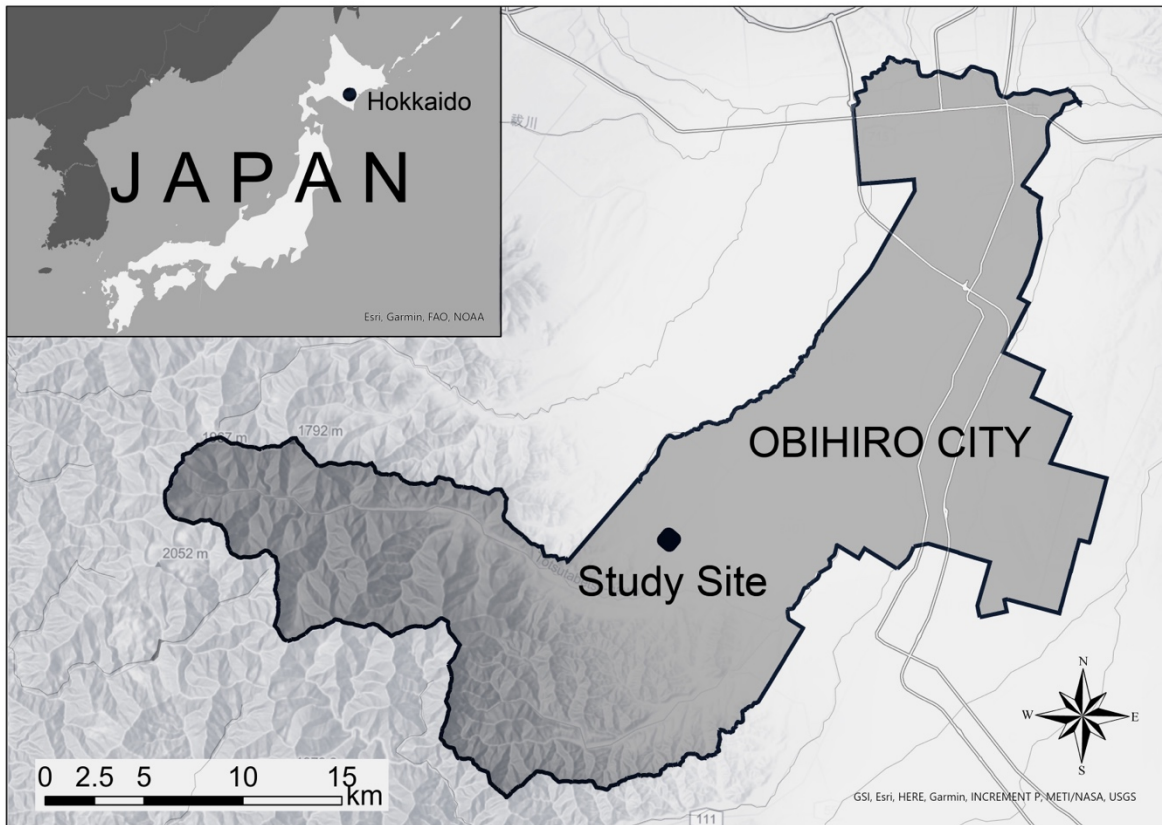
between control points or distance of checkpoints from their nearest GCP contribute much less to explaining RMSE and MAE [41]. Villanueva and Blanco (2019) presented a method for assessing the impact of GCP distribution, quantity, and inter-GCP distance on the output digital elevation model (DEM) by utilizing SfM and GIS. The results showed that the best configuration was the evenly distributed GCP set, configurations clumped to the edge and distributed to the edge had the lower accuracy, and those configurations clumped to the center yielded the worst accuracy [36]. Furthermore, the Geographical Survey Institute of Ministry of Land, Infrastructure, Transport, and Tourism of Japan also suggests that at least four GCPs should be used and must be set both surrounding and inside the subject area to obtain satisfactory accuracy for public surveying with UAV [42]. However, none of the previous studies above has covered all the variables that affect the quality of GCP setting, such as the number of GCPs, the distance between GCPs, or the distribution configuration of GCPs.

Furthermore, most of the previous studies have agreed that GCPs should be evenly spaced around the subject area if possible, and the more GCPs are used, the higher the accuracy is expected. However, the most basic aim and advantage of UAV remote sensing is to observe areas that are difficult or impossible for investigators to enter. For example, for land surveys, it is difficult to set the GCP on artificial structures; in the case of forest surveys, the anti-aircraft signals cannot be recognized even if the GCPs are placed and measured inside the forest; in the case of ecosystem service surveys, it is impossible to set stable GCPs at the center of a water body such as lakes or rivers; and for agricultural surveys, setting GCPs inside the crops is destructive for the growing plants and will cause disruptions to field management. Therefore, it is necessary to acknowledge that in many surveying sites, only the outer edges of the subject area are available for GCP placement. Based on this reality, the current study aims to create a standard to evaluate the quality of GCP setting to provide a guideline for researchers or surveyors of UAV photogrammetry to decide the most optimal number and spatial configuration of GCPs without intruding into the subject area.

## 2.2 Methodology

### 2.2.1 Study site

The survey for this study was conducted at an experimental field located in the agricultural area of Obihiro City, Hokkaido, Japan (Latitude: 42.3728°, Longitude: 142.9985°, Elevation: 261 m above sea level, **Figure 2.1**). The study site was approximately 300 × 400 m (12 ha), with the elevation change of 7.5 m. The experimental field was selected as the study area because the difference in elevation was small, so that the topographic factor would not have significant influence on the georeferencing error. Moreover, it was a typical sample of cropland or grassland, which would be an inaccessible area during the growing season of the crop.



**Figure 2.1 Study site location.**

### 2.2.2 Data collection

The field survey was conducted on 21 August 2021. The weather was sunny, and the wind speed was less than 2 m/s during the whole survey period. As shown in **Figure 2.2**, twelve GCPs were evenly distributed at the outer edge of the study site. The distance between two nearest GCPs was between 48 m and 144 m. However, twenty checkpoints were evenly distributed across the whole area of the field. The anti-aircraft signals were placed on the GCPs and checkpoints. The size of the anti-aircraft signals for GCPs was 60 × 60 cm, while the size of those for checkpoints was 35 × 35 cm (**Figure 2.3**). All the points had a clear view of the sky and maintained a distance of at least 5 m from the trees or houses.



**Figure 2.2 Distribution of GCPs and check points inside the study site.**



**Figure 2.3 Anti-aircraft signals (Left: For GCPs; Right: For check points).**

The coordinates of the GCPs and the checkpoints were determined using an RTK-GNSS receiver (Hiper V, TOPCON, Tokyo, Japan) in real-time kinematic mode. The distance between the study site and the nearest electronic reference point (Taisho Town, Obihiro City) was 9.43 km. The antenna height of the receiver was 1.80 m above ground (**Figure 2.4**). According to the manufacturer of the RTK-GNSS equipment, the MAE of the measured coordinates was expected to be 10 mm horizontally and 15 mm vertically. The GCP and check point coordinates were used to correct the position information of the UAV photogrammetry results and verify the accuracy of the corrected photogrammetry results, respectively.



**Figure 2.4 RTK-GNSS (TOPCON HiperV) measuring.**

The UAV photography was conducted after the GCPs and checkpoints were placed and measured. The UAV used in this study was the Inspire 2 (DJI Inc., Shenzhen, China, **Figure 2.5**). The camera used to obtain the RGB imagery was the Zenmuse X5S (9–45 mm, resolution:  $5280 \times 3956$ ). During photography, the camera angle was set to be vertical downward. Two flights were conducted to capture the whole field area because of the battery limitation. Both flights were flown based on the same parameters using an auto flight application Pix4D capture (Pix4D, Lausanne, Swiss). The flying altitude was 50 m above ground; the overlap was 70% by top and 70% by side. The total flying time was 31 min 23 s and total flying distance was 10.045 km, covering a total area of 16 ha and collecting 780 images.



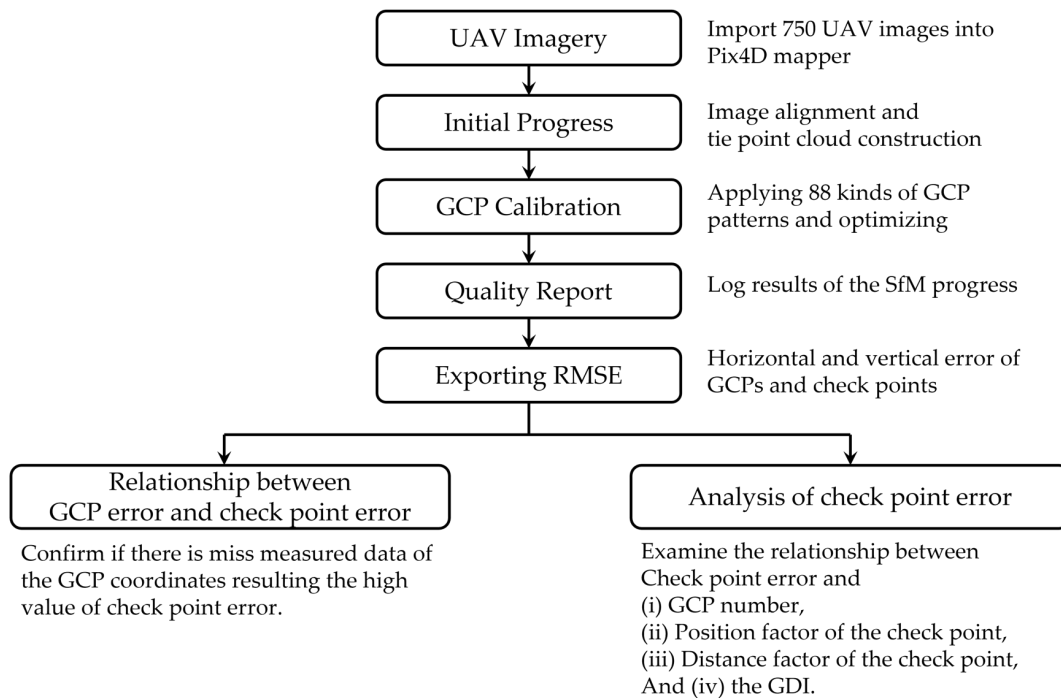
**Figure 2.5 UAV photography with Inspire2 at the study site.**



## 2.2.3 Data Processing

### 2.2.3.1 Workflow

The data process workflow is shown in **Figure 2.6**. The UAV imagery was processed using an SfM software (Pix4D mapper ver 4.5.6, Pix4D, Lausanne, Swiss). After inputting the images into the software, the initial step of SfM, which is the bundle adjustment including the image alignment and camera parameters viewpoint calculation, was performed. Next, the three-dimensional tie point cloud describing the surface model of the object area was constructed. The tie point cloud included the sparse points with 3D coordinates acquired from the GPS information of the UAV images. Subsequently, a high-density point cloud was constructed based on this sparse tie point cloud. Then, as the final production of the SfM, a digital surface model (DSM) and orthomosaic was constructed based on the high-density point cloud. Therefore, to provide accurate position information to these photogrammetry results, the position calibration using a well-distributed GCP set needs to be applied right after the tie point cloud is constructed. To discuss the optimal GCP establishment, this study has created 88 kinds of GCP set patterns with different GCP number and distribution. Each GCP pattern was then used to calibrate tie point cloud derived from the original UAV images at the SfM software, and the calibrating accuracy were compared to reveal the effect by GCP distribution on the georeferencing accuracy. The details of these GCP patterns are introduced in the **Section 2.3.2**.



**Figure 2.6 Data process workflow.**

After inputting the GCP information and optimizing the tie point cloud, the software exported a quality report including the bundle adjustment details (the calculated camera position, overlap, and number of key points matches) and geolocation details of the process so far for each GCP pattern. The geolocation details included the Error X, Error Y, and Error Z of both GCPs and check points. Error X stands for the difference between the computed GCP/check point 3D point and the original position obtained from UAV images in the X direction (original position—computed position); the same process was followed for the Error Y and Error Z. For clarity, this study uses “horizontal error” and “vertical error” to stand for the difference between the computed GCP/check point and the original position in horizontal and vertical directions. The calculation for horizontal error is shown in Equation (1). The value of vertical error was the same as that for Error Z.

$$\text{Horizontal Error} = \sqrt{(\text{Error X})^2 + (\text{Error Y})^2} \quad (1)$$

Then, the Horizontal Error and Vertical Error of both GCPs and check points (20 points) were evaluated. During the error evaluation step, the relationship between the GCP and check point errors was examined. There is a possibility that the measurement of the GCP coordinated with RTK-GNSS may have outliers. If there were any missed data used to calibrate the point cloud, the calibration result would be misdirected and lose their reliability and reproducibility. To ensure that there were no missing data among the GCPs, the correlation between the error of each GCP and the error of all the check points was determined. If a few GCPs was mismeasured, then the error of these mismeasured GCPs would have a higher correlation with the error of the test points.

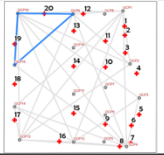
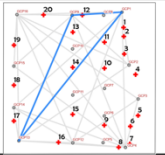
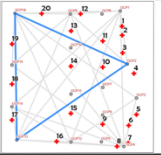
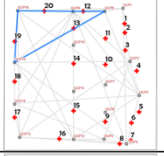
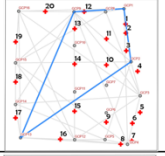
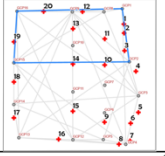
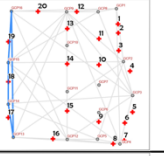
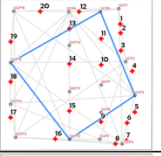
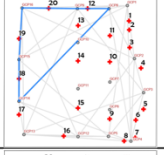
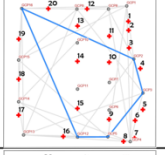
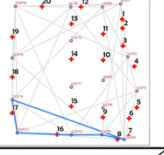
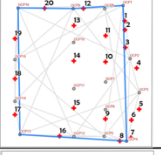
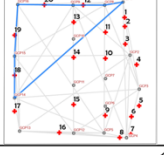
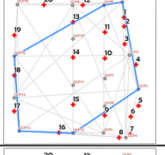
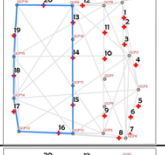
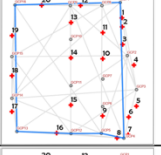

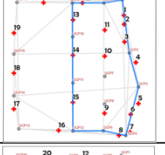
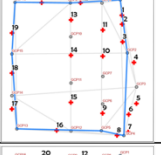
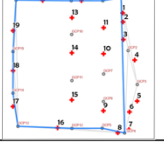
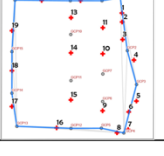
Finally, the evaluation of the twenty check points was conducted. To fully assess the calibration effect of the GCP patterns, this study discussed four GCP distribution factors that affect the accuracy of the check points: the GCP number, position of the check points, distance between the check points and the GCPs, and GCP distribution index (GDI). The details of the GDI calculation are explained in **Section 2.2.3.3**.

#### 2.2.3.2. GCP Patterns

The 88 GCP patterns were separated to six groups due to the number of GCPs that were used. These six groups were named the 3-GCP Group (twelve patterns), the 4-GCP Group (twenty patterns), the 5 GCP-Group (sixteen patterns), the 6-GCP Group (twenty patterns), the 8 GCP-Group (eleven patterns), and the above-10-GCP Group (nine patterns). Within each group, the GCP patterns were separated into several types based on the configuration of

GCPs, which were the (A) corner, (B) diagonal, (C) half side, (D) straight line, and (E) surrounding types.

Additionally, not all the six groups contained all types. For example, the 3-GCP group did not contain (C) the half side type, because when only three GCPs were used, (C) the half side type was not significantly different from (B) the diagonal type. Similarly, the 8-GCP Group and the above-10-GCP Group did not contain (A) the corner type, because when there were more than eight GCPs applied, it was impossible to distribute them at one corner of the field. Additionally, only the 4-GCP Group and 5-GCP Group contained (D) the straight-line type, because this type was made to discuss the case of settling GCPs at one side of the field, and only the GCP configurations formed by four or five GCPs resembled that scenario. The typical patterns of each group and configuration type are shown at **Figure 2.7**.

Type	(A) Corner type	(B) Diagonal type	(C) Half-side type	(D) Line type	(E) Surrounding type
3-GCP Group					
4-GCP Group					
5-GCP Group					
6-GCP Group					
8-GCP Group					
Above-10-GCP Group					

**Figure 2.7 Typical GCP patterns of each group and each configuration type.**

### 2.2.3.3. GCP Distribution Index Calculation

To recommend the optimal GCP distribution that is applicable to different locations and periods, some studies have described GCP distribution quantitatively using the GCP density. For example, Gindraux et al. (2017) determined  $\rho_{GCP}$  ( $1/\text{km}^2$ ) as the density of GCPs per unit area [41]. However, this method reduced one dimension, which was the spatial bias inside one square kilometer. With this method, as long as the quantity of GCPs inside a certain area was the same, even if they were clumped in the center or distributed at the edges, the GCP density was the same. Knowing the optimal number of GCPs calculated by the optimal GCP density, users of UAV photogrammetry still face the problem of how to distribute the GCPs. It is a crucial problem, because the configuration of GCPs also has a significant effect on the photogrammetric accuracy [39]. In this study, the GDI has been used to quantify the GCP distribution considering not only their quantity but also their spatial bias. The GDI was calculated by Equation (2).

$$GDI = \frac{Area_{GCP}}{Area_{Whole}} \times Number_{GCP} \quad (2)$$

In this equation,  $Area_{GCP}$  [ $\text{m}^2$ ] indicates the area surrounded by GCPs, while  $Area_{Whole}$  [ $\text{m}^2$ ] indicates the whole subject site. When the number of GCP is the same, the larger the area surrounded by GCPs, the higher the GDI value. However, when the area surrounded by GCPs is the same, the more GCPs are used, the higher the GDI value.

## 2.3. Results

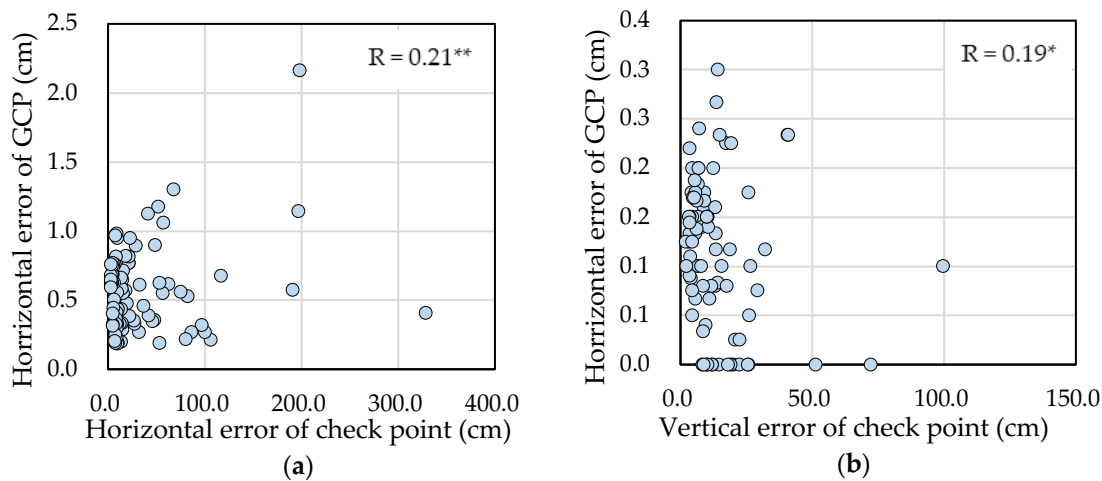
### 2.3.1. Relationship between GCP Error and Check Point Error

The coordinates of twelve GCPs and twenty check points measured by RTK-GNSS (Table 2.1) were used as the reference data to calculate the GCP error and check point error. The coordinate system used in this study was the Japan Geodetic Datum 2011 (JGD2011)/Japan Plane Rectangular CS XIII. The relationship between GCP error and check point error is shown in Figure 2.8. The correlation coefficient of horizontal errors was 0.21\*, suggesting the horizontal error of GCPs and check points had a low correlation. Furthermore, the  $p$  value of the correlation between the vertical error of GCPs and check points was 0.065, suggesting that the vertical GCP error had no significant correlation with the vertical check point error.

These results suggested that the GCP coordinate error had no significant effect on the check point error. This proved that the check point error was not caused mismeasured GCP coordinates, but by the distribution configuration or quantity of GCPs and check points.

**Table 2.1 Coordinates of GCPs and check points.  
JGD2011/Japan Plane Rectangular CS XIII.**

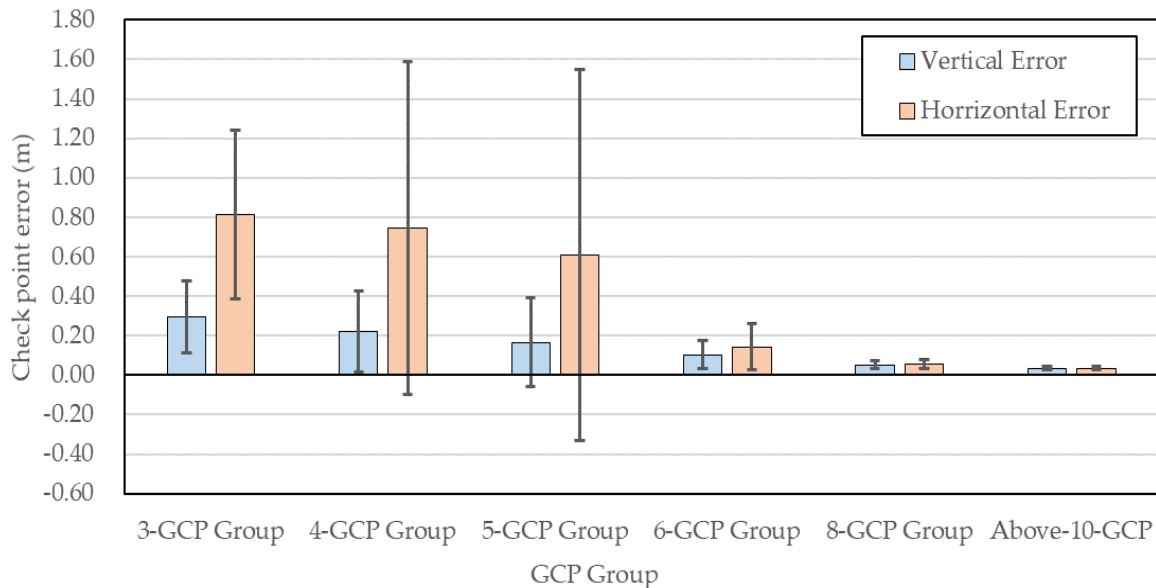
No.	X (m)	Y (m)	Z (m)
GCP 01	-139,952.522	-102,272.435	256.863
GCP 02	-140,070.595	-102,347.832	256.432
GCP 03	-140,154.070	-102,386.420	258.195
GCP 04	-140,230.000	-102,493.170	261.535
GCP 05	-140,182.974	-102,530.043	262.111
GCP 06	-140,131.528	-102,482.524	260.648
GCP 07	-140,076.385	-102,436.148	259.196
GCP 08	-139,928.018	-102,314.091	256.773
GCP 09	-139,875.156	-102,377.220	257.424
GCP 14	-139,962.953	-102,649.875	260.426
GCP 15	-139,879.514	-102,579.624	260.368
GCP 16	-139,781.105	-102,486.545	258.573
Check Point 01	-139,986.148	-102,295.145	255.291
Check Point 02	-140,004.484	-102,309.756	255.227
Check Point 03	-140,040.503	-102,338.486	255.722
Check Point 04	-140,100.647	-102,350.477	256.539
Check Point 05	-140,187.101	-102,414.480	259.264
Check Point 06	-140,195.925	-102,448.142	260.514
Check Point 07	-140,230.253	-102,478.878	261.134
Check Point 08	-140,218.267	-102,506.576	261.775
Check Point 09	-140,149.903	-102,498.298	261.168
Check Point 10	-140,035.921	-102,402.136	258.011
Check Point 11	-139,983.693	-102,358.083	257.232
Check Point 12	-139,892.041	-102,356.891	257.200
Check Point 13	-139,910.263	-102,404.505	258.142
Check Point 14	-139,980.764	-102,464.030	259.577
Check Point 15	-140,075.091	-102,543.271	261.686
Check Point 16	-140,107.254	-102,618.705	263.118
Check Point 17	-139,989.584	-102,672.110	260.428
Check Point 18	-139,917.891	-102,611.724	260.960
Check Point 19	-139,837.641	-102,544.269	259.622
Check Point 20	-139,826.454	-102,434.035	257.530



**Figure 2.8 Relationship between GCP error and check point error: (a) Horizontal error; (b) Vertical error (\*\*:  $p$ -value < 0.01; \*:  $0.01 \leq p$ -value < 0.05).**

### 2.3.2. Relationship between GCP Number and Check Point Error

**Figure 2.9** shows the relationship between the number of GCPs and check point error (horizontal and vertical). For all GCP groups, the vertical check point error was lower than the horizontal error. This was because the study site was flat with little difference in elevation. Both vertical and horizontal error decreased with the increase in the GCP number. In particular, the horizontal error decreased significantly from 0.611 m to 0.144 m when the GCP number increased from five to six. This suggested that for a subject field with the area of approximately 10 ha, using at least six GCPs would efficiently improve the calibration compared to using less than five.



**Figure 2.9 Relationship between GCP number and mean check point error.**

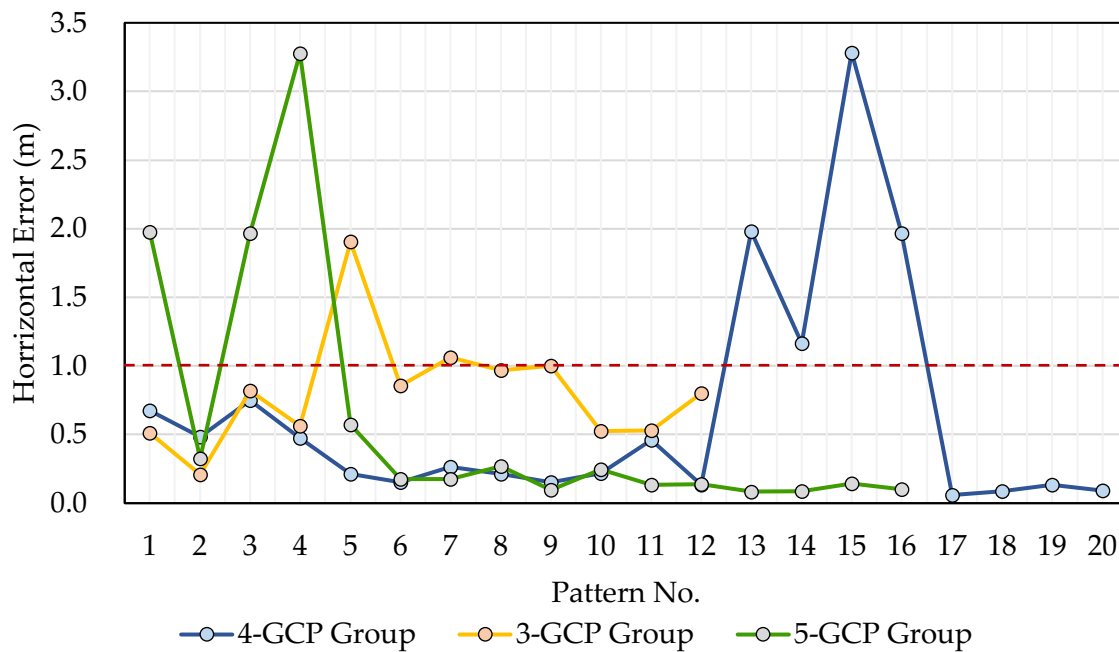
However, even though the average horizontal error of the 3-GCP Group, 4-GCP Group, and 5-GCP Group was significantly higher than the groups with more GCPs, it did not mean that all the patterns with three, four, or five GCPs had low calibration. As shown in **Figure 9**, all the three groups had an extremely high standard deviation (STDEV) value of the check point error. The STDEV for the 4-GCP Group and 5-GCP Group (0.884 m and 0.940 m, respectively) was even larger than the mean horizontal error (0.813 m and 0.744 m, respectively). This implied that even when the GCP number was the same, different GCP patterns had varied check point errors, indicating that the GCP number should not be the only factor considered when determining the optimal GCP distribution.

### 2.3.3. Relationship between GCP Configuration Type and Check Point Error

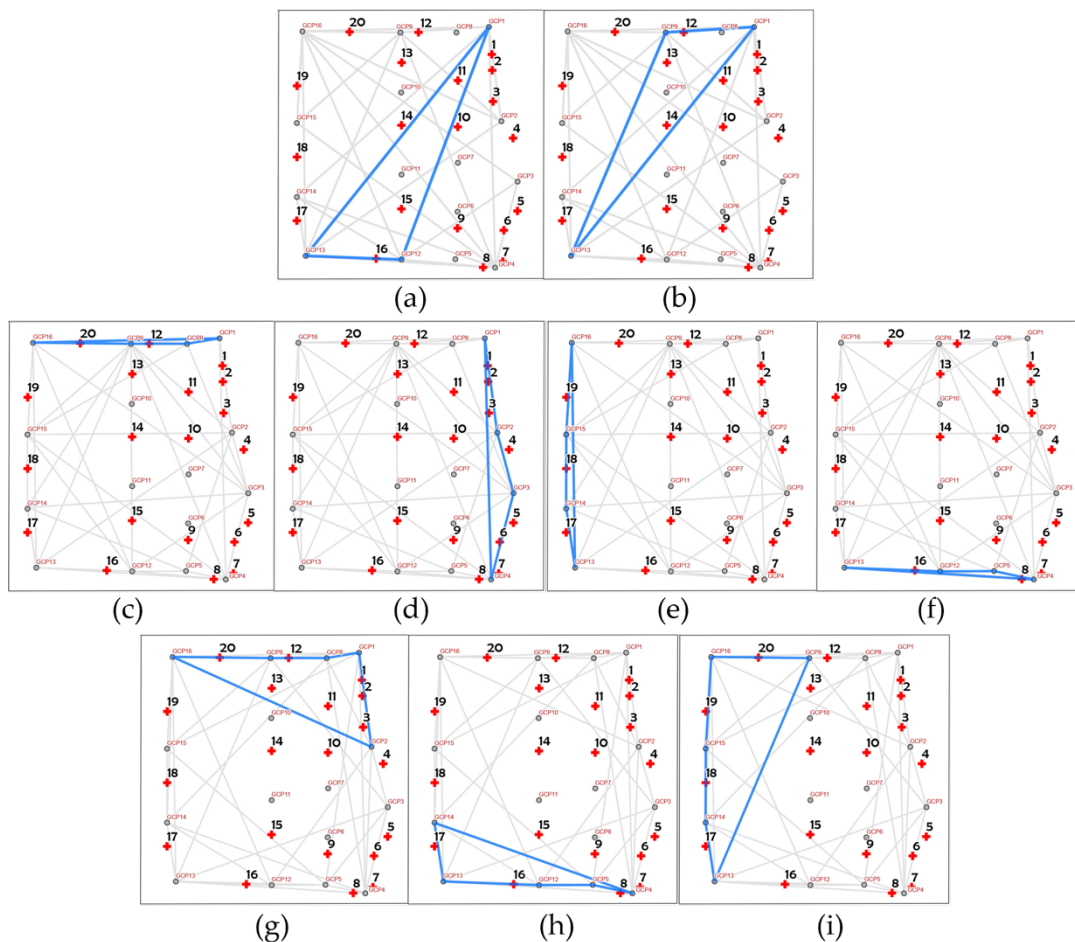
Because **Figure 2.9** indicated that the both the mean horizontal error and the STDEV of the 3-GCP Group, 4-GCP Group, and 5-GCP Group were particularly high, the mean horizontal error of each GCP pattern in these groups are shown in **Figure 2.10** to identify the specific GCP patterns with extremely high horizontal error. As shown in **Figure 2.10**, the horizontal error of Pattern 05 and Pattern 07 in the 3-GCP Group; Patterns 13–16 in the 4-GCP Group; and Pattern 01, Pattern 03, and Pattern 04 in the 5-GCP Group was obviously larger than 1.0 m and was significantly different from the other patterns in the same group. Even with the same GCP number, there were certain distribution configurations of GCPs that might cause high calibration error, which was further proof that the number or density cannot



be the main factor to determine the optimal GCP placement. To discuss the characteristic of the GCP patterns that may cause large calibration error, the configuration of the GCP patterns with above-1.0 m-horizontal error are shown in **Figure 2.11**.



**Figure 2.10 Horizontal error of each GCP pattern in the 3-GCP Group, 4-GCP Group, and 5-GCP Group.**



**Figure 2.11 GCP patterns with above-1.0 m-horizontal error: (a) Pattern 05, 3-GCP Group; (b) Pattern 07, 3-GCP Group; (c) Pattern 13, 4-GCP Group; (d) Pattern 14, 4-GCP Group; (e) Pattern 15, 4-GCP Group; (f) Pattern 16, 4-GCP Group; (g) Pattern 01, 5-GCP Group; (h) Pattern 03, 5-GCP Group; (i) Pattern 04, 5-GCP Group.**

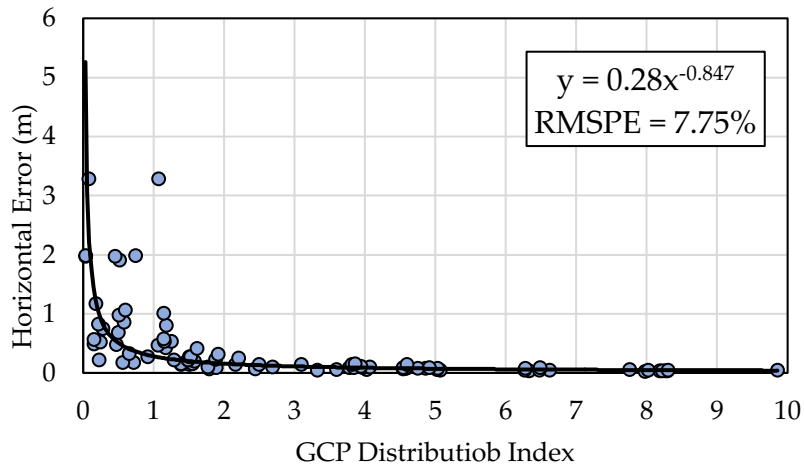
As shown in **Figure 2.11**, the GCP patterns with above-1.0-horizontal error belonged to the diagonal type in the 3-GCP Group and to the line type in 4-GCP Group and 5-GCP Group. Both the diagonal and line types had the same aspect ratio characteristic (the rate of the longest side to the height, which is vertical to it) and was the highest within their group. As shown in **Figure 2.11**, the GCP configuration of these patterns was long and narrow, especially for those in the line type in the 4-GCP Group, which were nearly a straight line. As shown in **Figure 2.10**, all the GCP patterns in the 4-GCP Group had stable, high calibration accuracy, except for the four-line type patterns. This result suggested that the higher the aspect rate of the GCP configuration, the lower the calibration accuracy would be, and the GCP patterns forming a straight line had the worst calibration accuracy.

#### 2.3.4. Describing the Calibration Ability of GCPs by GDI

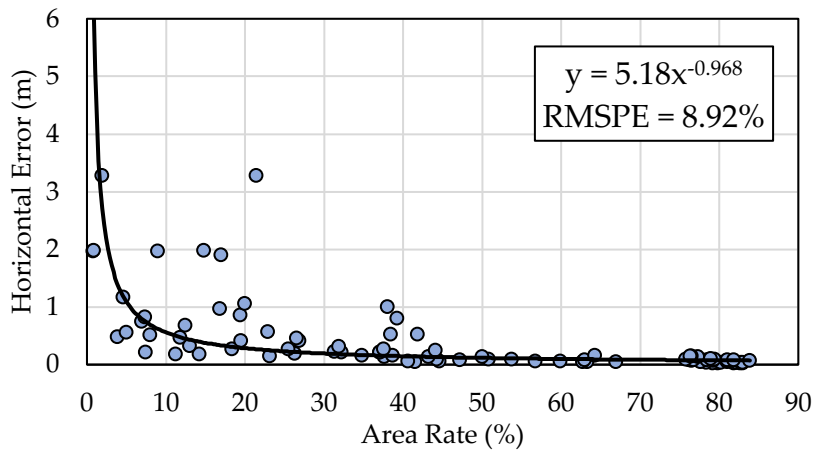
As noted, when the available GCPs were comparatively less, such as the 3-GCP Group, 4-GCP Group, and 5-GCP Group, the aspect rate was a useful factor when considering the optimal GCP placement. However, when the available GCPs were enough to form a well-balanced polygon, such as the 6-GCP Group, the 8-GCP Group, and the above-10-GCP Group, the distribution configuration of GCPs would not form long and narrow shapes because there were enough polygon apexes. Although the shape of distribution configuration was no longer a main factor that affected the calibration accuracy, the horizontal error still varied for different GCP patterns. For example, as shown in **Figure 2.9**, the STDEV of the 6-GCP Group was 0.116 m, which was almost equal to the average horizontal error (0.144 m). This suggested that there was a factor other than the number and configuration shape of GCPs that affected the calibration accuracy. This factor is considered to be the area ratio surrounded by GCPs.

When the numbers of GCPs are the same, and the shapes of the GCP configuration have no distinguishing characteristics, the main difference between the GCP patterns is the surrounding area. However, when the surrounding area remains constant, the number of GCPs also results in varied calibration accuracy. To integrate the effect on calibration accuracy of these two factors, this study has suggested a new parameter to describe the calibration ability of GCP, which is the GDI.

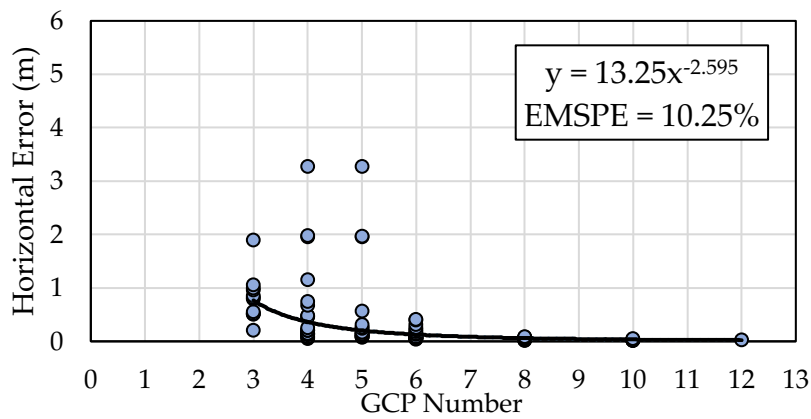
As shown in Equation (2), the GDI is the product of the rate of the area surround by GCPs and the number of GCPs. The larger the GDI value, the larger the calibration accuracy of the GCPs. When the number of GCPs is low, surrounding a larger area with these GCPs may improve the accuracy. Similarly, even with enough GCPs, if the area surrounded by GCPs is extremely small, the accuracy will be low. A proof of this is that the line type had the lowest accuracy among both the 4-GCP Group and the 5-GCP Group. The relationship among horizontal error and GDI, the rate of the area surrounded by GCPs, and the number of GCPs are shown in **Figure 2.12**. Among these three factors describing the distribution of GCPs, GDI had the highest coefficient of determination ( $EMSPE = 7.75\%$ ), while both the area rate and the GCP number had large variation for estimating the horizontal error ( $RMSPE = 8.92\%$  and  $10.25\%$ ). This result showed that as the product by the area rate and the number of GCPs, GDI was more qualified than the rest for describing the calibration ability of GCPs. To provide a reference for optimal GCP distribution determination, the horizontal error was classified into five ranks, which are shown in **Table 2.2** with the average GDI, area rate, and GCP number relevant to each of them. This reference table indicates that to guarantee an accuracy with a horizontal error  $< 10$  cm, the GCP distribution containing seven GCPs and surrounding 70% of the subject area is recommended. The specific number or surrounding area rate of GCPs may fluctuate, but the GDI should be maintained at approximately five. With the decrease in GDI, the expected horizontal error becomes larger. When the value of GDI is  $< 0.5$ , the horizontal is expected to be  $> 0.5$  m.



(a)



(b)



(c)

**Figure 2.12 Relationship between the factors describing GCP distribution: (a) GDI; (b) Rate of area surrounded by GCPs; (c) Number of GCPs.**

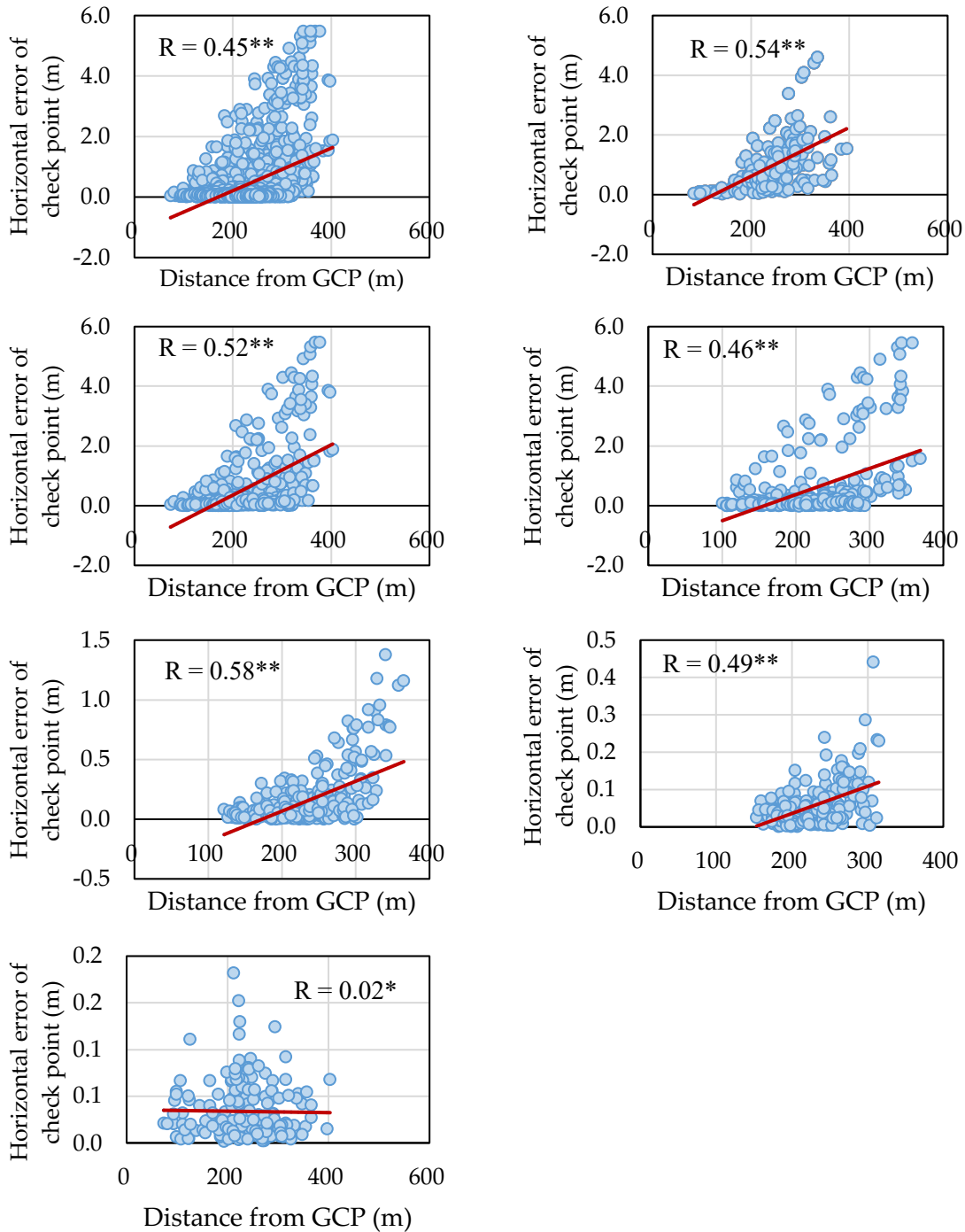
**Table 2.2 Reference value of GDI, area rate, and number of GCPs of each rank of horizontal error.**

Rank No.	Horizontal Error (m)	GDI	Area Percentage	GCP Number
10-cm-Rank	0.06	5.36	71%	7
20-cm-Rank	0.148	2.33	47%	5
30-cm-Rank	0.313	1.22	25%	5
40-cm-Rank	0.689	0.654	20%	3
50-cm-Rank	1.958	0.483	13%	4

### 2.3.5. Relationship between the Position of Check Point Distance and Check Point Error

To provide practical proposal for more accurate UAV photogrammetry, this study has not only focused on the placement of GCPs, but also discussed the effect of the check point position on the photogrammetry accuracy. There are two factors relating to the position of the check points: the distance between the check points and the GCPs and the positional relation between check points and the area surrounded by GCPs.

In this study, the relationship between the horizontal error of the check points and these two factors were determined. **Figure 2.13** shows the relationship between the horizontal check point error and the average distance between each check point and three nearest GCPs for all the twenty check points in each GCP pattern for every GCP group. Within every group, the correlation coefficient was less than 0.6, suggesting that there was no significant correlation between the horizontal error and the distance between GCPs and check points.



**Figure 2.13 Relationship between the horizontal error and the distance between GCPs and the check point: (a) All patterns; (b) 3-GCP-Group; (c) 4-GCP-Group; (d) 5-GCP Group; (e) 6-GCP Group; (f) 8-GCP Group; (g) Above-10-GCP Group (\*\*:  $p$ -value < 0.01; \*:  $0.01 \leq p$ -value < 0.05).**

Then, the positional relation between check points and the area surrounded by GCPs was discussed. The positional relation was classified into three types: outside (check point was outside the area surrounded by GCPs), inside (check point was inside the area surrounded by GCPs), and between (check point was located between two GCPs). **Table 2.3** shows the average horizontal error of check points of these three types for each GCP group. Within each GCP group, the outside check point type had the highest horizontal error, the inside check point type had the lower horizontal error, and the between type had the lowest horizontal error. This suggested that GCPs had better calibration effect for the subjects that were located inside the area surrounded by them and had the highest calibration accuracy when the subject was between two GCPs. This result indicated that if there is a particular subject that needs high photographic accuracy, the optimal GCP placement is to situate the subject between two GCPs. If that is hard to achieve, then having the subject inside the area surrounded by GCPs may provide moderate accuracy.

**Table 2.3 Average horizontal error of check points of these three types for each GCP group (m).**

	<b>3-GCP Group</b>	<b>4-GCP Group</b>	<b>5-GCP Group</b>	<b>6-GCP Group</b>	<b>8-GCP Group</b>	<b>Above-10-GCP Group</b>
Outside	0.873	0.769	0.449	0.218	0.074	0.035
Inside	0.728	0.125	0.128	0.083	0.054	0.031
Between	0.247	0.118	0.060	0.062	0.037	0.027

## 2.4 Discussion

UAV remote sensing is not just an engineering science, it is also a tool for the researchers and common users from all kinds of fields and occupations, such as sociology, environmental assessment, and agriculture. If the basic accuracy verification is conducted without considering the actual situation these non-professional users are facing, the existence of UAV remote sensing will be meaningless outside the academic world.

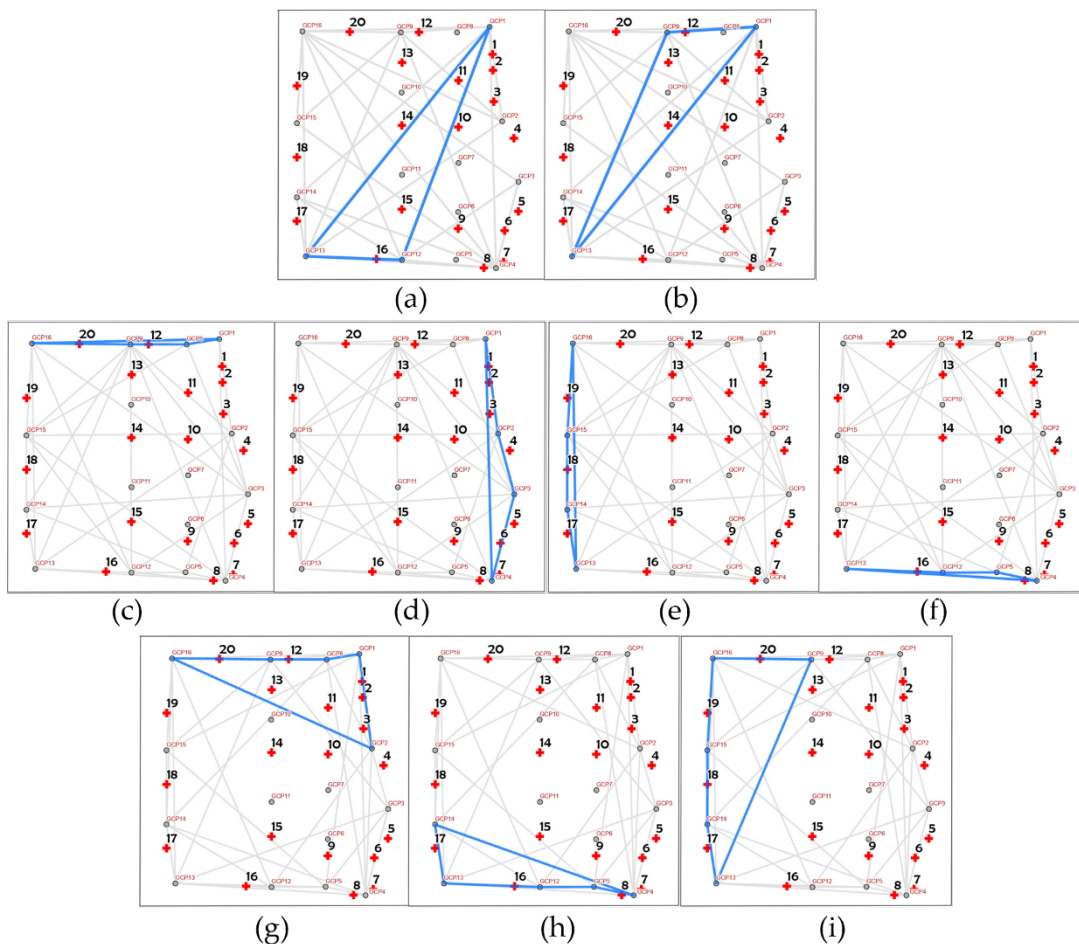
Many studies have discussed the optimal GCP distribution for UAV photogrammetry. However, when it comes to survey sites in open land or rural areas, the subject field is sometimes difficult or impossible for surveyors to enter due to the variety of environments and may be why photogrammetry by UAV is needed. In these cases, the theoretical optimal GCP distribution with GCPs inside the survey field cannot be put to practical use. In fact, many researchers or users of UAV worry about the photogrammetric accuracy when they cannot place GCPs inside the field. Sometimes, they have to put the GCPs along the road because it is the only place that is possible to set the anti-aircraft signals, but they do not

know how much this special GCP configuration can correct the position information of the whole field. With these doubts, they cannot fully trust the accuracy of the photogrammetric production, and in worst cases, the whole UAV survey may be in vain. Furthermore, even if they managed to set some GCPs around the field, they have doubts such as if the GCPs can correct the position information of the subjects from far away. These researchers and users need reference data to tell them how to obtain the optimal GCP calibration effect even without the internal GCPs, and if they must place the GCPs in a special configuration such as a straight line or a little triangle, on what level the photogrammetric error will be. With this kind of reference, the UAV photogrammetry results can be clarified and start contributing to all fields of study. This is exactly the motivation of this study.

In this study, 88 GCP distribution patterns with different configurations using three, four, five, six, eight, ten, and twelve GCPs were applied for the UAV photographs of a 12 ha field to discuss the optimal GCP distribution in an inaccessible field.

The results show that when the GCP number was less than six, the shape of GCP configuration was a main factor affecting the calibration accuracy of the GCPs. Specifically, the higher the aspect ratio of the GCP configuration, the lower the calibration accuracy. As an extreme case, when four GCPs were used, the GCP configuration with all GCPs forming a straight line had very high horizontal error (2.099 m on average), which was over seven times that of the other configurations also using four GCPs (0.285 m on average). The reason the straight-line type of GCP configuration was discussed in this study is that it is a case that often occurs in UAV surveys. When the whole subject area is difficult to enter or there is no significant object on the ground inside the field, such as a forest, grassland, or lake, the most convenient method is to establish GCPs along the road near the field, because there are many significant objects such as signals and cracks on the road, and it is easy to install the anti-aircraft signals because the road is flat and has no obstacles on it. However, based on the result of this study, placing GCPs along the road will result in a low calibration accuracy because the GCPs will form a straight line. In such cases, it is better to arrange the GCPs into a well-balanced triangle or rectangle with low aspect ratio, such as the corner, diagonal, half-side, or surrounding type shown in **Figure 2.7**. If the field is totally inaccessible, setting the GCPs in the corner to form a right triangle will obtain better accuracy than setting the GCPs along the road. It is the same when only three GCPs are used. In the 3-GCP Group, the corner type had much better accuracy (average horizontal error = 0.526 m) than the diagonal type (average horizontal error = 1.198 m), because the aspect ratio of the diagonal type was higher than the corner type. When only three GCPs are available, putting them as an equilateral triangle or a right triangle will obtain better accuracy than an obtuse triangle (**Figure 2.14**).





**Figure 2.14 GCP patterns and horizontal error ( $E_{horizontal}$ ) for the 3-GCP Group.**

When there are more than eight available GCPs, the shape of the GCP configuration is no longer a main factor affecting the GCP calibration accuracy because the configurations formed by more than six vertices tend to have no significant aspect ratio value. However, different GCP patterns still have variable accuracy. The factor that affects the GCP calibration accuracy when more than six GCPs are used is the rate of the area surrounded by GCPs. However, the area rate cannot be the only factor explaining the accuracy, because when the area rate stays consistent, the more GCPs used, the higher the accuracy. To integrate these two factors, this study proposed the GDI (the product of area rate and GCP quantity) to describe the ability of GCP calibration when the GCP number is more than six. According to the results, GDI was better at describing the horizontal checkpoint error and thus the GCP calibration accuracy than the area rate and GCP quantity. When surveyors have doubts about the error level of their UAV photogrammetric products, they can calculate the GDI and find the corresponding error value shown in **Table 2.3**. Similarly, if they want to achieve a certain

level of accuracy and have doubts about what kind of GCP distribution is suitable, they can also calculate the area rate the GCPs should surround using the GCP number. Furthermore, when evaluating former studies or reports using UAV photogrammetry with certain GCP distributions, readers can gain insight into the error level using this reference table. This provides a standard to evaluate the accuracy of UAV photogrammetric results, which have often been subjective.

The last factor that affected the GCP calibration accuracy was the position of the measurement subjects. Normally, it is considered that the farther the subject is from the GCPs, the lower the accuracy will be. However, the results showed that distance between subjects and GCPs was not the main factor affecting the accuracy because the correlation between the GCP-check point distance and horizontal error was low ( $R = 0.45$ ). Instead of the distance between the subjects and GCPs, the positional relation is more impactful on the GCP calibration accuracy. Locating the subject inside the area that is surrounded by GCPs will efficiently increase the photogrammetric accuracy. However, if the subject is located between two GCPs, it will obtain the best accuracy. When a certain object instead of the whole survey land needs to be measured accurately, surveyors tend to surround the object with GCPs. Based on the results of this study, this placement of GCPs will not provide the best accuracy and placing GCPs on two sides of the object of interest is preferred.

Recently, UAV remote sensing technology has been utilized for resource monitoring in multidisciplinary fields, such as agricultural and land resources, fisheries resources, forests, agroforestry, ecosystem services, etc. It still has the potential to contribute to the transdisciplinary processes of collaborative monitoring of various natural resources with societal stakeholders due to its high-cost performance ratio, high mobility, high image resolution, and user friendliness without many difficulties in operations. However, the UAV survey with high precision is still limited in the field of information engineering and is facing difficulty in being popularized in other science fields, including transdisciplinary knowledge co-creations. This is due to the uncertain survey procedure caused by differences between various study sites. The cross-cutting between the engineering fields that focus on improving remote sensing precision and the other fields which use remote sensing technology as an approach of knowledge creation is necessary. The current study has not only introduced the common methodology of using GCPs, which is a crucial factor to improve UAV survey precision, but also created a standard of settling GCPs properly in inaccessible areas, which helps diverse users of UAV photogrammetry to obtain more reliable UAV remote sensing data at the different study sites. Furthermore, through the effective utilization of high-precision and high-resolution remote sensing data in inaccessible areas such as forests, grasslands, water bodies, coastal areas, and protected areas, it is hopeful to achieve better-integrated management of these areas through transdisciplinary collaborations with researchers of diverse disciplines and societal stakeholders. The results and proposals made in this study are useful for cross-cutting between the UAV remote sensing engineering and

other practical science fields, substantially contributing to sustainable community development based on transdisciplinary integration of agricultural and other natural resource management systems by popularizing the precise UAV photogrammetry.

#### **4.5 Conclusions of this chapter**

This study was conducted using UAV photography and RTK-GNSS equipment at an experimental field (12 ha) located in Obihiro City, Hokkaido, Japan on 24 August 2021. The calibration ability of 88 GCP pattern repetitions was verified to discuss the optimal method to determine the GCP distribution.

Results show that when the available GCPs are less than six, the aspect ratio of the GCP configuration is the main factor affecting the accuracy. A lower aspect ratio is recommended to achieve better accuracy. When there are more than six available GCPs, the GDI is the proper factor to describe the GCP calibration ability. The higher the GDI, the higher the accuracy.

This study also provided a table of reference data to predict the error value with GDI. With this indicator, the georeferencing accuracy is predictable with the GCP number and GCP area. Moreover, according to the concept of GDI, the optimal distribution of GCPs can reduce the necessary number of GCPs to achieve a certain accuracy, and by which improve the efficiency of UAV photogrammetric surveys. In addition, further study on applying the GDI at challenging terrains such as a mountainous area is required.

Finally, referring to the positional relation between the object and GCPs, this study indicated that setting GCPs on two sides of an object may improve the calibration effect more than setting GCPs around it when a certain object needs to be measured.

These results and suggestions are expected to help researchers and societal stakeholders employing UAV photogrammetry obtain more trustworthy data, which can contribute to their research and practices. By providing one improvement for natural resource users and managers to perform accurate monitoring under challenging conditions, the results of this study can hopefully help improve monitoring accuracy at inter- and transdisciplinary studies of sociology, forestry, agriculture, and engineering surveys, which contributes to the development of an integrated resource monitoring system.

## Reference

1. Piras, M.; Taddia, G.; Forno, M.G.; Gattiglio, M.; Aicardi, I.; Dabove, P.; Lo Russo, S.; Lingua, A. Detailed geological mapping in mountain areas using an unmanned aerial vehicle: Application to the Rodoretto Valley, NW Italian Alps. *Geomat. Nat. Hazards Risk* **2017**, *8*, 137–149.
2. Manfreda, S.; McCabe, M.F.; Miller, P.E.; Lucas, R.; Pajuelo Madrigal, V.; Mallinis, G.; Dor, E.B.; Helman, D.; Estes, L.; Ciruolo, G.; et al. On the use of unmanned aerial systems for environmental monitoring. *Remote Sens.* **2018**, *10*, 641.
3. Bendig, J.; Yu, K.; Aasen, H.; Bolten, A.; Bennertz, S.; Broscheit, J.; Gnyp, M.L.; Bareth, G. Combining UAV-based plant height from crop surface models, visible, and near infrared vegetation indices for biomass monitoring in barley. *Int. J. Appl. Earth Obs. Geoinf.* **2015**, *39*, 79–87.
4. Bareth, G.; Bendig, J.; Tilly, N.; Hoffmeister, D.; Aasen, H.; Bolten, A. A comparison of UAV-and TLS-derived plant height for crop monitoring: Using polygon grids for the analysis of crop surface models (CSMs). *Photogramm. Fernerkund. Geoinf.* **2016**, *2016*volume?, 85–94.
5. Zhang, K.; Tsuji, O.; Kimura, M.; Muneoka, T.; Hoshiyama, K. Monitoring of Crop Plant Height Based on DSM Data Obtained by Small Unmanned Vehicle Considering the Difference of Plant Shapes. *Int. J. Environ. Rural. Dev.* **2020**, *11*, 131–136.
6. Zhang, Y.; Wu, H.; Yang, W. Forests growth monitoring based on tree canopy 3D reconstruction using UAV aerial photogrammetry. *Forests* **2019**, *10*, 1052.
7. Zhang, Y.; Yang, W.; Zhang, W.; Yu, J.; Zhang, J.; Yang, Y.; Lu, Y.; Tang, W. Two-step ResUp&Down generative adversarial network to reconstruct multispectral image from aerial RGB image. *Comput. Electron. Agric.* **2022**, *192*, 106617.
8. Zhang, Y.; Yang, W.; Sun, Y.; Chang, C.; Yu, J.; Zhang, W. Fusion of multispectral aerial imagery and vegetation indices for machine learning-based ground classification. *Remote Sens.* **2021**, *13*, 1411.
9. Zhang, W.; Gao, F.; Jiang, N.; Zhang, C.; Zhang, Y. High-Temporal-Resolution Forest Growth Monitoring Based on Segmented 3D Canopy Surface from UAV Aerial Photogrammetry. *Drones* **2022**, *6*, 158.
10. Sankey, T.; Donager, J.; McVay, J.; Sankey, J.B. UAV lidar and hyperspectral fusion for forest monitoring in the southwestern USA. *Remote Sens. Environ.* **2017**, *195*, 30–43.

11. Martinez, J.G.; Gheisari, M.; Alarcón, L.F. UAV integration in current construction safety planning and monitoring processes: Case study of a high-rise building construction project in Chile. *J. Manag. Eng.* **2020**, *36*, 05020005.
12. Zheng, H.; Cheng, T.; Zhou, M.; Li, D.; Yao, X.; Tian, Y.; Cao, W.; Zhu, Y. Improved estimation of rice aboveground biomass combining textural and spectral analysis of UAV imagery. *Precis. Agric.* **2019**, *20*, 611–629.
13. Guan, S.; Fukami, K.; Matsunaka, H.; Okami, M.; Tanaka, R.; Nakano, H.; Sakai, T.; Nakano, K.; Ohdan, H.; Takahashi, K. Assessing Correlation of High-Resolution NDVI with Fertilizer Application Level and Yield of Rice and Wheat Crops Using Small UAVs. *Remote Sens.* **2019**, *11*, 112.
14. Hildmann, H.; Kovacs, E. Using unmanned aerial vehicles (UAVs) as mobile sensing platforms (MSPs) for disaster response, civil security and public safety. *Drones* **2019**, *3*, 59.
15. James, M.R.; Robson, S.; d'Oleire-Oltmanns, S.; Niethammer, U. Optimising UAV topographic surveys processed with structure-from-motion: Ground control quality, quantity and bundle adjustment. *Geomorphology* **2017**, *280*, 51–66.
16. Bendig, J.; Bolten, A.; Bareth, G. 4 UAV-based Imaging for Multi-Temporal, very high Resolution Crop Surface Models to monitor Crop Growth Variability. *Unmanned Aer. Veh. (UAVs) Multi-Temporal Crop Surf. Model.* **2013**, *44*, 53–69.
17. Yang, J.; Li, X.; Luo, L.; Zhao, L.; Wei, J.; Ma, T. New Supplementary Photography Methods after the Anomalous of Ground Control Points in UAV Structure-from-Motion Photogrammetry. *Drones* **2022**, *6*, 105.
18. Taddia, Y.; Stecchi, F.; Pellegrinelli, A. Coastal mapping using DJI Phantom 4 RTK in post-processing kinematic mode. *Drones* **2020**, *4*, 9.
19. Žabota, B.; Kobal, M. Accuracy assessment of uav-photogrammetric-derived products using PPK and GCPs in challenging terrains: In search of optimized rockfall mapping. *Remote Sens.* **2021**, *13*, 3812.
20. Hugenholtz, C.; Brown, O.; Walker, J.; Barchyn, T.; Nesbit, P.; Kucharczyk, M.; Myshak, S. Spatial accuracy of UAV-derived orthoimagery and topography: Comparing photogrammetric models processed with direct geo-referencing and ground control points. *Geomatica* **2016**, *70*, 21–30.
21. Fazeli, H.; Samadzadegan, F.; Dadrasjavan, F. Evaluating the Potential of RTK-UAV for Automatic Point Cloud Generation in 3D Rapid Mapping. *Int. Arch. Photogramm. Remote Sens. Spat. Inf. Sci.* **2016**, *41*, 221–226.

22. Štroner, M.; Urban, R.; Reindl, T.; Seidl, J.; Brouček, J. Evaluation of the georeferencing accuracy of a photogrammetric model using a quadcopter with onboard GNSS RTK. *Sensors* **2020**, *20*, 2318.
23. Taddia, Y.; González-García, L.; Zambello, E.; Pellegrinelli, A. Quality assessment of photogrammetric models for façade and building reconstruction using DJI Phantom 4 RTK. *Remote Sens.* **2020**, *12*, 3144.
24. Teppati Losè, L.; Chiabrando, F.; Giulio Tonolo, F. Boosting the timeliness of UAV large scale mapping. Direct georeferencing approaches: Operational strategies and best practices. *ISPRS Int. J. Geo-Inf.* **2020**, *9*, 578.
25. James, M.R.; Robson, S. Mitigating systematic error in topographic models derived from UAV and ground—Based image networks. *Earth Surf. Processes Landf.* **2014**, *39*, 1413–1420.
26. Nikolakopoulos, K.G.; Kyriou, A.; Koukouvelas, I.K. Developing a Guideline of Unmanned Aerial Vehicle’s Acquisition Geometry for Landslide Mapping and Monitoring. *Appl. Sci.* **2022**, *12*, 4598.
27. Meinen, B.U.; Robinson, D.T. Mapping erosion and deposition in an agricultural landscape: Optimization of UAV image acquisition schemes for SfM-MVS. *Remote Sens. Environ.* **2020**, *239*, 111666.
28. Tonkin, T.N.; Midgley, N.G. Ground-control networks for image based surface reconstruction: An investigation of optimum survey designs using UAV derived imagery and structure-from-motion photogrammetry. *Remote Sens.* **2016**, *8*, 786.
29. Bolkas, D. Assessment of GCP number and separation distance for small UAS surveys with and without GNSS-PPK positioning. *J. Surv. Eng.* **2019**, *145*, 04019007.
30. Mestas-Carrascosa, F.J.; Rumbao, I.C.; Berrocal, J.A.B.; Porrás, A.G.F. Positional quality assessment of orthophotos obtained from sensors onboard multi-rotor UAV platforms. *Sensors* **2014**, *14*, 22394–22407.
31. Ulvi, A. The effect of the distribution and numbers of ground control points on the precision of producing orthophoto maps with an unmanned aerial vehicle. *J. Asian Archit. Build. Eng.* **2021**, *20*, 806–817.
32. Liu, X.; Lian, X.; Yang, W.; Wang, F.; Han, Y.; Zhang, Y. Accuracy assessment of a UAV direct georeferencing method and impact of the configuration of ground control points. *Drones* **2022**, *6*, 30.

33. Sanz-Ablanedo, E.; Chandler, J.H.; Rodríguez-Pérez, J.R.; Ordóñez, C. Accuracy of unmanned aerial vehicle (UAV) and SfM photogrammetry survey as a function of the number and location of ground control points used. *Remote Sens.* **2018**, *10*, 1606.
34. Nagendran, S.K.; Tung, W.Y.; Ismail, M.A.M. Accuracy assessment on low altitude UAV-borne photogrammetry outputs influenced by ground control point at different altitude. In *IOP Conference Series: Earth and Environmental Science, Proceedings of the 9th IGRSM International Conference and Exhibition on Geospatial & Remote Sensing (IGRSM 2018), Kuala Lumpur, Malaysia, 24–25 April 2018*; IOP Publishing: Bristol, UK; Volume 169, p. 012031.
35. Park, J.W.; Yeom, D.J. Method for establishing ground control points to realize UAV-based precision digital maps of earthwork sites. *J. Asian Archit. Build. Eng.* **2022**, *21*, 110–119.
36. Awasthi, B.; Karki, S.; Regmi, P.; Dhimi, D.S.; Thapa, S.; Panday, U.S. Analyzing the Effect of Distribution Pattern and Number of GCPs on Overall Accuracy of UAV Photogrammetric Results. In *Lecture Notes in Civil Engineering, Proceedings of the International Conference on Unmanned Aerial System in Geomatics, Roorkee, India, 6–7 April 2019*; Jain, K., Khoshelham, K., Zhu, X., Tiwari, A., Eds.; Springer: Cham, Switzerland; pp. 339–354.
37. Mirko, S.; Eufemia, T.; Alessandro, R.; Giuseppe, F.; Umberto, F. Assessing the Impact of the Number of GCPs on the Accuracy of Photogrammetric Mapping from UAV Imagery. *Balt. Surv.* **2019**, *10*, 43–51.
38. Cabo, C.; Sanz-Ablanedo, E.; Roca-Pardiñas, J.; Ordóñez, C. Influence of the number and spatial distribution of ground control points in the accuracy of uav-sfm dems: An approach based on generalized additive models. *IEEE Trans. Geosci. Remote Sens.* **2021**, *59*, 10618–10627.
39. Villanueva, J.K.S.; Blanco, A.C. Optimization of ground control point (GCP) configuration for unmanned aerial vehicle (UAV) survey using structure from motion (SfM). *Int. Arch. Photogramm. Remote Sens. Spat. Inf. Sci.* **2019**, *42*, 167–174.
40. Geographical Survey Institute. *Manual of Public Surveying with UAV*; Ministry of Land, Infrastructure, Transport and Tourism of Japan: Tokyo, Japan, 2017; pp. 23–24.
41. Gindraux, S.; Boesch, R.; Farinotti, D. Accuracy assessment of digital surface models from unmanned aerial vehicles' imagery on glaciers. *Remote Sens.* **2017**, *9*, 186.
42. Yang, H.; Li, H.; Gong, Z.; Dai, W.; Lu, S. Relations between the Number of GCPs and Accuracy of UAV Photogrammetry in the Foreshore of the Sandy Beach. *J. Coast. Res.* **2020**, *95*, 1372–1376.

## **Chapter 3 Monitoring of Crop Plant Height Based on DSM Data Obtained by Small UAV Considering the Difference of Plant Shapes**

### **3.1 Introduction**

Plant Height is an indicator that is strongly related to the resistance of crops to overthrow, biomass, and yield, and reasonable grass height is a guarantee of crop yield [1]. By adding stem thickness and Normalized Difference Vegetation Index (NDVI) to grass height, the biomass of a crop can be estimated and further yield can be predicted [2]. In addition, increasing grass height under the assumption that it does not cause overthrow can increase yield [3]. Besides, grass height of crops can reflect their growing environment, and irrigation and fertilization can be planned rationally by monitoring grass height [4]. Therefore, rapid and accurate monitoring of crop grass height across the field is important for understanding crop growth conditions.

Many research results have been reported on crop growth monitoring worldwide. The main methods used to obtain crop height information include ground surveying, multispectral analysis, and laser surveying. Ground surveying requires the surveyor to enter the growing area of the crop, which inevitably causes damage to the crop. It is also time-consuming and difficult to obtain grass height information for the entire field, since only surveyed values for specific locations can be obtained. Grass height estimation using multispectral data generally uses data acquired by satellites, which has the disadvantages of a long acquisition period and low ground resolution, making it difficult to obtain immediate grass height information. In addition, the accuracy of grass height estimation using multispectral data is not stable because the spectral reflectance of crops differs at each growth stage. Remote sensing by laser surveying has high measurement accuracy, especially for forest tree height, and is an effective tool for measuring tree height and grass height of crops, but the equipment is very expensive, making it difficult to spread to ordinary farmers [5]. Therefore, UAV is thought to be a promising method for monitoring grass height as a remote sensing technology that can observe the entire field at low altitude and is inexpensive.

SfM technology is commonly used to create wide-area scale spatial information using a large number (tens to hundreds) of aerial images taken by UAVs. The process generates a three-dimensional point cloud by generating a three-dimensional point cloud, which is then used to generate a three-dimensional model, orthomosaic, and numerical DSM [6].

In 2013, Bendig et al. used a small rotary-wing UAV (MK-Oktokoper, HI System GmbH) flying at an altitude of 30 m and using a woodpile as a GCP, generated a DSM using image data acquired by an RGB sensor mounted on the UAV, and calculated the difference between the DSM for a level ground condition and proposed a method for estimating the height of barley grass by calculating the difference between the DSM and the DTM. The results were



compared with measured values on the ground, and an estimation accuracy of  $R^2 = 0.69$  was obtained with a coefficient of determination [7,8].

In 2014, the same researcher estimated barley biomass using the DSM estimate of grass height and obtained an accuracy of  $R^2=0.71$ . In 2015, the same researcher modeled biomass by combining DSM with vegetation indices using UAVs and obtained an accuracy of  $R^2 = 0.80\sim 0.82$ .

Zarco-Tejada et al. (2014) used aerial images from an RGB digital camera mounted on a fixed-wing UAV to construct an orthomosaic and a DSM. DSM was constructed to estimate olive tree height. The results were compared with actual measurements and showed a coefficient of determination of  $R^2 = 0.83$ , RMSE = 1.16 m to 4.38 m, and an accuracy of R-RMSE = 11.5% [9]. Teng et al. (2019) flew a UAV (S100, DJI) to 30 m to verify the accuracy of PH by DSM and obtained an estimation accuracy of RMSE = 3.3 cm [10].

Although many validation studies on grass height estimation based on UAV aerial photography data have been conducted around the world in recent years, few studies have examined crops with different stomatal morphologies at the same time, in the same region, and under the same flight conditions. In particular, there have been no studies comparing monocotyledonous and dicotyledonous plants, which differ greatly in leaf morphology and cultivation methods, under the same conditions. For this reason, this study conducted UAV aerial photography and ground-based growth surveys of three crops with distinctive stomatal morphology: Perilla (*dicotyledonous*), Potato (*dicotyledonous*), Reed (*monocotyledonous*), Oat (*monocotyledonous*) and barley (*monocotyledonous*).

When DSM is used to estimate grass height of crops, the differential DSM value is generally lower than the measured grass height; in UAV-based studies, the ground resolution is often a few centimeters, and a pixel in an aerial image represents a few square centimeters of ground objects. On the other hand, the ground resolution of DSM is larger than that of aerial imagery. This means that the DSM generation process is likely to include not only the top of the crop, but also the lower stems, leaves, or ground. In contrast, in actual measurements, it is common to measure the maximum grass height within a specific area. As a result, the DSM measures more detail than the actual measurement, resulting in a lower differential DSM value than the actual measurement.

To address this problem, it is desirable to obtain measured values in a manner more similar to the process of DSM generation than the conventional method of measuring maximum grass height. Many studies have randomly selected measured locations in the plots under study and compared them to the average of the differential DSMs for the entire plot. Not only is it difficult to represent the average grass height of the entire plot at those randomly selected locations, but it is also unstable depending on the individual surveyor. Therefore, it is desirable to extract differential DSMs at locations that match the actual measurement locations as much as possible.

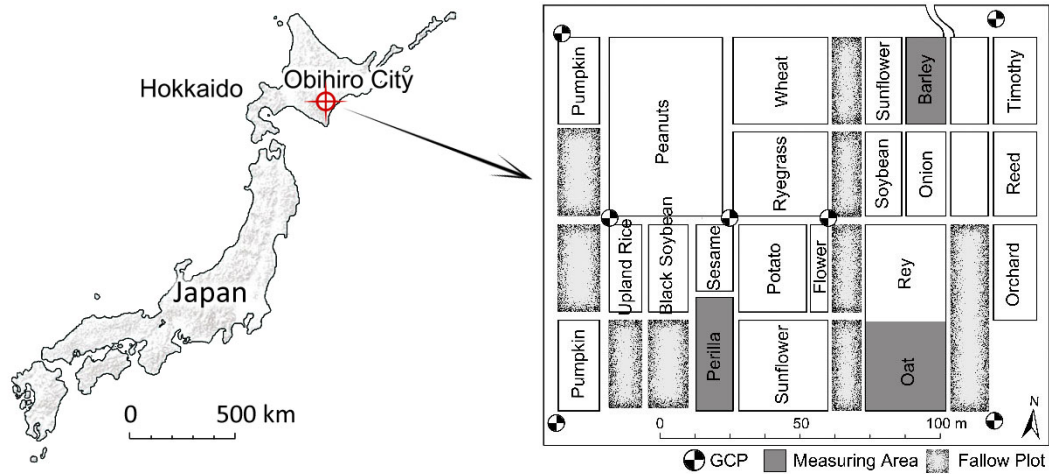
Furthermore, the method of installing wooden stakes on the ground and using them as GCPs is more efficient than installing GCPs and measuring location information at each survey, but the tops of the stakes are a certain distance away from the ground surface, which may cause errors when correcting the DSM as a GCP.

To remedy these problems observed in previous studies, this study used a homemade grass height measuring device, fixed the survey site using a marker pole and orthomosaic, buried the woodpile in the ground, and placed an aerial marker on top of it for use as a GCP. The objective of this study was to improve the accuracy of DSM data and measured data using this improved survey method, and to evaluate the accuracy of grass height estimation using small UAV aerial images with a view to the stem and leaf morphology of the crop, using multiple crops as survey targets.

## 3.2 Methodology

### 3.2.1 Study site

The research plot is located in Obihiro City, Hokkaido, Japan, at longitude 143.1713°E-143.1738°N, latitude 42.8694°N-42.8678°N, and elevation about 77 m (**Figure 3.1**). Hokkaido is the second largest prefecture in the Japanese archipelago (77,983.90 km<sup>2</sup>), the largest and northernmost prefecture in Japan, and the largest food production base. The Tokachi Plain, where Obihiro is located, is on the Pacific Ocean side of eastern Hokkaido, with the Hidaka Mountains to the west, the Daisetsu Mountains to the north, and the Pacific Ocean to the south and east. The prevailing winds are northwesterly in winter and southeasterly in summer. In spring and fall, the winds blow differently during the transition periods from winter to summer and from summer to winter, respectively. In summer, the Pacific high pressure system in the south of Japan extends to the north, and the southeast monsoon brings hot and humid air to the Tokachi Plain, making it hotter. However, depending on the city, the Ogasawara high is weak and an anticyclone with its center in the Sea of Okhotsk appears frequently. This high-pressure system is the base of a decree base, and easterly winds called "Yamase" blow along the Pacific coast. This wind brings summer and exceptional weather to Tokachi. From an agricultural meteorological standpoint, this difference in weather is the main reason why the Tokachi region is a field crop zone.



**Figure 3.1** Location of Study Site

Tokachi agriculture is one of the most specialized field crop farming areas in Hokkaido, as well as in Japan, and there are also some combined field and dairy farming operations. In terms of regions, field crops are predominant in the central region centering on Obihiro City, while dairy and livestock farming are the main businesses in the mountainous and coastal regions. The large-scale, mechanized, and highly productive agriculture has resulted in 39 ha of arable land per farm household, 22 times the national average, and the percentage of farmers by size of arable land is as follows: 20-30 ha (24%), 30-50 ha (39%), 50-100 ha (39%), and 20-30 ha (24%). The percentage of farmers by the size of cultivated land is 24% for 20-30 ha, 39% for 30-50 ha, and 13% for 50-100 ha. The ratio of full-time farmers to sales farmers (farmers with arable land of 30 ha or more or farm product sales of 500,000 ha or more) is 73%, which is overwhelmingly higher than the national figure of 23%. Agricultural output accounts for 24% of Hokkaido's total, with the arable sector accounting for 56% of output and the livestock sector 44%. The main crops in the arable sector are wheat, buckwheat, sugar beets, soybeans, sweet corn, potatoes, and radishes.

The experimental field is rectangular in shape (about 2.8 ha in area), 180 m east-west and 160 m north-south, and is surrounded by a birch windbreak. In the survey year (2019), the entire field was divided into 22 cropping zones (henceforth referred to as fields), including pepo squash, peanut, ricinus, black sesame, sesame, wheat, Italian barley, oyster, sunflower, soybean, barley, onion, rye, wild oats, embak, timothy, reed cana, and Nineteen experimental crops were cultivated (**Figure 2**). This paper describes the results of a survey of five of the cultivated crops with distinctive stomatal morphology: Perilla, Potato, Reed, Oat and Barley.

### 3.2.2 UAV surveys

Prior to conducting the UAV aerial survey, ground control points (GCPs) were established at seven locations throughout the field to measure location information. The GCPs were surveyed on May 28, 2019, from 3:00 p.m. to 4:00 p.m. using the RTK satellite positioning system (Real Time Hiper V), and its positioning accuracy during static positioning mode is 10 mm + 0.5 ppm in the horizontal direction and 15 mm + 1.0 ppm in the vertical direction. The coordinate system used was the Japan Geodetic System 2011. An aerial marker (black and white, 40 cm × 40 m) was placed over the GCPs before each aerial photography to make the GCPs easier to identify.

Immediately prior to conducting the aerial photography survey, the locations and heights of utility poles, trees, and construction objects around the surveyed area were carefully considered to ensure that they would not obstruct the UAV flight. Plant stems and leaves and sand blown up by the Provera's rotation could cause dirt and damage to the aircraft, so a flat and clean area was selected for the UAV takeoff and landing sites, and a heliport was established.

A small rotary-wing UAV (Phantom4 Pro, DJI) was used for aerial photography. The aircraft weighs 1375 g (including the battery and Provera), has a diagonal dimension of 350 mm (not including the propeller), a maximum flight speed of 50 km/h in GPS mode, an operational altitude limit (above sea level) of 6000 m, a maximum wind resistance of 10 m/s, a maximum flight time of approximately 30 minutes, an operating environment The maximum flight time is about 30 minutes, the operating environment temperature is 0 to 40°, and the satellite positioning system is GPS/GNSS. The camera lens has a field of view of 84 m and a maximum wind resistance of 10 m/s. The maximum flight time is approximately 30 minutes. The camera lens on the aircraft has an 84° field of view, 8.8mm/24mm, f/2.8 to f/11, and an autofocus function. The image size of the aerial data was 5472 x 3648 pixels and was saved as JPEG data on a micro SD card.

Aerial photography was conducted using Pix4D Capture (Pix4D, Inc.), a flight planning application dedicated to UAVs, with the following parameters: Above Ground Height (AGB) of 50 m, camera angle of 70° (from the horizontal), and overlap and side wrap rates of 80%. parameters. The flight path was Double Grid, the flight range was approximately 210 x 210 m, the total route length was approximately 6500 m, the flight time was approximately 32 minutes, the stability speed was approximately 4.7 m/s, and the number of satellite captures was 12 to 16. aerial photography was conducted under the same conditions each time. A list of survey dates is shown in **Table 2-2**.

### 3.2.3 Ground surveys

Each ground survey was conducted immediately after the aerial photography or on the following day in the fields of the subject crops. Four to ten measurement points (10 in the barley field, 4 in the wheat field, and 8 in the sorghum field) were placed in the field of each crop to be surveyed, and the locations were marked with a gardening pole (150 cm high and 0.5 cm in diameter) with a pink marking dope (30 cm long).

A self-made device for measuring grass height was used. The measuring device consists of a plastic pole 150 cm long and 28 cm<sup>2</sup> in cross-sectional area and a thin flat plate 0.2 cm thick and 200 cm<sup>2</sup> in area (20 cm long and 10 cm wide). A tape measure is applied to the surface of the plus pole. The flat plate can slide up and down on the pole and rotate horizontally around the pole. When measuring, the measuring device is placed vertically at the measurement point and the flat plate is slid from the top of the measuring device to the top of the crop. The height of the position of the flat plate was recorded when the crop stems and leaves were slightly deformed and the most stems and leaves were in contact with the bottom of the flat plate. The plate is rotated 90° horizontally and surveyed in four different directions with the measurement point at the center. The average of the four measurements was taken as the measured value for this measurement point.

### 3.2.4 Data analysis

An orthomosaic (1.6 cm ground resolution) corrected for location with GCP was introduced in ArcGIS Pro, marking tape was identified to mark the actual measurement point, and vector data (shape file) of the point was created at that location. Since grass height within a radius of 20 cm centered on the measured point was surveyed in the ground survey, a buffer zone of a 40 cm radius circular area centered on the created point shape file was created, taking into consideration the slight deviation between the DSM and orthomosaic and the error due to the height of the measured pole. The buffer zone was then created in ArcGIS Pro. The maximum differential DSM value was used to estimate grass height based on the results of [8].

There is a certain difference between the differential DSM values from UAV aerial images and the measured grass height of the crop, and the extent of this difference is strongly influenced by the stem and leaf morphology of the crop. Therefore, it is necessary to create a linear regression equation between the differential DSM values and the measured values in order to estimate grass height using DSM from UAV aerial photography images. 70% of the survey data was randomly selected as training data and the remaining 30% was used as test data using the scikit-learn module of Python 3.7. The remaining 30% was used as test data. Using the training data, a linear regression estimating equation was created using the least squares method, and the goodness of fit was evaluated using the coefficient of determination

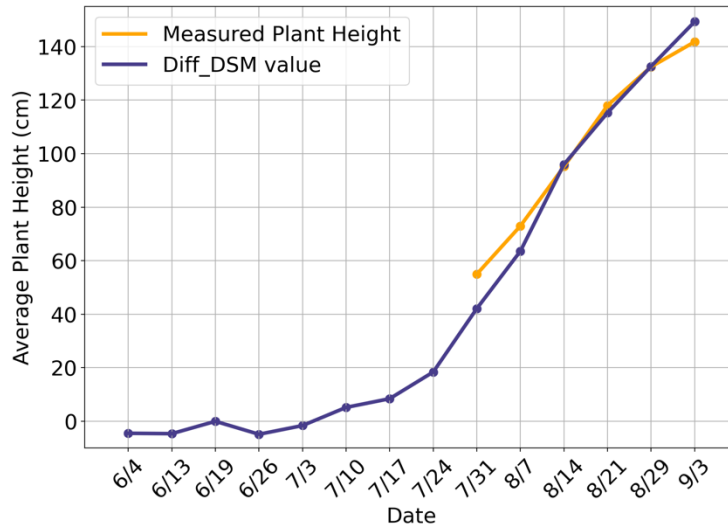
$R^2$  and the root mean squared error RMSE (Root Mean Squared Error). The accuracy of the estimation equation when applied to actual grass height estimation was also verified using test data.

In fields with large crop stubble gaps, the ground surface elevation information in the aerial image causes the DSM to be lower than the actual crop height. Therefore, it is expected that the accuracy of grass height estimation based on differential DSM values will be improved by taking into account the vegetation coverage inside the field. The total number of pixels in the field area ( $P_{total}$ ) is then calculated in the Histogram window. Next, the Color Range function extracts non-green pixels and transfers them to a new layer. Finally, the remaining green pixels ( $P_{green}$ ) were counted and their percentage of the total pixels was used as the vegetation coverage of the field.

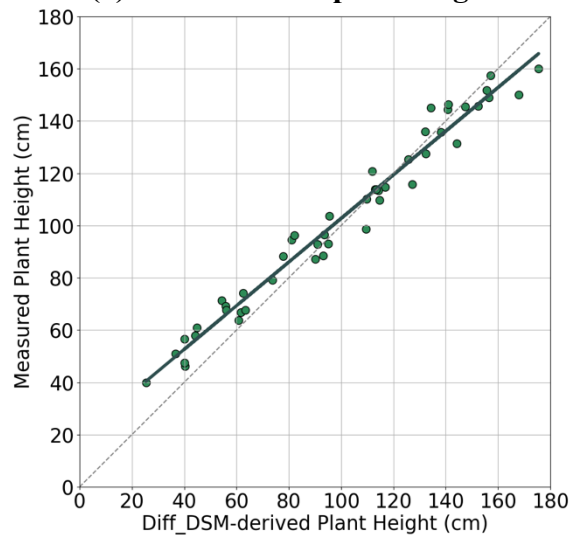
### 3.3 Results and Discussion

#### 3.3.1 Accuracy of estimated plant height for Perilla

**Figure 3.2. (a), (b)** shows the time-series change in plant height and the relationship between the estimated plant height and the measured plant height in the Perilla field. In the Perilla field, the degree of fit between the estimated plant height and the measured plant height is very high ( $R^2 = 0.9721$ ) from the foliage elongation stage to just before flowering. rice field. In recent years, Perilla is a crop that has been attracting attention for its health-enhancing effects. The plant grows as tall as 60cm to 200m, and many branches develop in the leaf axil of the stem. It has strong fertilizing ability and grows vigorously without additional fertilizing or flooding. In order to increase the number of seeds, it is necessary to prevent drooping and pinching. It is thought that the growth characteristics of offspring greatly improved the accuracy of plant height estimation by DSM. From this result, it was found that DSM with 10 cm ground resolution can be applied to grasp the plant height of crops with vigorous growth and tight internodes such as Perilla.



**Figure 3.2 (a) Time series of plant height of Perilla**

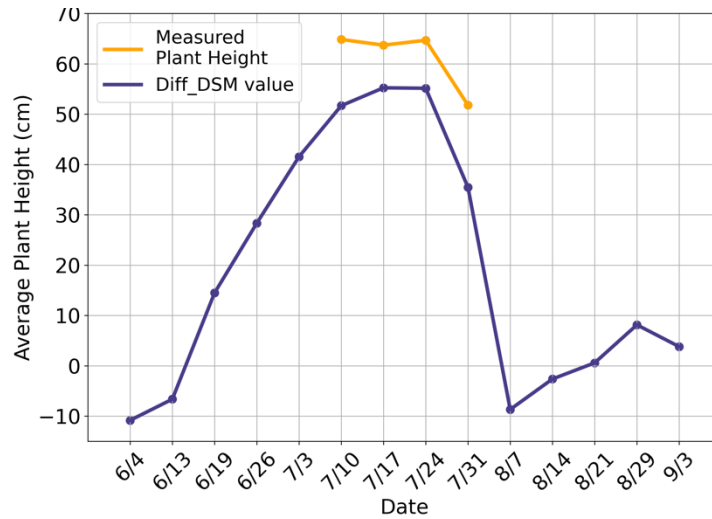


**Figure 3.3 (b) Relationship between the estimated plant height by DSM and measured plant height of Perilla**

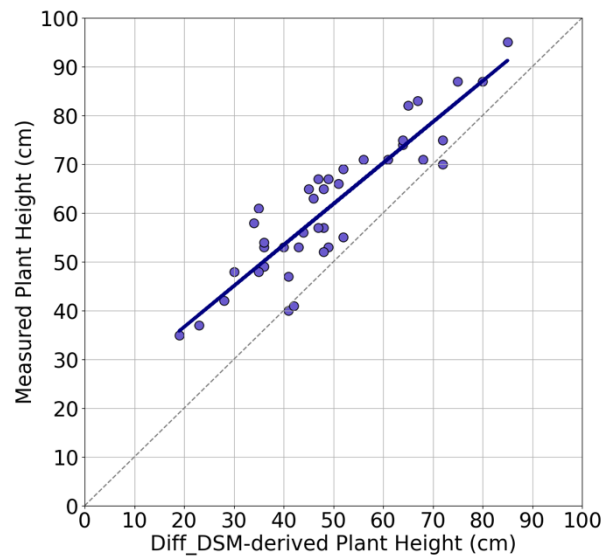
### 3.3.2 Accuracy of estimated plant height for Potato

**Figure 3.4 (a), (b)** show changes in plant height over time in potato fields and the relationship between estimated plant height and measured plant height. In the potato field, a strong correlation ( $R^2=0.82^{**}$ ) was observed between the estimated plant height and the measured plant height from the growing season to harvest. Also, the RMSE was 13.57 cm, which was smaller than that of grass crops. Mature potato leaves are pinnately compound. Such leaf discs usually develop from each node of the stem with two-fifths phyllo taxis, have

long petioles, and 7 to 9 elliptical leaflets are attached to the long petioles to form a compound leaf. In addition, secondary differentiated lobules are attached between these large lobules. Such a compound leaf structure is considered to have improved the accuracy of plant height estimation by DSM. From this result, it was found that DSM with 10cm ground resolution can be used for estimating the plant height of crops with pinnately compound leaves such as potatoes after the growing season.



**Figure 3.4 (a) Time series of plant height of Potato**

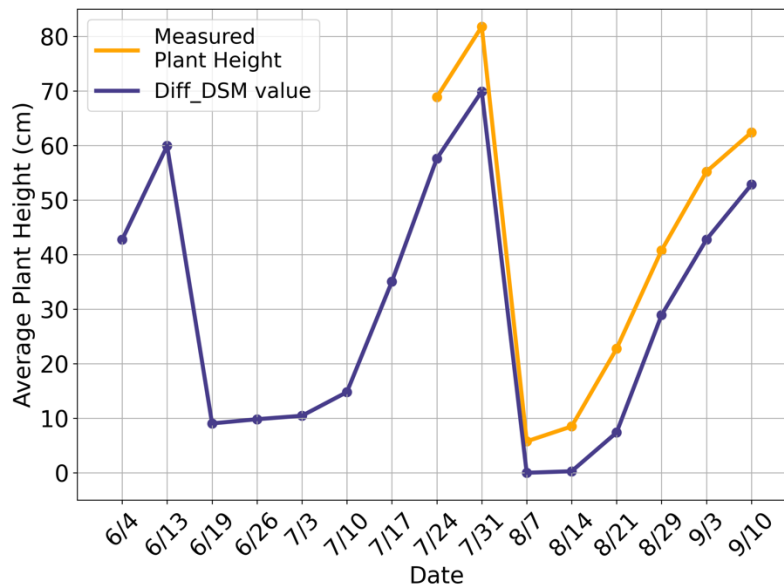


**Figure 3.4 (b) Relationship between the estimated plant height by DSM and measured plan height of Potato**



### 3.3.3 Accuracy of estimated plant height for Reed

**Figure 3.5 (a) and (b)** show changes in plant height over time and the relationship between the estimated plant height and the measured plant height. In pastures, the degree of fitness between the estimated plant height and the measured plant height was very high ( $R^2 = 0.97^{**}$ ) from the second growing season to the third growing season. The RMSE was also relatively low, though stable at 11.70 cm. Concerning the shape of foliage and foliage, grass is cooked with oat, the culm is erect, and the leaves are alternate with broad linear sharp tops. This cultivation method is considered to have improved the accuracy of plant height estimation by DSM. From this, it was found that the DSM with a resolution of 10 cm or more is suitable for estimating the height of crowded pasture grass from the beginning of growth to the time of mowing. In addition, it was found that the error in the estimated plant height for pasture grasses with broad-line sharp tops, 10-35 cm in length and 6-18 mm in width, was always stabilized at about 10 cm.



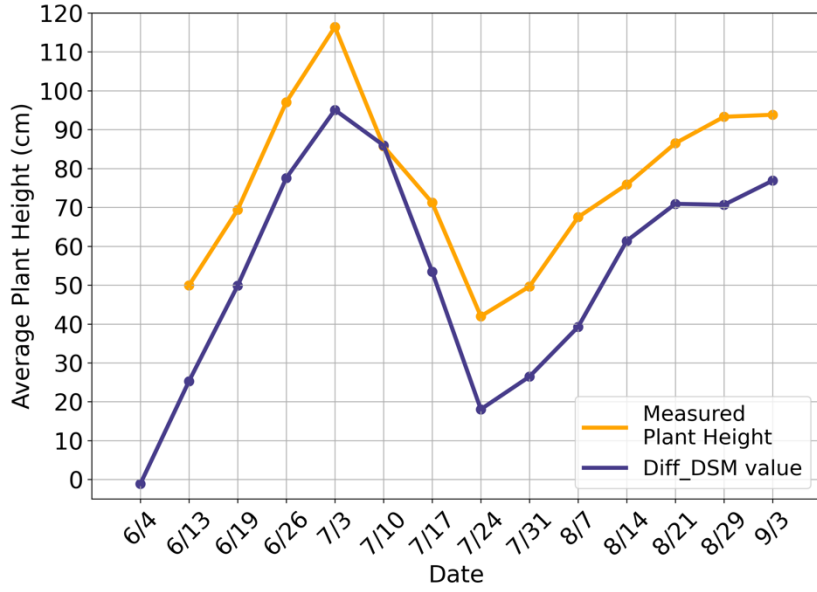
**Figure 3.5 (a) Time series of plant height of Potato**



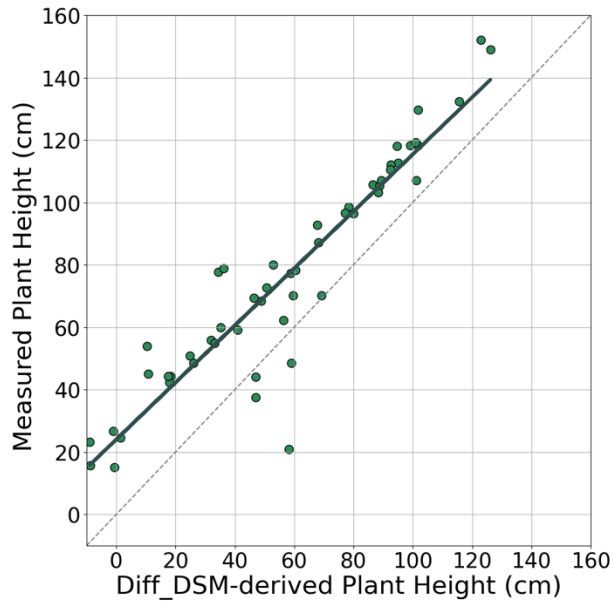
**Figure 3.5 (b) Relationship between the estimated plant height by DSM and measured plant height of Potato**

### 3.3.4 Accuracy of estimated plant height for Oat

**Figures 3.6 (a) and 3(b)** show changes in plant height over time in an oat field and the relationship between plant height estimated by differential DSM and measured plant height. In the oat field, a very strong correlation ( $R = 0.09$ ) was observed between the estimated plant height and the measured plant height during the entire survey period including the heading stage. However, the RMSE was relatively large at 13.15 cm. Oats are collectively called wheat together with grains such as wheat and barley, but unlike wheat and barley, the panicles do not stand upright on the culm, but consist of small panicles that sparsely droop downward. It does not exceed the size of the leaves (**Figure 3.4**). In addition, it has the largest spikelet (approximately 3 cm) in the Poaceae family, so even if the inflorescence exceeds the culm, it can be recognized in an aerial image. However, similar to the wheat, the upright culms are fasciated and the gap between leaves is relatively large, so the RMSE value is relatively large. From this, it was found that the DSM with a ground resolution of 10 cm is effective for estimating the plant height of gramineous cereals that cannot grow pampas.



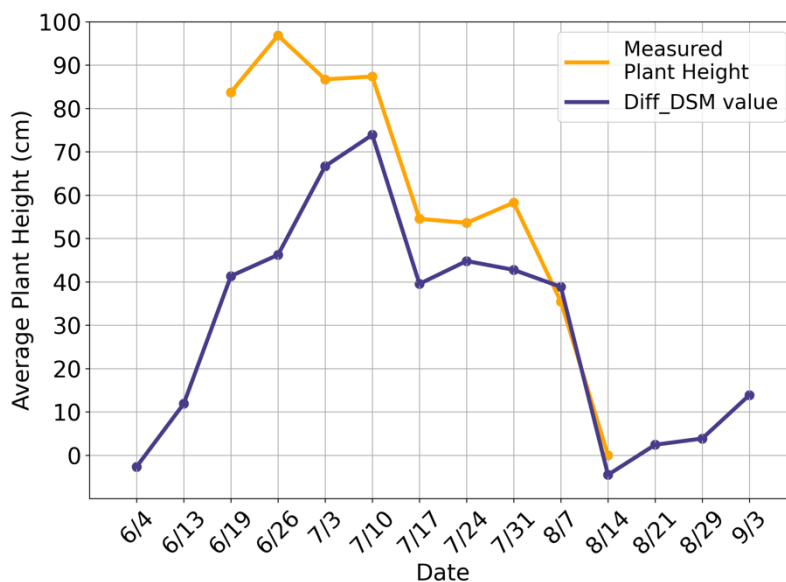
**Figure 3.6 (a) Time series of plant height of Oat**



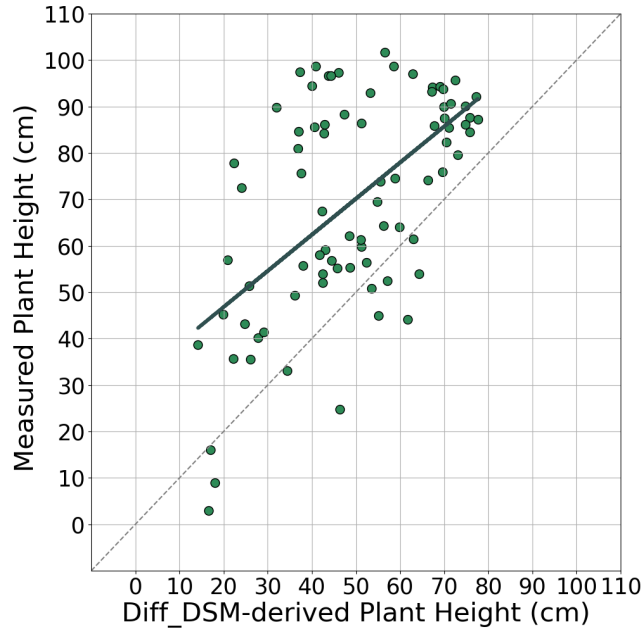
**Figure 3.6 (b) Relationship between the estimated plant height by DSM and measured plan height of Oat**

### 3.3.5 Accuracy of estimated plant height for Barley

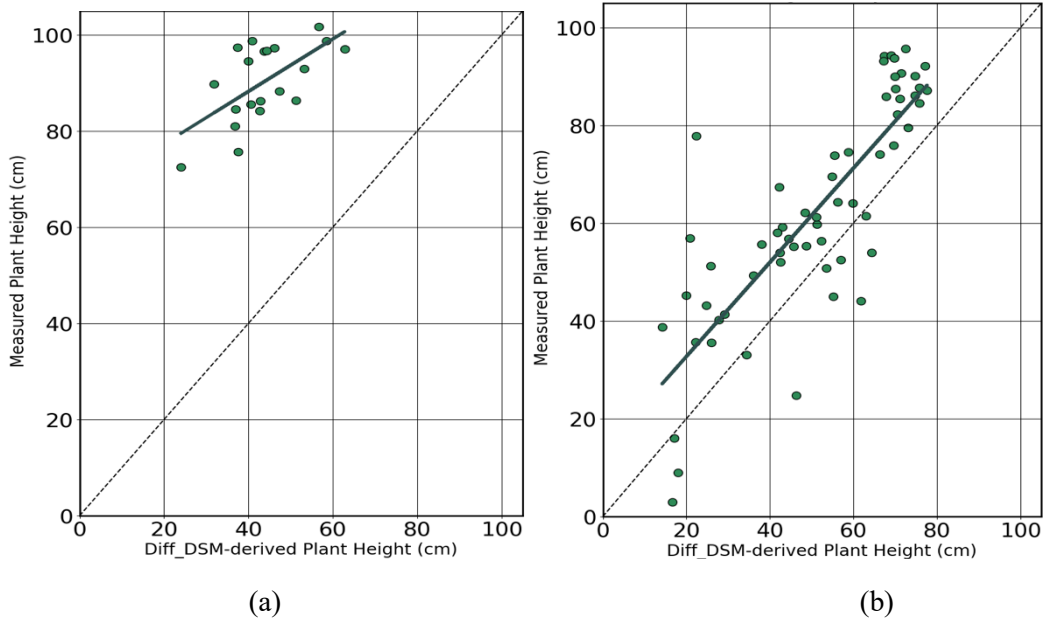
**Figure 3.7 (a)** and **(b)** show the time-series changes in the plant height of the barley field and the relationship between the estimated plant height and the measured plant height based on the difference DSM. It greatly exceeded the measured plant height. The reason for this is thought to be that the barley had emerged during this period. Like wheat, barley produces dense panicles on the culm length at the time of ear emergence, but the tip of the panicle is characterized by a long erect pampas grass, and the inflorescence is covered with countless pampas grass. Such pampas grass is thought to be the driving force behind the estimated plant height being lower than the measured plant height when the ground resolution of DSM is 10 cm. From July 3rd, the barley field suffered severe lodging due to heavy rain, and the lodging condition continued until harvest. Due to this phenomenon, the estimated plant height became closer to the measured plant height. **Figure 3.8 (a)** and **(b)** show the relationship between the estimated plant height before and after lodging and the measured plant height. From this result, it was found that the DSM with a ground resolution of 10 cm is not suitable for estimating the plant height of crops with pampas grass on the culm length such as barley.



**Figure 3.7 (a) Time series of plant height of Barley**



**Figure 3.7 (b) Relationship between the estimated plant height by DSM and measured plant height of Barley**



**Figure 3.8 Relationship between the estimated plant height by DSM and measured plant height of Barley during different growing period:  
 (a) From 2019/6/19 to 6/26; (b) From 2019/7/3 to 8/4**

### 3.3.6 Correction of estimated plant height by canopy cover

The Canopy Cover value and the dates of the UAV photographs by which the Canopy Cover was calculated are shown in Table 1. In the barley field, the Canopy Cover increased pronouncedly after the lodging from 88.9% (June 26th) to 97.1% (July 3rd), while in the Perilla field, the Canopy Cover increased gradually from 90.4% (July 31th) to 100.0% (September 3rd). The relationship between the measured PH and the estimated PH corrected by Canopy Cover is shown in **Figure 3.9**. In the barley field, the performance of the estimated PH after correction by Canopy Cover ( $R^2=0.57$ ,  $RMSE=20.9$  cm) was shown to be more accurate than before correction. In the Perilla field, the estimation accuracy was slightly increased ( $R^2=0.97$ ,  $RMSE=7.9$  cm) after it was corrected by Canopy Cover.

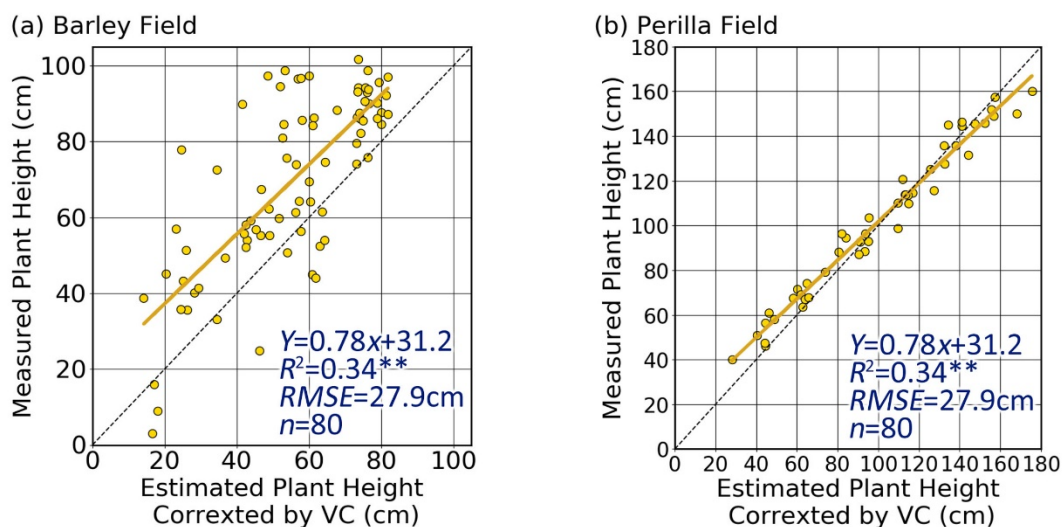
**Table 1 Canopy Cover during survey period**

(a) Barley Field

Date	June 19	June 26	July 3	July 10	July 17	July 24	July 31
CC	87.3%	88.9%	97.1%	98.8%	98.8%	99.2%	95.5%

(b) Perilla Field

Date	July 31	August 7	August 14	August 21	August 29	September 3
CC	87.3%	88.9%	97.1%	98.8%	98.8%	99.2%



**Figure 3.9 Relationship between measured and estimated PH corrected by Canopy Cover**

### **3.4 Conclusions of this chapter**

In this study, the accuracy of estimating PH based on DSM data generated from UAV photographs for three crops with different plant shapes were compared. Although the estimation accuracy for barley was low during the whole survey period, it increased after the elimination of the effect of the spikes. For both barley and oat plants, the estimated PH were lower than the measured PH, because the DSM provided the average height of all factors within one pixel. However, the estimated PH for perilla was more accurate than the other subjects and surpassed the measured PH late in the growth stage due to its luxuriant plant shape. Future study is expected to discuss and verify this difference of estimation characteristic between monocotyledons and dicotyledons. Furthermore, VC was proved to be helpful to increase the estimation accuracy of PH for both barley and perilla plant.

## Reference of this chapter

1. Tilly, N., Hoffmeister, D., Cao, Q., Huang, S., Lenz-Wiedemann, V., Miao, Y., & Bareth, G. (2014). Multitemporal crop surface models: accurate plant height measurement and biomass estimation with terrestrial laser scanning in paddy rice. *Journal of Applied Remote Sensing*, 8(1), 083671.
2. Ballesteros, R., Ortega, J. F., Hernandez, D., & Moreno, M. A. (2018). Onion biomass monitoring using UAV-based RGB imaging. *Precision agriculture*, 19, 840-857.
3. Lu, N., Zhou, J., Han, Z., Li, D., Cao, Q., Yao, X., ... & Cheng, T. (2019). Improved estimation of aboveground biomass in wheat from RGB imagery and point cloud data acquired with a low-cost unmanned aerial vehicle system. *Plant Methods*, 15(1), 17.
4. Zeng, Yong, and Rui Zhang. "Energy-efficient UAV communication with trajectory optimization." *IEEE Transactions on Wireless Communications* 16.6 (2017): 3747-3760.
5. Sun, X., Liu, L., Li, C., Yin, J., Zhao, J., & Si, W. (2019). Classification for remote sensing data with improved CNN-SVM method. *IEEE Access*, 7, 164507-164516.
6. Qi, Jiaguo, Yoshio Inoue, and Narumon Wiangwang. "Hyperspectral remote sensing in global change studies." *Fundamentals, Sensor Systems, Spectral Libraries, and Data Mining for Vegetation*. CRC Press, 2018. 3-26.
7. Bendig, J., Willkomm, M., Tilly, N., Gnyp, M. L., Bennertz, S., Qiang, C., ... & Bareth, G. (2013). Very high resolution crop surface models (CSMs) from UAV-based stereo images for rice growth monitoring in Northeast China. *Int. Arch. Photogramm. Remote Sens. Spat. Inf. Sci*, 40, 45-50.
8. Bendig, J., Bolten, A., Bennertz, S., Broscheit, J., Eichfuss, S., & Bareth, G. (2014). Estimating biomass of barley using crop surface models (CSMs) derived from UAV-based RGB imaging. *Remote sensing*, 6(11), 10395-10412.
9. Zarco-Tejada, Pablo J., et al. "Tree height quantification using very high resolution imagery acquired from an unmanned aerial vehicle (UAV) and automatic 3D photo-reconstruction methods." *European journal of agronomy* 55 (2014): 89-99.
10. Teng, L., Jianfeng, M., Pengbin, F., Yue, M., Xindi, M., Jiawei, Z., ... & Di, L. (2019, October). Lightweight security authentication mechanism towards UAV networks. In *2019 International Conference on Networking and Network Applications (NaNA)* (pp. 379-384). IEEE.



## **Chapter 4 Comparison of DSM and 3d Point Cloud by Small UAV Imagery on Estimating Plant Height and Biomass Volume**

### **4.1 Introduction**

Proper planting of biomass fuel plant has become one of the main challenges of carbon neutral. In recent years, attention has been paid to the use of pasture grass as biofuel. Gramineae grass has a vigorous regenerative power and can be cut multiple times a year. Some species can be continuously cultivated for more than five years [1]. Furthermore, pasture grasses can adapt to most kinds of ground surface environment and provide high yields where the edible crops can hardly grow, which avoids the competition between biofuel and food production.

At the site of grassland management, plant height and biomass production monitoring during the growing stage is one of the most important measurements. In the last decade, with the advancement in new platforms such as unmanned aerial vehicles (UAVs), methods based on remote sensing for biomass production estimation are gathering popularity. As a result of the fusion of UAV remote sensing and digital photogrammetry technology, a flexible and automatic approach of progressing aerial imagery has been developed, which is known as the structure from motion (SfM) technology. Based on the multiple overlapping images, characteristic feature points are detected of which the three-dimensional (3D) coordinated are reconstructed during the bundle adjustment progress afterwards. After the bundle adjustment, a detailed scene geometry made by a sparse point cloud is built and all pixels are used in this step to reconstruct finer scene details. Based on this sparse point cloud, the dense point cloud, orthomosaic and the digital surface model (DSM) are exported. As an intermediate production to construct the DSM, the characteristic of the dense point cloud is that it is not filtered, meaning that it contains all the outliers and noise point [2]. On the other hand, DSM is exported in a common image format such as \*.tif with a particular coordinate system, with the pixel size of more than one centimeter, meaning that one pixel represents the mean value of all 3D points inside it. Furthermore, filters such as noise filter and surface smoothing filter are applied to the DSM, which make the DSM unable to represent the detail of the small features on the ground precisely, such as the leaves of plants [3].

The difference between the DSMs of a planted field and the digital terrain model (DTM) has been referred to crop surface model (CSM) [4]. Ever since Bendig et al. firstly adopted SfM-MVS to derive plant height (PH) and above-ground biomass using CSMs in 2013, this method has become the most explored and verified approach to simulate the structure of crops all over the world. Most studies showed that the plant height estimated by CSMs tend to be lower than the plant height measured on the ground, because of the average and smooth surface of CSMs [5]. Based on this background, there is thought to be a possibility that point clouds can represent the plant height of crops more accurately than CSMs.

However, there is no study yet discussing the difference at the performance on estimating plant height and above-ground biomass volume of pasture grass. The objectives of this study are 1) to compare the estimation results of plant height and biomass volume

obtained by point clouds and CSMs respectively, and 2) discuss the characteristics of each of them on representing three-dimensional structure of the crop.

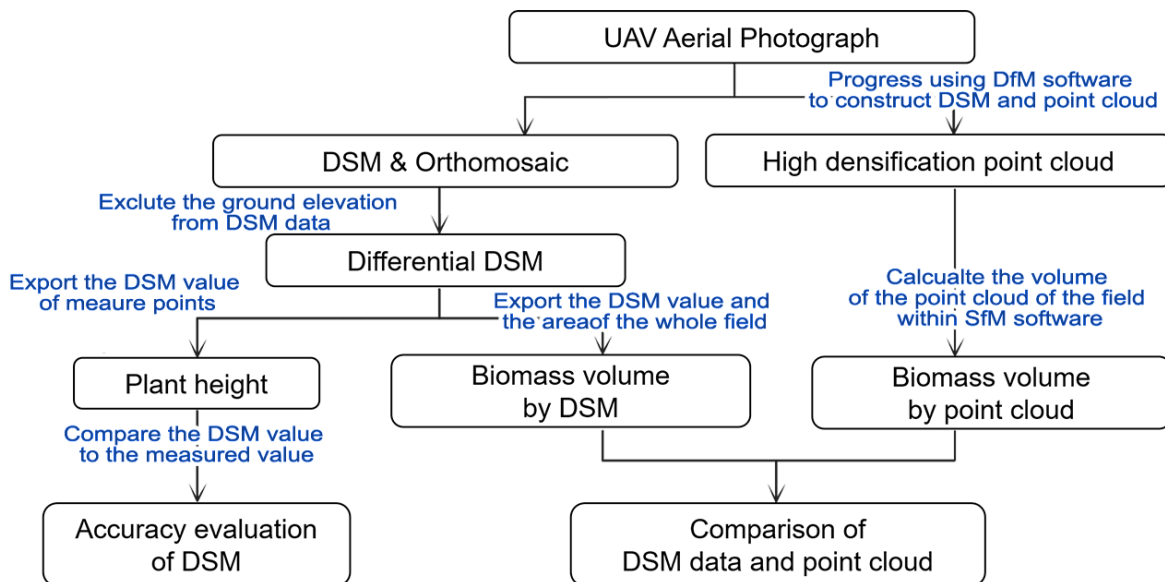
## 4.2 Methodology

### 4.2.1 Data collection

The study site was a grass field inside the experimental field of Obihiro University of Agriculture and Veterinary Medicine, Obihiro City, Hokkaido, Japan. The specie of the pasture grass was reed canary grass. The surveys by UAV were conducted weekly from 31st May to 3<sup>rd</sup> September 2019 (15 times in total), with Phantom 4 Pro (DJI). Before the UAV flights, seven ground control points (GCPs), of which position information was measured using RTK-GNSS (HiperV, TOPCON), were settled all over the experimental field. The flights were carried out automatically by Pix4D Capture (Pix4D). During each flight, the flying height was 50 m above ground. Both the top-overlap and the side-overlap rate were 80%. The ground sampling distance (GSD) of the raw aerial imagery was 1.32 cm. Ground surveys in order to obtain the plant height of the grass were conducted from 17<sup>th</sup> July to 3<sup>rd</sup> September (totally 8 times), on the same dates as the UAV surveys. During each time of the ground surveys, six measuring points were settled all around the grass field and marked with marking tapes which could be seen at the aerial imagery. Sampling of these six measure points was made during every time of the ground survey. A self-made plant height measure was used to obtain the optimal height value of the grasses. According to [5], “the  $PH_{CSM}$  represents the mean plant height of all pixels in a pixel. As a result, not only the top of the plant, for example the ears, is measured, but also the lower parts, like the leaves. Consequently, the detail of  $PH_{CSM}$  is higher than  $PH_M$ , because  $PH_{CSM}$  contains more than on pixel per plant and, the method of the  $PH_M$  reference measurements in the field should be discussed.” Based on this opinion, which is most reasonable, the method of method to measure plant height with tape measure or staff ruler, which has been used in many studies, can defiantly not obtain the obtain value standing for the plant height of a certain the field. In this research, a self-made plant height measure was used to obtain the reference plant height. A sliceable plastic plate (10 cm × 20 cm) was used to determine the proper height of the grass canopy. When measuring, the plate was sliced down from above, until every parts of its bottom was touched by the grass leaves. The leaves should be naturally curved instead of being forced bending when the plat has stopped. This method can not only help determine the optimal canopy position, but also help the observer to read the scale efficiently. The height of the grass is usually lower than one meter, meaning that the investigator has to squat down or gravel down to the ground in order to look at the canopy from a horizontal direction.

## 4.2.2 Data analysis

**Figure 4.1** shows the workflow of the data processing. The RGB imagery obtained by UAV was progressed using Pix4D mapper (ver 4.6.5, Pix4D) to construct the dense point clouds, orthomosaic, and DSMs, of which coordinate was corrected by GCP calibration. By identifying the measuring points at the orthomosaic, the coordinates of the measuring points were extracted using ArcGIS Pro (ver 2.4.1, Esri). After inputting the coordinates into the Pix4D mapper again, the location of the measuring points was marked at the dense point clouds. The plant height obtained from point clouds ( $PH_{PC}$ ) was then calculated by subtraction the altitude of the ground surface from the altitude of the grass surface. On the other hand, CSMs were made with ArcGIS Pro by subtraction of the DSM of the field without plants from the DSMs with plants. The plant height obtained from CSMs ( $PH_{CSM}$ ), which was in other words the CSM value of each measuring point, was then extracted using ArcGIS Pro. Then, both  $PH_{PC}$  and  $PH_{CSM}$  were compared to the measured value of plant height ( $PH_M$ ) to evaluate the accuracy of point clouds and CSMs to estimate the plant height of grasses. Finally, the above-ground biomass volume (BV) of the whole grass field instead of the particular measuring points was extracted from point clouds and CSMs ( $BV_{PC}$ ,  $BCANOPY COVER_{SM}$ ), respectively, and compared to each other to unravel the characteristics of point clouds and CSMs on estimating above-ground biomass volume of pasture grass. The calculation of  $BCANOPY COVER_{SM}$  used the geometry function of ArcGIS, and the calculation of  $BV_{PC}$  used the Volume Tool of Pix4D mapper.

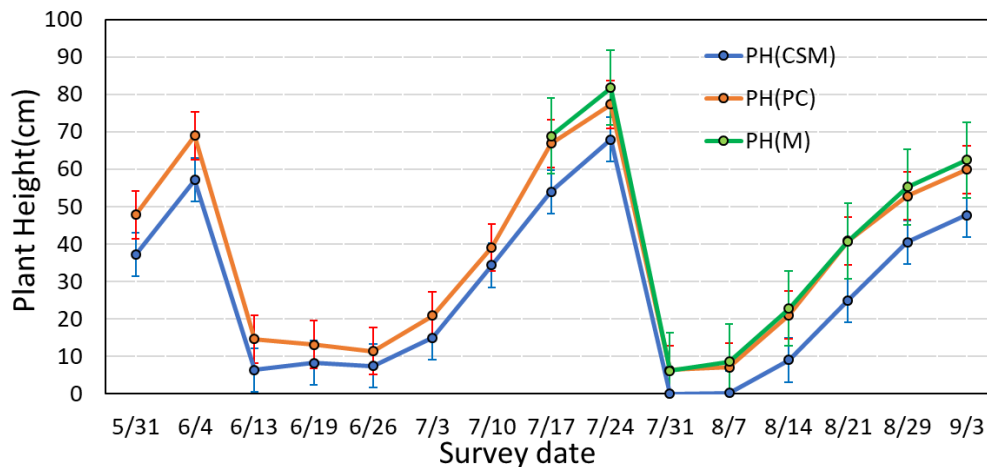


**Figure 4.1** Workflow of data analysis

## 4.3 Results

### 4.3.1 Time series of the plant height estimated by point clouds and DSMs

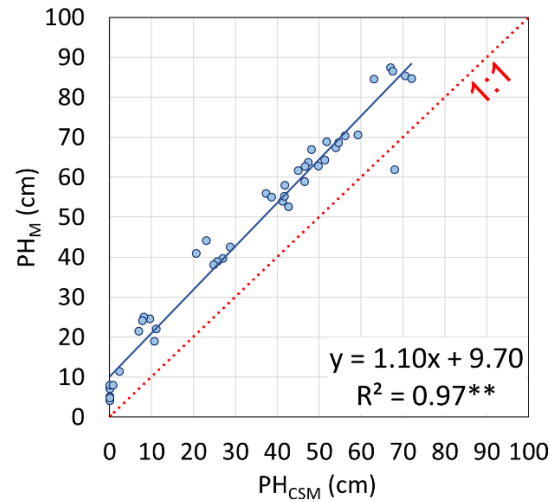
**Figure 4.2** shows the Time series of measured value of plant height ( $PH_M$ ), plant height obtained from point clouds ( $PH_{PC}$ ) and plant height obtained from crop surface model ( $PH_{CSM}$ ). From 17th July to 3<sup>rd</sup> September, all the three time series lines remained approximately parallel to each other. However, the line of  $PH_{CSM}$  stayed lower than the reference line all the time, while the  $PH_{PC}$  line was almost laying over the reference line. This indicated that both CSMs and point clouds could reflect the growth trend of grass, while there was a constant difference existing between the plant height estimated by CSMs and the reference value.



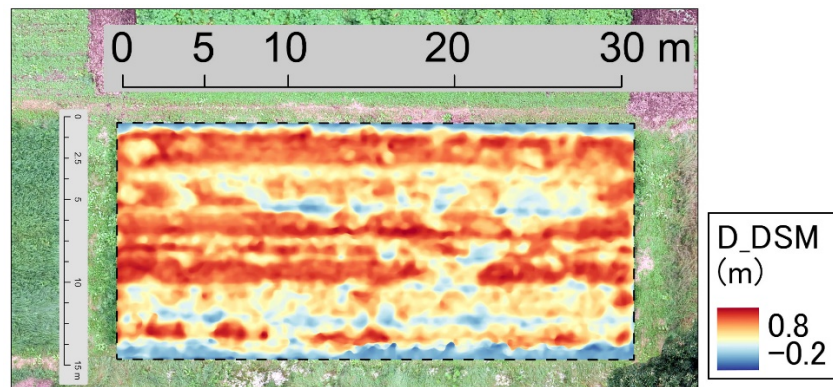
**Figure 4.2** Time series of  $PH_M$ ,  $PH_{PC}$  and  $PH_{CSM}$

### 4.3.2 Comparison of the accuracies of plant height estimated by DSM and 3D point cloud data

**Figure 4.3** shows the relationship between  $PH_M$  and the estimated plant height by CSMS ( $PH_{CSM}$ ). The number of samples was 48 (6 samples  $\times$  8 times of ground survey). The regression coefficient was close to 1, which suggests the regression line was nearly parallel to the 1:1 line. On the other hand, the intercept was approximately 10, suggesting there was a difference of about 10 cm between  $PH_M$  and  $PH_{CSM}$ , which stayed stable during the whole survey period since the regression coefficient was near to 1. The  $R^2$  and  $RMSE$  were 0.97\*\* and 14 cm, respectively, also showing that  $PH_{CSM}$  has the same changing trend, however a stable difference with  $PH_M$ . These showed that CSM can represent the changing trend of the plant height of pasture grasses, but has a relatively low accuracy on estimating the value of plant height. On the other hand, as shown at **Figure 4**, the CSM map could show the growth unevenness clearly by the estimated plant height within ArcGIS.

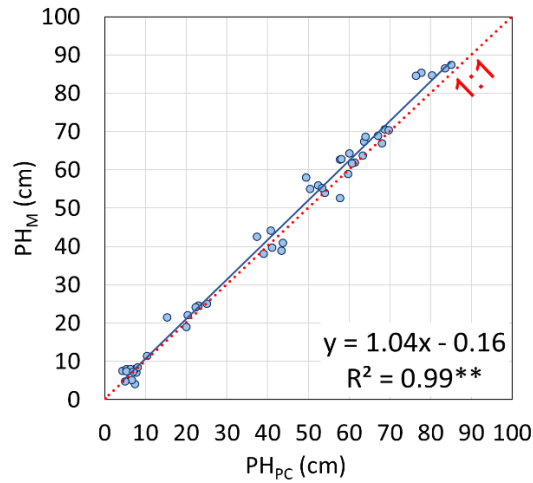


**Figure 4.3 Relationship between  $PH_M$  and  $PH_{CSM}$**



**Figure 4.4 CSM map for grass field (2019/7/24)**

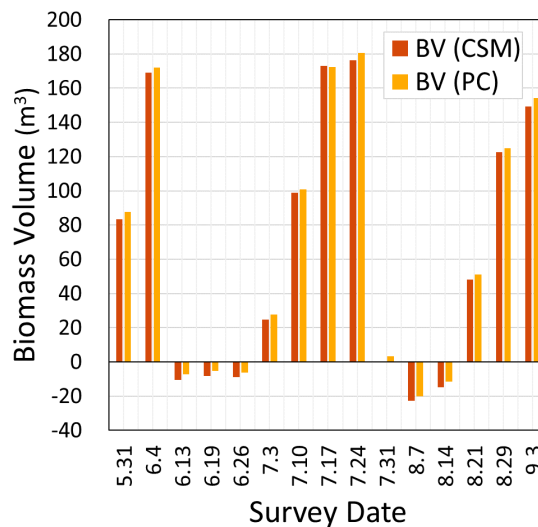
**Figure 4.5** shows the relationship between the measured value of plant height ( $PH_M$ ) and the estimated plant height by point clouds ( $PH_{PC}$ ). The regression coefficient and intercept of the regression equation were 1.04 and -0.16, respectively, making the regression line extremely close to the 1:1 line. The coefficient of determination ( $R^2$ ) and the RMSE were 0.99\*\* and 3 cm, respectively. This result showed that point clouds can estimate plant height of pasture grass with extremely high accuracy with little need for calibration.



**Figure 4.5 Relationship between PH<sub>M</sub> and PH<sub>PC</sub>**

#### 4.3.3 Comparison of biomass volume estimated by DSM and point cloud data

**Figure 4.6** shows the comparison of BV<sub>PC</sub> and BCANOPY COVER<sub>SM</sub> of the whole field during the whole survey period from 31<sup>th</sup> May to 3<sup>rd</sup> September. The BCANOPY COVER<sub>SM</sub> and BV<sub>PC</sub> of 13<sup>th</sup> June, 19<sup>th</sup> June, 26<sup>th</sup> June, 7<sup>th</sup> August, and 14<sup>th</sup> August showed minus value because the DSM used as the bare ground surface had included the remaining grass after the reaping. The result of t-test showed that there was no significant difference between BV<sub>PC</sub> and BCANOPY COVER<sub>SM</sub>. This result showed that despite point cloud can estimate plant height of pasture grass with higher accuracy than CSM, it gives the same value of above-ground biomass volume estimation with CSMs.



**Figure 4.6 Comparison of BV<sub>PC</sub> and BCANOPY COVER<sub>SM</sub>**

#### 4.4 Discussion

Despite the reference plant height was measured by an improved method and was as accurate as possible, there was still a 13 cm RMSE of the  $PH_{CSM}$  of the grassland. It is necessary to realize that there is a problem estimating when estimating plant height using CSMs, which is caused not by the human error or the environmental factors such as the wind, but by the characteristics of the DSM itself. There is a fact that should not be ignored that the airborne laser scanning or the aerial digital photogrammetry were aiming at generating DEMs standing for the basic topographic shape at the first place. The key point of DEM generation using aerial imagery was never about the bumpy terrain or the above-ground objects, but about the smooth terrain. This fact is so important, because it resulted in a critical characteristic of the dense matching algorithm such as SfM-MVS, which are the de-noising filter and the smooth filter. Both of these filters can improve the accuracy and quality when constructing terrain models or large-scaled buildings. However, the disadvantage of using these filters is that the small-scaled or low-heighted objects may be smoothed, for example, the leaf of crop plants. As long as DSM is still raster data, which represents the ground objects with certain-sized pixels, it has a limit on estimating plant height of crops, because there are spaces between the crop leaves. This is thought to be the inherent weakness of apply remote sensing photogrammetry to agriculture.

Compared with CSMs, point clouds showed much higher accuracy on estimating plant height of grass field. The reason of the high accuracy is considered to be because no smooth filter and pixel averaging algorithm has been conducted when constructing point clouds. While CSM shows the average height of all the objects of a certain area (for example, one pixel), point cloud shows the particular height of one certain object (for example, the leaf of grass). In other words, point cloud reflects a more detailed height distribution data of the grass field. Therefore, it is considered that point cloud is more qualified than CSM to estimate grass field plant height.

However, on the other hand, when estimating above-ground biomass volume, no significant difference was found between the results obtained by CSMs and point clouds. It is because when calculating the total value of the grass above-ground volume with point cloud, not only the dense points of the canopy that were included, but also the lower parts between the grass leaves, including the ground surface. As the result, point cloud yields the same value as CSM on grass above-ground biomass volume estimation. The spaces between the leaves, which has been found an error factor and should be excluded when estimating plant height, is no longer an error factor when estimating above-ground biomass volume and should be considered in order to increase the accuracy. This led to a conclusion that point cloud is more qualified on estimating plant height of grass than CSM, but has the same accuracy as CSM on estimating above-ground biomass volume.

There has been mainly two purpose for remote sensing at agriculture field, monitoring the current status of the crop land, and predicting the final yield of the crops before harvesting. Before UAV was popularized, the former purpose could not be fully achieved, because neither satellite imagery nor laser scanning was properly suit for the purpose. The ground resolution of satellite imagery, which is usually larger than one meter, is too large for a single crop land. The laser scanning conducted by ground survey is both time and labor consuming, making it almost not realistic for the whole crop field. This is exactly why UAV is so crucial on applying remote sensing to the real agriculture sites. It is more precise than satellite imagery, and more efficient than laser scanning, making it perfectly suit the purpose of current status monitoring of crop lands. For decades, remote sensing has found difficulties on benefiting the farmers directly. With UAV becoming a trustable platform of remote sensing, it is finally possible to help farmers make better management of their own crop land, by not only the traditional CSM data, but also the precise dense point cloud data.

#### **4.5 Conclusion of this chapter**

In this study, the abilities of dense point clouds and CSMs on estimating plant height and above-ground biomass volume for pasture grass have been validated and compared based on multiple-time surveys. Plant height was monitored by dense point cloud with very high accuracy (RMSE = 3.5 cm), while the plant height monitored by CSMs was consistently lower than the reference value. On the other hand, no significant difference exists between the above-ground biomass volume estimated by dense point cloud and CSMs. These results show that dense point cloud has an advantage on reflecting current status of crops, while has the same accuracy with CSMs on predicting above-ground biomass volume. When the purpose of the UAV survey is to monitor the precise status of the crops or identify the lodging area, point cloud is a better choice of data; while when the purpose is estimating the biomass volume of the whole field with little requirement of details, DSM data provides the estimated value with both accuracy and efficiency.



## Reference of this chapter

1. Nakagawa, H. 2009. "Characteristic of tropical grasses for biomass production and the breeding for biofuel feedstocks." *Japanese Journal of Grassland Science* 55 (3), 274-283.
2. Koppel, P. 2015. Agisoft PhotoScan: Point Cloud accuracy in close range configuration. Koppel Engineering, Retrieved from [https://www.google.com/url?sa=t&rct=j&q=&esrc=s&source=web&cd=&cad=rja&uact=8&ved=2ahUKEwj8rZmjMb5AhWTCd4KHbzdBj8QFnoECCMQAQ&url=https%3A%2F%2Fwww.agisoft.com%2Fpdf%2Farticles%2FPaul\\_Koppel\\_AgisoftPhotoScan\\_case\\_study\\_01.pdf&usg=AOvVaw1KS6bqVXJTbroDu1YCh2s5](https://www.google.com/url?sa=t&rct=j&q=&esrc=s&source=web&cd=&cad=rja&uact=8&ved=2ahUKEwj8rZmjMb5AhWTCd4KHbzdBj8QFnoECCMQAQ&url=https%3A%2F%2Fwww.agisoft.com%2Fpdf%2Farticles%2FPaul_Koppel_AgisoftPhotoScan_case_study_01.pdf&usg=AOvVaw1KS6bqVXJTbroDu1YCh2s5)
3. Cubero-Castan, M., Schneider-Zapp, K., Bellomo, M., Shi, D., Rehak, M. and Strecha, C. 2018. Assessment of the radiometric accuracy in a target less work flow using Pix4D software. In *2018 9th Workshop on Hyperspectral Image and Signal Processing: Evolution in Remote Sensing (WHISPERS)*. IEEE, 1-4.
4. Hoffmeister, D., Bolten, A., Curdt, C., Waldhoff, G., & Bareth, G. 2010. High-resolution crop surface models (CSM) and crop volume models (CVM) on field level by terrestrial laser scanning. In *Sixth International Symposium on Digital Earth: Models, Algorithms, and Virtual Reality* Vol. 7840, 90-95. SPIE.
5. Bendig, J., Bolten, A., Bennertz, S., Broscheit, J., Eichfuss, S. and Bareth, G. 2014. Estimating biomass of barley using crop surface models (CSMs) derived from UAV-based RGB imaging. *Remote sensing*, 6(11), 10395-10412.

## **Chapter 5 Relationship between NDVI and Canopy Cover Sensed by Small UAV under Different Ground Resolution**

### **5.1 Introduction**

Canopy cover (CC) is a relatively easily measured property that is a is indicator of crop growth, and an important parameter in crop simulation models, such as AquaCrop model. When simulating crop development, AquaCrop describes the development expansion of the CC using the percentage area of green canopy cover. According to the Food and Agriculture Organization (FAO), CC is defined as the ratio between the soil surface covered by the green canopy cover over the ground surface. CC value ranges from 0, when there is a bare soil, to 1, where the ground is fully covered by the vegetation canopy. The maximum value of CC is decided by the crop characteristic. By means of a logistic type equation, AquaCrop describes the development of the canopy between generation and the moment maximum CC is reached. And then, at the end of the season when the senescence starts, the CC value declines [1]. Accurate and efficient estimation of CC would allow improved scheduling and allocation of irrigation water [2].

On the other hand, during the last three decades, Vegetation indices (VIs) have been extensively used for tracing and monitoring vegetation conditions such as health, growth levels and water or nutrients stress [3]. Previous studies have shown that various spectral calculated from visible and near- infrared reflectance data, are linearly related to the value of CC [4]. Healthy canopies of green vegetation have a very distinct interaction with certain portions of the electromagnetic spectrum. In the visible region, chlorophyll causes strong absorption of energy, primarily for use in photosynthesis. This absorption peaks in the red and blue region s of the visible spectrum, while the green region is reflected by chlorophyll, thus leading to the green color of most leaves. This strong contrast between the reflectance of red and near infrared regions of the electromagnet spectrum has been used to develop the Normalized Difference Vegetation Index (NDVI), a VI that has been widely used in the agricultural remote sensing field [3]. High resolution satellite data obtained from multispectral satellite sensors such as NOAA AVHRR, Terra MODIS, Landsat TM and all others that acquire data in both the visible and the near infrared regions have been used to generate Vis such as NDVI, to make better crop management, monitor the growing stress, and estimate the yield. Furthermore, during the last 10 years, the research methodology and data analysis techniques from traditional remote sensing has been used to process aerial images that has much higher spatial and temporal resolutions taken by Unmanned Aerial Vehicles (UAVs). This rapid development of remote sensing and precision agriculture provide aerial imagery with various resolution.

However, because remote sensing data may show different values even in the same position of the same species of vegetation, only a few studies have estimated CC with UAV-

obtained NDVI and show that UAV-based NDVI has the same linear regression relationship with CC as satellite-based NDVI. To explore the interchangeability of UAV-based NDVI and satellite-sensed NDVI on monitoring CC, this study discussed the possibility of CC estimation using remote sensed NDVI data under various spatial resolution of a peanut experimental field in Hokkaido, Japan.

## 5.2 Methodology

### 5.2.1 Data collection

This study was conducted in the experimental field of Obihiro University of Agriculture and Veterinary Medicine, located in Obihiro City, Hokkaido, Japan (143.1709-143.1747°N, 42.8698-42.8671°E, 60.6-99.8m altitude). The experimental field has a total area of 3.2 hectares (200×160m), which was separated to multiple sectors planted with various experimental crops. The peanuts sector inside the experimental field was selected as the study site to compare NDVI and CC. The peanuts usually have relatively spread forms of about 30-50 cm high with long branches that grow close to the ground. This morphological characteristic makes peanut a good objective to study the relationship between NDVI and CC, because NDVI tends to perform poor correlation to CC because of the variation of Leaf Area Index (LAI) when the vegetation cover area is the same, and this kind of variation of LAI is relatively unapparent in peanuts. The area of the peanut field is 1600 m<sup>2</sup> (40×40m), with the plant density of 7.7 plant/m<sup>2</sup>. The soil surface of the plant area was covered by white mulch films, because insolation during the early stage of growth is necessary to insure the basic vegetation growth of peanuts in low temperature region such as Hokkaido, and there was risk of chilling injury during the autumn of Hokkaido.

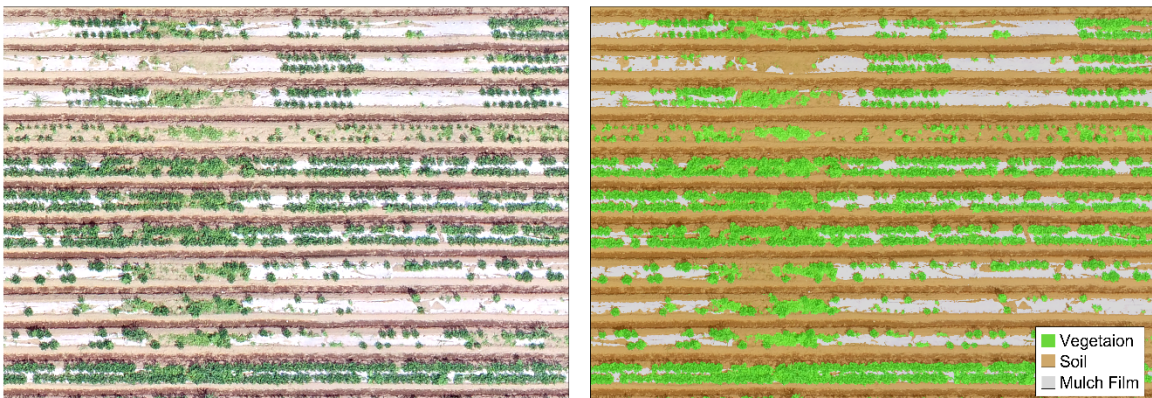
The RGB imagery of the experimental field was taken by Phantom 4 Pro (DJI) in 31th July, 2019, and the reflectance imagery was taken by a portable multispectral camera Sequoia (Parrot), which was installed on Inspire 1(DJI) at 1<sup>st</sup> August, 2019. The flight data is shown at **Table 5.1**.

**Table 5.1 Flight parameters**

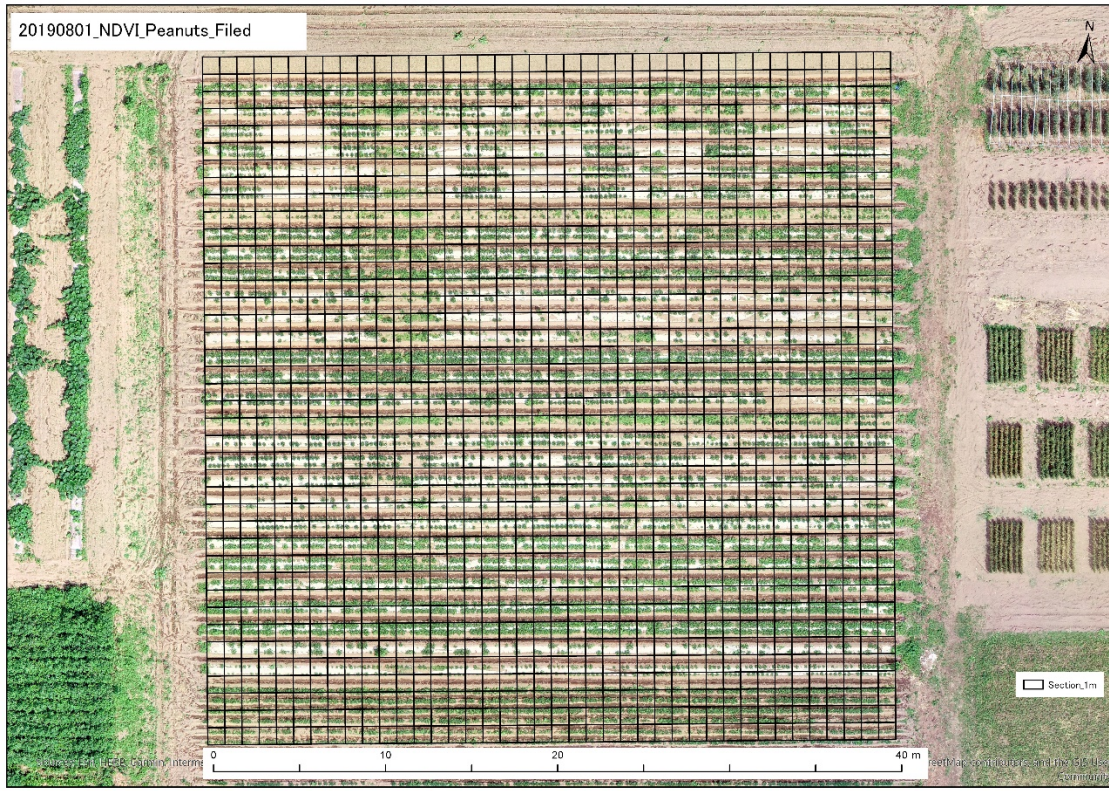
Equipment	Date	Height	Speed	Overlap-top	Overlap-side	Resolution
Phantom 4 Pro	7/31	50 m	4.8 m/s	80%	80%	1.3 cm/pixel
Inspire 1 & Sequoia	8/1	40 m	3.0 m/s	80%	80%	5.9 cm/pixel

### 5.2.2 Data analysis

After obtaining aerial imagery, an RGB orthomosaic image and a reflectance map of the experimental field were generated with the Structure from Motion (SfM) software, Pix4D Mapper (ver4.6.4, Pix4D). The RGB orthomosaic image was used to separate the vegetation, soil and mulch films in a Geographic Information System (GIS) software, ArcGIS Pro (ver 2.3.0, Esri) with a supervised image classification tool. The result of classification is shown at **Figure 5.2**. Basing on the classified raster, the CC value of the peanuts field was calculated using Eq.1, where “Vegetation”, “Soil” and “Mulch film” mean the number of pixels covered by green vegetation canopy, soil and mulch films, respectively. To obtain the CC and NDVI values under different ground resolutions, we divided the peanut field to squared grids with the side length of 0.5 m, 1.0 m, 2.5 m, 5.0 m, and 10 m. As an example, the 1.0 m grids are shown at **Figure 5.3**. Basing on the georeferenced reflectance map, the NDVI values of the peanuts field was calculated by Equation 2, where “NIR” and “Red” mean the reflectance volume of the near-infrared region and the red region. The relationship between NDVI and CC values of each size of grids was determined using a least-squares fitting algorithm with python (ver. 3.7). An Analysis of Covariance (ANCOVA) was carried out to testify if there is significant difference between the relationships between NDVI and CC under different ground resolutions. Finally, the accuracy of the regression equation was verified using RMSE.



**Figure 5.2 Classification result**  
(Left: RGB orthomosaic image; Right: Classified raster)



**Figure 5.3 Example of squared grid dividing the peanuts field (Grid size: 1.0 m)**

$$CC = \frac{\textit{Vegetation}}{\textit{Vegetaion} + \textit{Soil} + \textit{Mulch film}} \quad (1)$$

Where “Vegetation”, “Soil” and “Mulch film” mean the number of pixels covered by green vegetation canopy, soil and mulch films, respectively.

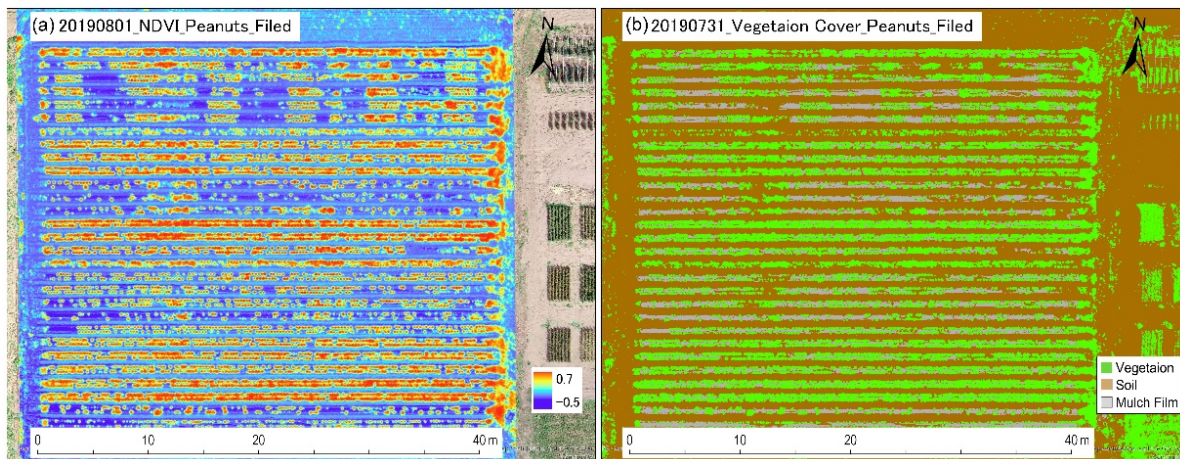
$$NDVI = \frac{NIR - Red}{NIR + Red} \quad (2)$$

Where “NIR” and “Red” mean the reflectance volume of the near-infrared region and the red region.

## 5.3 Results

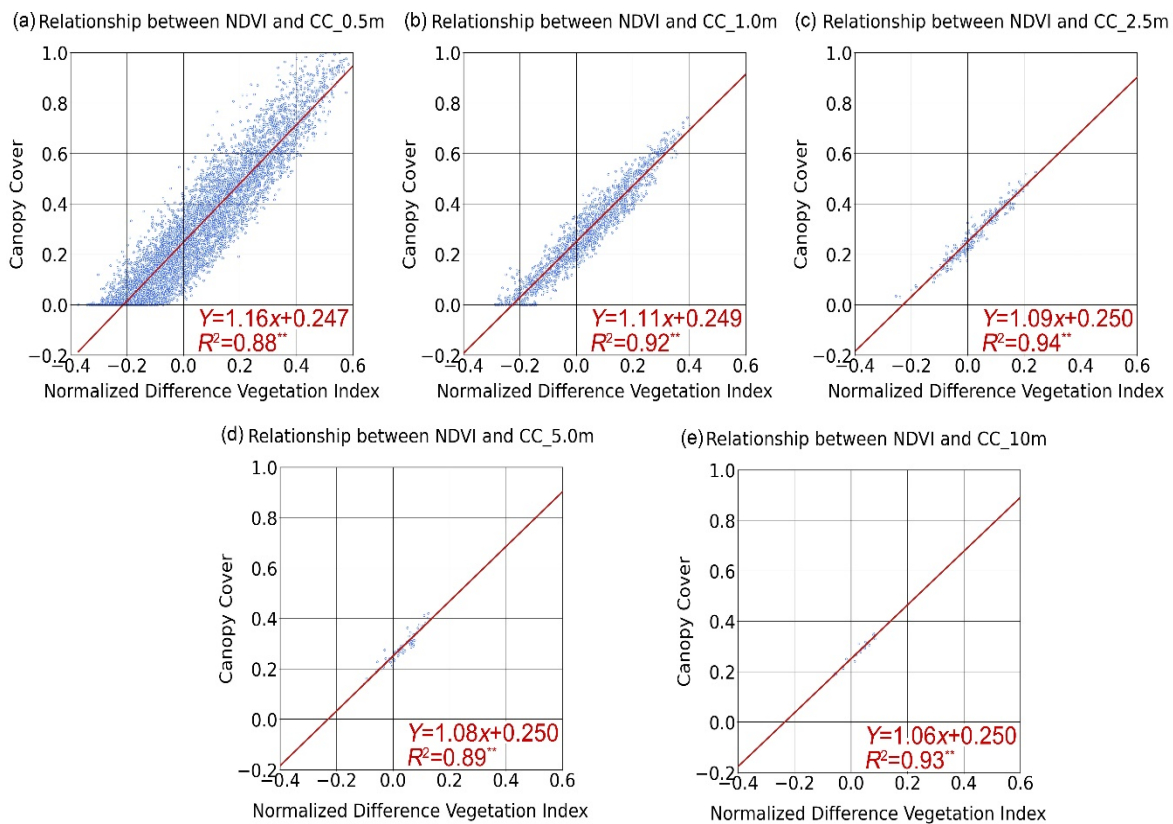
### 5.3.1 Relationship between NDVI and canopy cover under different ground resolution

**Figure 5.4 a, b** shows the spatial distribution of NDVI and vegetation cover under the original resolution of the peanuts field. NDVI tended to be high in the area covered by vegetation and low at the area covered by soil or mulch films. This is because the surface of vegetation has a lower reflectance rate in the red region and a higher reflectance in the near-infrared region, while the soil and the plastic mulch films have similar reflectance in both regions. Besides, the mulch film has a lower NDVI than soil, because the PCANOPY COVER material has a relatively higher reflectance of red, and at the meantime, a lower reflectance of near-infrared than soil [5]. The spatial distribution of NDVI of the other grid sizes (0.5 m, 1.0 m, 2.5 m, 5.0 m, and 10 m) showed the same trend. The NDVI value varied from -0.47 to 0.68 under the original resolution, from -0.37 to 0.61 under 0.5 m grid size, from -0.29 to 0.40 under 1.0, grid size, from -0.25 to 0.24 under 2.5 m grid size, from -0.10 to 0.13 under 5.0 m grid size, and from -0.05 to 0.08 under 10 m grid size. Unlike the crops or forests with the vertical growth pattern, the maximum NDVI value of peanuts was less than 0.7. This is because peanuts have a low-height, wide-expanding and horizontal-trained canopies which cause relatively low LAI within the canopies. The CC values varied from 0.00 to 1.00 under the original resolution, from 0.00 to 1.00 under 0.5 m grid size, from 0.00 to 0.74 under 1.0m grid size, from 0.03 to 0.53 under 2.5 m grid size, from 0.14 to 0.42 under 5.0 m grid size, and from 0.19 to 0.35 under 10 m grid size. The range of both NDVI and CC values decreased with the increase of grid sizes.



**Figure 5.4 Spatial distribution of NDVI (a) and vegetation cover (b)**

**Figure 5.5 a, b, c, d, e** shows the correlation between NDVI and CC under each grid size. NDVI was strongly correlated with CC under the resolution of 0.5 m, 1.0 m, 2.5 m, 5.0 m, and 10 m ( $R^2=0.88^{**}$ ,  $0.92^{**}$ ,  $0.94^{**}$ ,  $0.89^{**}$ , and  $0.93^{**}$ , respectively). The shape of the linear regression line ( $y=ax+b$ ) of NDVI and CC closely resembled to each other, with the slopes ( $a$ ) of 1.16, 1.11, 1.09, 1.08, and 1.06, respectively, and the intercepts ( $b$ ) of 0.25, 0.25, 0.25, 0.25, and 0.25, respectively. The intercept values indicate that a grid with 25 percent of it covered by peanuts canopies has an approximately NDVI value of 0. The slope values slightly decreased with the increasing of grid size, resulting the NDVI values of the grids without any vegetation cover varies from 0.5 m to 10 m (-0.21, -0.22, -0.23, -0.23, and -0.24, respectively). This is thought to be caused by the offset effect of two kinds of abnormal value of NDVI, one kind of the abnormal value happens in the grids with relatively low CC value but high NDVI values, due to the high LAI: the other kind of abnormal value is the grid with a high percentage of mulch films, which causes a lower NDVI value than the normal soil ground surface.



**Figure 5.5 Relationship between NDVI and CC**

### 5.3.2 Accuracy of predicted canopy cover by NDVI

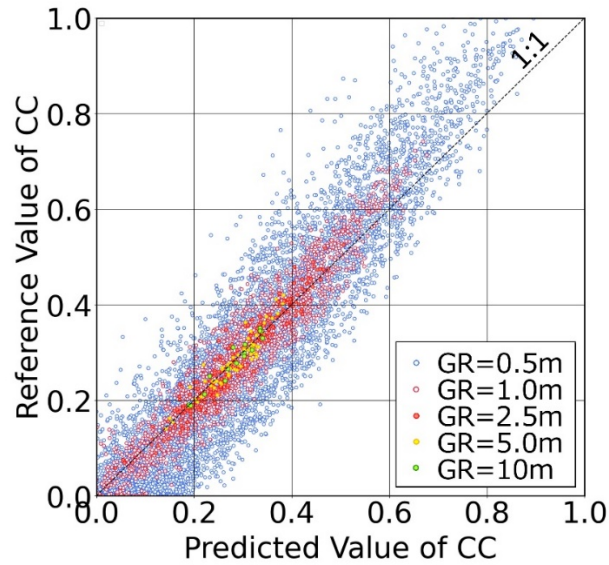
To testify the significance of the differences between each regression equation, an ANCOVA was conducted with an Excel data analysis add-on, XLSTAT (ver 2020.5.1, Addinsoft), where CC as the dependent variable, while NDVI and ground resolution as the explanatory variables. The result is shown at **Table 5.2**. The p value of all kinds of grid sizes was near to 1.000, indicating that the grid sizes have no significant effect on the relationship between NDVI and CC.

**Table 5.2 Model parameters of ANCOVA**

Factor	Regression coefficient	Standard deviation	<i>t</i>	<i>Pr &gt;  t </i>
Intercept	0.248	1.981	12.507	< <b>0.0001</b>
NDVI	1.16	0.469	246.767	< <b>0.0001</b>
Ground Resolution 0.5m	-0.003	1.983	-0.001	0.999
Ground Resolution 1m	-0.003	1.991	-0.002	0.999
Ground Resolution 3m	0.043	2.074	0.021	0.983
Ground Resolution 5m	-0.006	2.218	-0.003	0.998
Ground Resolution 10m	0.000	0.000		

Therefore, despite the slight difference between the regression equations of the five kinds of grid sizes, it is considered that the NDVI value of peanuts remains the same relationship with CC under different ground resolution. Since the offset effect of two abnormal values of NDVI was most remarkable at the 10 m grids, the equation derived from the data of 10m grid size was used to predict CC using NDVI. The relationship between the predicted CC value and the reference CC value was shown at **Figure 5.6**. The RMSE of CC estimation of each grid size from 0.50 m to 10 m was 0.081, 0.089, 0.048, 0.025, 0.020, 0.014, respectively.





**Figure 5.6 Relationship between the predicted CC value and the reference CC value**

#### **5.4 Discussion**

#### **5.5 Conclusion of this chapter**

Herein, we analyzed the relationships between NDVI and CC values of peanuts in the experimental field using UAV-sensed data under five kinds of ground resolutions. As the result, the NDVI showed highly correlated linear relationship with CC under each ground resolution. Slight differences of slopes and intercepts was found between the regression equations because two kinds of abnormal values of NDVI caused by high LAI and plastic material on the ground surface tend to cancel each other out in the larger grids. This kind of differences was found not significant due to an ANCOVA. The regression equation of 10 m grid size performed a moderate estimation accuracy of CC with the RMSE less than 0.01. This result demonstrated the possibility of using UAV multispectral imagery for CC monitoring with the same regression equations as satellite multispectral imagery.

### Reference of this chapter

1. Steduto, P., Hsiao, T.C., Raes, D. and Fereres, E., 2009. AquaCrop—The FAO crop model to simulate yield response to water: I. Concepts and underlying principles. *Agronomy Journal*, 101(3), pp.426-437.
2. Zhao, D., Huang, L., Li, J. and Qi, J., 2007. A comparative analysis of broadband and narrowband derived vegetation indices in predicting LAI and CCD of a cotton canopy. *ISPRS Journal of Photogrammetry and Remote Sensing*, 62(1), pp.25-33.
3. Bausch, W.C., 1995. Remote sensing of crop coefficients for improving the irrigation scheduling of corn.
4. Purevdorj, T.S., Tateishi, R., Ishiyama, T. and Honda, Y., 1998. Relationships between percent vegetation cover and vegetation indices. *International journal of remote sensing*, 19(18), pp.3519-3535.
5. Corradini, F., Bartholomeus, H., Lwanga, E.H., Gertsen, H. and Geissen, V., 2019. Predicting soil microplastic concentration using vis-NIR spectroscopy. *Science of the Total Environment*, 650, pp.922-932.

## **Chapter 6 Assessment of Three Automated Identification Methods for Ground Objects Based on UAV Imagery**

### **6.1 Introduction**

Despite recent advances and development in earth observing satellites, temporal resolution and cloud cover are some of the obstacles present for many quantitative remote sensing applications such as monitoring and detecting dynamics of environmental systems. Since the 2010s, unmanned aerial vehicle (UAV) has been popular for various purposes such as disaster relief, civil engineering surveys, pesticide spraying, and infrastructure inspections [1]. Compared to earth observation satellites such as Landsat, Terr, and SPOT, UAVs have advantages such as high mobility, high resolution, and low altitude flight (unaffected by clouds), which enable them to achieve highly accurate and precise observation of the ground objects.

Ground object identification using UAV imagery is helpful for an improved environmental and resource management system. For example, the occurrence of waste items all over the village, farming land, and natural parks have resulted in garbage management becoming a serious local environmental issue. Additionally, plastic pollution due to agricultural activities is an important source of pollution as they are difficult to quantify [2]. Furthermore, uncontrolled open dumping and burning pollutes water and soil, affects plants, increases vectors of disease, emits odors and green-house gasses into the atmosphere, and poses serious health risks to people working at open dumping sites [3]-[4]. Micro-plastics, formed when waste plastics are fragmented by photochemical, mechanical, and biological processes, contaminate aquatic ecosystems through passive or active ingestion by a wide range of organisms [5]. Environmental degradation, because of poor waste management, decreases the quality and quantity of forest, fisheries, and tourism resources. Such degradation has negative impacts on local industries, which in turn does indirectly affect people's well-being [6]-[9]. To sustainably mitigate and monitor drivers of environmental degradation, including ground objects such as agricultural wastes, vegetation, soil, weak vegetation, plastic sheets and metals, requires transdisciplinary collaboration in identification and monitoring amongst societal stakeholders and researchers.

Vegetation canopy cover monitoring is another topic that can be benefited from precise ground object identification, providing important information for forestry management and ecosystem service survey. Canopy cover (CC) is an easily measured characteristic that is an indicator of crop growth and an important parameter in crop simulation models, such as the Aqua Crop model [10]. Accurate and efficient CC estimation would allow improved scheduling and allocation of irrigation water [11]. Furthermore, identifying dead or weakened plants can help farmers to make better field management decisions. Therefore, identifying crop cover and weakened vegetation precisely and efficiently using UAV

imagery is thought to be helpful to rural environmental management, agriculture development, and integrated resource management. Most previous studies have only applied the normalized difference vegetation index (NDVI) threshold method for land cover classification and have not assessed the classification accuracy.

Ground object classification has been studied worldwide and can be achieved through different approaches. Vegetation indices have been extensively used to trace and monitor vegetation conditions such as health, growth levels, and water or nutrient stress [12]. Previous studies have shown that various spectral calculations based on visible and near-infrared reflectance data can reflect the growth status of vegetation [13]. In the last decade, research methodology and data analysis techniques from traditional remote sensing have been used to process aerial images obtained using UAVs that have high spatial and temporal resolutions, which allows precise NDVI data of the ground surface. Not only can the health condition of plants be monitored using NDVI, but discovery of the weakened vegetation, soil, and plastic and metal items is also possible, which have significantly different reflectance rates in the band ranges of red and near-infrared light [14]. Furthermore, PCANOPY COVER and metal materials have lower NDVIs than that of soil because of a relatively higher reflectance in the red range and a lower reflectance of near-infrared range than soil [15]. Therefore, the NDVI threshold method has been used as one of the standards to classify the land cover. Putr et al. (2015) successfully detected forest cover over multiple years in a national forest park using Landsat images with the NDVI threshold method [16]. Singh et al. (2020) assessed changes in land cover in a rural area with Landsat images using the NDVI threshold, and precisely detected the decrease in the densely vegetated area [17]. Hashim et al. (2019) performed urban vegetation classification using the NDVI threshold method based on very high-resolution Pleiades satellite image, and achieved a 70% overall accuracy [18]. El-Gammal et al. (2014) classified vegetation, non-vegetation, and water bodies in a rural area with Landsat images using the NDVI threshold method and achieved an extremely high overall accuracy of 96% [19]. This research shows that the NDVI threshold method is a practical classifier for land use classification.

Other methods for land cover classification include machine learning approaches, which classify the image depending on appropriate training samples. The machine learning algorithm allows image diagnosis to be conducted in an automatic and efficient manner. One of the most common methods of machine learning classification based on red, green, and blue-colored (RGB) images, such as the orthomosaic constructed from aerial images, is to classify the pixels depending on their RGB values according to the training samples. Hassan et al. (2011) generated land use/land cover maps with UAV-obtained RGB images using the supervised classification algorithm (maximum likelihood) and achieved a 90% overall classification accuracy [20]. Hamylton et al. (2020) compared the classification results with UAV GCB images using the pixel classification, visual interpretation, and machine learning approaches, and the machine learning method showed the highest overall accuracy of 85%

[21]. Shin et al. (2019) conducted classification of forest burn severity with UAV-obtained multispectral imagery using the maximum likelihood and threshold methods and achieved overall accuracies of 89% and 71%, respectively [22]. These results showed that the pixel-based machine learning method could achieve very high accuracy at land cover classification.

Differing from traditional pixel-based classification methods, the object-based image analysis (OBIA) method first separates the image into segments which are small polygons constructed of several neighboring and similar-valued pixels [23]. Then, with appropriate training samples, the classification is performed by dividing the segments into different classes according to their shape, size, and spectral content [24]. Compared to traditional pixel-based classification methods, OBIA is thought to be accurate for hydrologic modeling and vegetation detection owing to its ability to detect the health status as well as the factors influencing the biological habitats in a rapid, accurate, and cost-effective manner [25]. The OBIA is one of the most popular classifiers for land cover classification and has been applied and verified worldwide. However, no study has yet compared the classification accuracy of methods using the NDVI threshold, RGB image-based machine learning, and OBIA in rural areas. Natesan et al. (2018) performed land use classification using UAV-obtained multispectral images, and achieved overall accuracies of 78% and 50% for water bodies and mixed-colored classification classes, respectively [26]. Ahmed et al. (2017) compared different UAV camera data and platform performance for classifying forest, shrub, and herbaceous layers; bare soil; and built-up areas using the OBIA method and achieved overall accuracies of 90% and 80% with the multispectral camera and RGB sensor, respectively [27]. Sarronet et al. (2018) proposed a method to map individual mango tree production using the geographic object-based image analysis (GEOBIA) and obtained an RMSE% accuracy ranging from 20% to 29% [28]. Brovkina et al. (2019) performed forest stand classification with UAV-based NDVI and point dense clouds using the OBIA method and achieved a Kappa coefficient accuracy of 0.74 [29]. Comparison of classification performance between UAV and satellite multispectral image aerial data using the OBIA method by Yang et al. (2019) yielded Kappa coefficients of 0.713 and 0.538, respectively [30]. Ventura et al. (2018) performed mapping and classification of marine habitats with UAV-obtained RGB images using the OBIA method and achieved an overall accuracy of >80% in different study sites [25].

The automated identification methods have been applicable at agricultural field for better field monitoring and managements. Lanthier et al. (2008) conducted a comparative study between supervised pixel-oriented and the OBIA classifications in a precision agriculture context using hyperspectral images to identify three different crop species (corn, peas and beans), and found out that the OBIA method achieved better performance with the Kappa of 0.8268 [31]. Lebourgeois et al. (2017) analyzed and optimized the performance of a combined Random Forest classifier / OBIA approach and applied it to multisource satellite data to produce land use maps of a smallholder agricultural zone at five different

nomenclature levels of the crops, and achieved an overall accuracy of 91.7% and 64.4% for the cropland and crop subclass levels respectively [32]. Zheng et al. (2019) presented the crop vision dataset for deep-learning-based classification and detection method for over 30 categories of crops and achieved the overall accuracy of over 99% [33]. However, these studies were only focused on vegetation monitoring and classification, instead of the overall environment including the non-vegetation objects which also have influence on better field management.

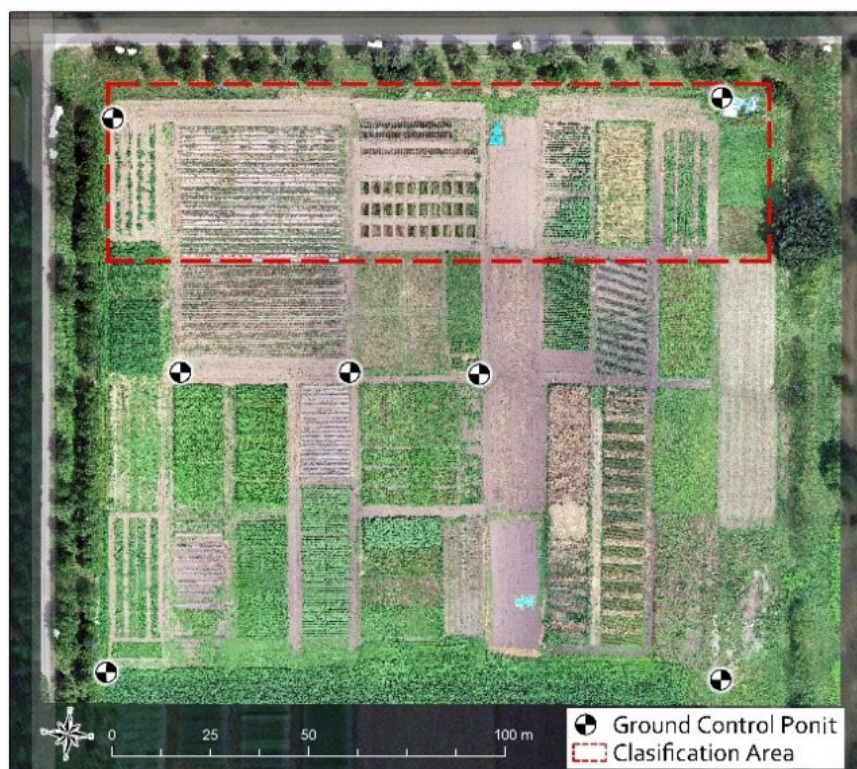
Unlike, satellite remote sensing methods, UAV surveys can identify accurately with high resolution and are also suited for small scale research applications. Applicability of these methods could provide societal stakeholders and researchers as a transdisciplinary approach in ground object identification, monitoring and decision-making abilities contributing to sustainable community development. However, for this approach to be used by stakeholders involved in integrated resource management, the following should be made clear (1) What are the characteristics of the three methods in terms of the accuracy of identification of the ground object? (2) What are the advantages and disadvantages of the three methods according to different ground object? (3) what are the recommendations for the choice of different methods toward integrated resource management? Therefore, this study aimed at performing ground matter identification with three different methods (NDVI threshold, RGB image-based machine learning, and Object-based image analysis (OBIA) method), comparing the total overall accuracy, and discussing the characteristics and optimal classification for each method.

## 6.2 Methodology

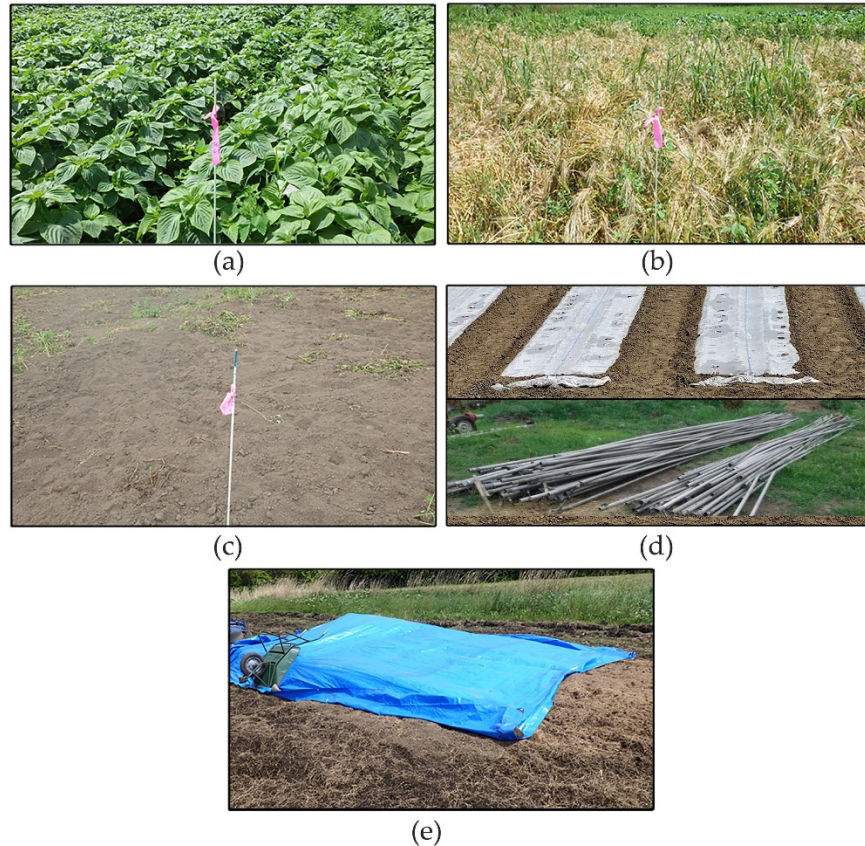
### 6.2.1 Study site

The aerial surveys were conducted within the experimental field (total area: 3.2 ha) of Obihiro University of Agriculture and Veterinary Medicine located at 42.8688°N, 143.1725°E, with an altitude of 75 m. The area used for classification verification is shown surrounded by the red dotted line in **Figure 6.1**. The ground objects at the study site were vegetation, dead/weakened vegetation, soil, plastic multi-sheet, plastic blue-sheet, and metal pipes (**Figure 6.2**). The vegetation included crops such as wheat, pasture grass, pumpkin, and peanut. The dead/weakened vegetation in this study site was barley which was near the harvest stage. If the methods discussed in this study could identify the weakened vegetation accurately, it would provide a useful tool for precision agriculture by helping farmers detect growth problems of the crops. A multi-sheet is a thin, smooth, and translucent film used in agriculture fields to maintain the temperature and moisture of soil and is made of polyethylene, which is the same material as that from which plastic bags are manufactured, is barely biodegradable, and can cause problems not only for the natural environment but

also for the health of livestock and humans. The blue-sheet is made of the same material as the multi-sheet, but has a thick, rough, and blue-colored surface, which results in a difference in the spectrophotometry reflection characteristics of these two kinds of polyethylene products. Multi-sheet, blue-sheet, and metal pipes are materials that are often found in most open waste dumping sites, which means they have similar visual appearance and spectrophotometry reflection characteristics.



**Figure 6.1. Aerial image of the experimental field with the classification verification site marked by the red dotted line.**



**Figure 6.2. The ground objects at the study site: (a) Vegetation; (b) Dead/weakened vegetation; (c) Soil; (d) Multi-sheet and metal ; (e) Plastic blue sheet**

### 6.2.2 Data collection

Aerial surveys were conducted twice on August 1st, 2019. The lightweight UAVs and camera parameters used for both surveys are shown in **Figure 6.3** and **Table 6.1**. The Phantom 4 Pro (DJI) was used to obtain the RGB images of the study site, and the Inspire 2 (DJI) equipped with a multispectral sensor and a sunlight sensor Sequoia (Parrot) was used to obtain the multispectral images (green band, 510–590 nm; red band, 620–700 nm; red-edge band, 715–775 nm; near-infrared band, 750–830 nm). A 10000-mA mobile battery (Anker Power Core) was also attached to the Inspire 1 to power the multispectral sensor. Considering that the agriculture field had relatively simple ground objects and lacked the characteristic points that help match images, the flight route used for both aerial surveys was a double grid to ensure successful image processing.





**Figure 6.3. Unmanned aerial vehicles (UAVs) used for the aerial surveys:  
(a) Phantom 4 Pro (DJI); (b) Inspire 1 (DJI) with Sequoia (Parrot)**

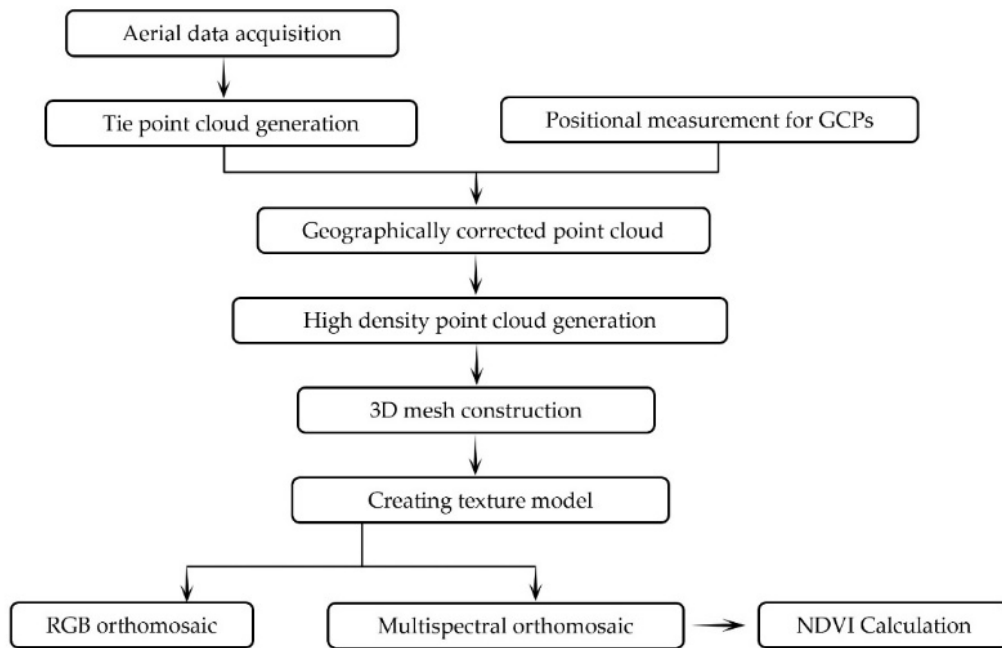
**Table 6.1. Unmanned aerial vehicle (UAV) and camera specifics**

	RGB Imagery	Multispectral Imagery
UAV model	Phantom 4 Pro (DJI)	Inspire 1 (DJI)
Total weight	1375 g	3400 g
Diagonal size	350 mm	581 mm
Maximum flight time	Approximately 30 min	Approximately 18 min
Camera type	1 inch CMOS	Multispectral Sensor
Image size	3840 × 2160 pixels	1280 × 960 pixels
Angle of view	84°	74°
Top overlap rate	80%	80%
Side overlap rate	80%	80%
Camera angle	75° from horizon	90° degrees from horizon
Flight height	50 m	40 m
Ground resolution	1.6 cm/pixel	6.2 cm/pixel

As shown in **Figure 6.1**, seven ground control points (GCPs) were selected within the experimental field. The position information of the seven GCPs was obtained by a Global Navigation Satellite System (GNSS) device Hiper V (TOPCON).

The Structure from Motion (SfM) technology can reconstruct the 3D structure of the object surface based on multiple, overlapping images taken by a moving camera. In the present study, the SfM process of the UAV images was conducted using Agisoft Metashape Professional Edition (ver. 1.8.0, Agisoft).

The image processing workflow is illustrated in **Figure 6.4**. After obtaining the aerial images using UAVs and importing them into the software, a tie point cloud was generated by aligning the images and finding the characteristic points existing in the overlapping areas between the images. Then, the position information of the GCPs obtained from the GNSS measurements was imported into the software and matched with the anti-aircraft signals in the images, which corrected the tie point cloud to the accurate geographic location. Based on the initial process results, a dense point cloud was generated based on depth maps calculated using dense stereo matching. Because generating the dense cloud was the most time-consuming step of the SfM process and that higher the density of the point cloud, the more complicated would be the subsequent calculations, in the present study, a medium quality dense cloud was generated. Based on the dense cloud information, a 3D polygonal mesh was constructed by connecting the points with polygonal surfaces. After the surface model was constructed, a texture model was created by extracting the RGB color value and calibrating the brightness and white balance, making the 3D model have the same visual appearance as that of the actual object. Finally, based on the texture model, the RGB and multispectral (red and near-infrared) orthomosaics were exported. The ground resolution of the final products of the SfM procedures was 1.6 cm for panchromatic and 4.2 cm for multispectral products. The NDVI raster was then calculated using the Raster Calculator geo-processing tool in ArcGIS Pro (ver. 2.4.1, Esri).



**Figure 6.4. Workflow for the Structure from Motion (SfM) process**

### 6.2.3 Classification procedures

#### i) NDVI Threshold Method

As mentioned in the introduction, the NDVI is an index mostly used to evaluate the health condition of plants. The higher the NDVI value, the healthier is the vegetation. Some objects other than plants also have specific NDVI values. The reflectance characteristics and the ranges of NDVI values of these objects have been discussed by many previous studies [34]-[39]. Although the NDVI values and spectral characteristic of the same object are various because of the differences in the used sensor or the ground resolution of the remote sensing data, there is an agreement that the dense and healthy vegetation has the NDVI value of more than 0.2 due to the extremely high reflectance of the near infrared band of light and the relatively low reflectance of the red light [40], and the NDVI value of the bare dry soil is around 0 due to the similar reflectance of the red light and the near infrared band of light [41]. Although the weakened vegetation has less chloroplast which leads to a lower reflectance of near infrared wave of light, the leaves are still conducting photosynthetic reaction. Therefore, the NDVI of the weakened or dead vegetation used in this study is lower than the normal vegetation but slightly higher than the bare soil. The plastic materials have different reflectance features due to the coating color or transmittance of light. However, the mean reflectance of red light (0.0375) from multiple plastic material is higher than the near infrared band of light (0.299), leading to a negative value of NDVI [42]. Same spectral features have been found on the commonly used metal such as Aluminum, iron and their alloys [43], [44]. Based on this characteristic of NDVI, the NDVI thresholds were used to classify the study area. The optimal significant figures of the NDVI threshold for the classification of ground objects have shown to be to the first decimal place, which was used in the NDVI threshold method in the present study (**Table 6.2**). The classification using this method was conducted within ArcGIS Pro (ver. 2.4.1, Esri). First, the NDVI raster was imported into the software. Then, the classes between the NDVI thresholds were extracted as independent raster layers using the Extract by Attributes geo-processing tool. To assign the attribute value for each class raster, the layers were processed using the Int tool, after which the vegetation layer was assigned the class number one, the soil layer as two, the dead/weakened vegetation layer as three, the multi-sheet and metal layer as four, and the blue-sheet layer as five. Additionally, the NDVI threshold of the blue-sheet class could not be defined since the NDVI value of the blue-sheet ranges from -0.1 to 0.1, which was included in both the soil class and the weakened vegetation class. Finally, the five layers were processed using the Mosaic to New Raster geo-processing tool, and a raster including the five classes of the entire study area was generated.

**Table 6.2. Normalized difference vegetation index (NDVI) threshold values for the different classes**

<b>Class</b>	Multi-sheet and Metal	Soil	Weakened Vegetation	Vegetation
<b>NDVI threshold</b>	-0.3 to -0.2	-0.2 to 0.0	0.0 to 0.2	0.2 to 1.0

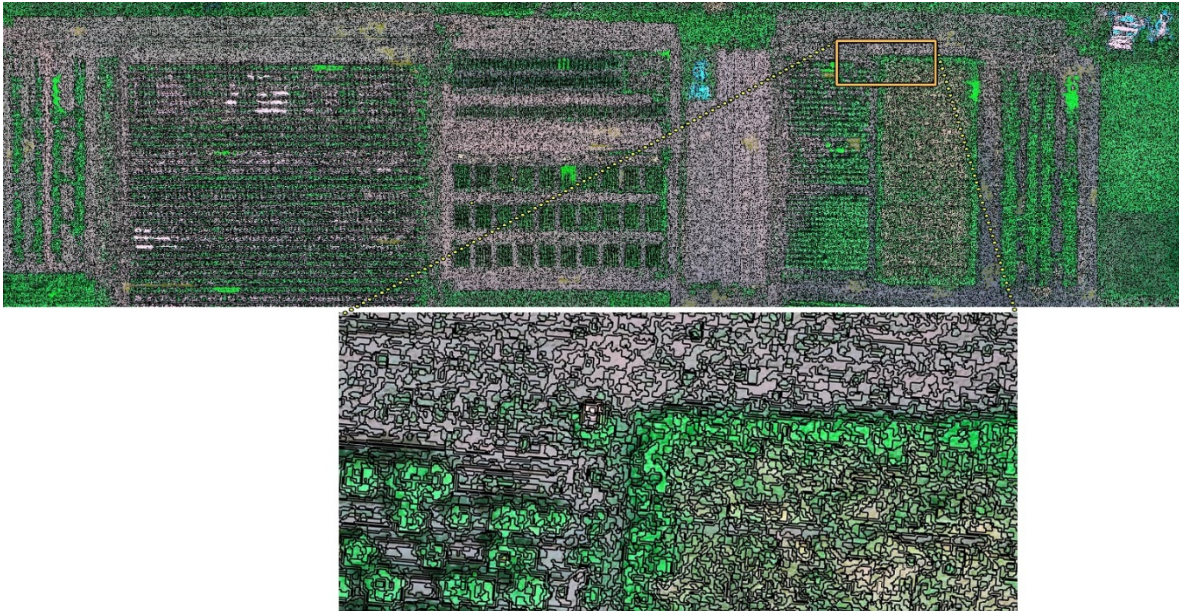
ii) RGB Image-based Machine Learning Method

The RGB image-based machine learning method uses the interactive Supervised Classification function of ArcGIS Pro. First, the RGB orthomosaic was input to the software, and a pyramid of the orthomosaic was built to achieve the optimal interactive performance. Next, five empty shape-file (polygon) layers for the classes (vegetation, soil, dead/weakened vegetation, multi-sheet and metal, and blue-sheet) were created and approximately 10–20 training samples for each class were manually distributed within the polygons. The number of training samples varied because the areas occupied by the different classes in the study area were not equal. To achieve the optimal classification result, all the training samples were determined at the pixel level, which means the error range was less than 2 cm. Therefore, although the required input data and operation steps for this method were simpler than those required for the NDVI threshold method, manual determination of the training samples was quite time-consuming. Finally, the maximum likelihood classification was performed on the orthomosaic layer of the study area based on the RGB values of the training samples.

iii) OBIA Method

The OBIA can classify the image objects by dividing the entire image into small segments according to their shape, size, and spectral content. The software used for this method was eCognition Developer (ver. 9.0, Trimble). First, a new project including the RGB orthomosaic, red band reflectance orthomosaic, near-infrared reflectance orthomosaic, and NDVI raster was created in the software, and was displayed as one RGB-mixed layer in the workspace, where the near-infrared was displayed as green and NDVI as red. Next, the mixed image was separated into multiple segments using the Multiresolution Segmentation tool. The scale factor, which decides the average size of the segments and is commonly set between 100 and 150 for high resolution UAV images [25], was set to 100 in the present study to obtain the classification result as precisely as possible. The result of segmentation is shown in **Figure 6.5**. Then, five classes were created inside the Class Hierarchy window and 80 to 200 segments for each class were selected as training samples using the Select Samples

tool. Finally, the classification was conducted according to the mean RGB value, mean brightness, standard deviation RGB, position, and shape of the mixed layer.



**Figure 6.5. Segmentation result (eCognition Developer 9.0, Trimble)**

#### 6.2.4 Accuracy evaluation of the classification methods

The accuracy assessments for the classification results of the three methods were performed with ArcGIS Pro. First, the orthomosaic and classification raster from the classification methods were input into the software. Next, a point shape-file with 1000 assessment points was created using the Creating Accuracy Assessment Point geo-processing tool (**Figure 6.6**).

The attribute table of the created point shape-file included both the Ground Truth field which is the reference value, and the Classification Field, which is the test value. The reference value was determined by visual judgement, by zooming into the point position and deciding manually what class the point belonged to. The visual judgement was also conducted at the pixel level, which means the tolerance of error was less than 2 cm. The test value was extracted from the classification raster using the Extract Values to Points geo-processing tool. Finally, the accuracy assessment for each classification result was conducted using the Compute Confuse Matrix geo-processing tool, by calculating the user's accuracy, the producer's accuracy, and the Kappa coefficient.



**Figure 6.6. One thousand assessment points used for the accuracy assessment of the classification results**

## 6.3 Results

### 6.3.1. UAV Mapping Products

**Figure 6.7** shows the RGB orthomosaic, red band orthomosaic, near-infrared orthomosaic, and NDVI raster generated from the UAV image, and the mixed RGB image in eCognition Developer, which were the photogrammetry products used for the subsequent classification. The characteristic of each product was the basis for the different performances of the three methods.

As shown in **Figure 6.7(a)**, In the RGB orthomosaic, the vegetation, multi-sheet and metal, and blue-sheet had characteristic RGB values that could be expressed clearly and brightly. However, the RGB values of soil and weakened vegetation were close to each other, resulting in a similar visual appearance. Specifically, the average RGB values of soil were 223, 209, and 190, respectively, whereas those of the weakened vegetation were 217, 204, and 174, respectively, for ten randomly selected sample pixels. This fact suggested that the RGB orthomosaic had a disadvantage in distinguishing soil and weakened vegetation.

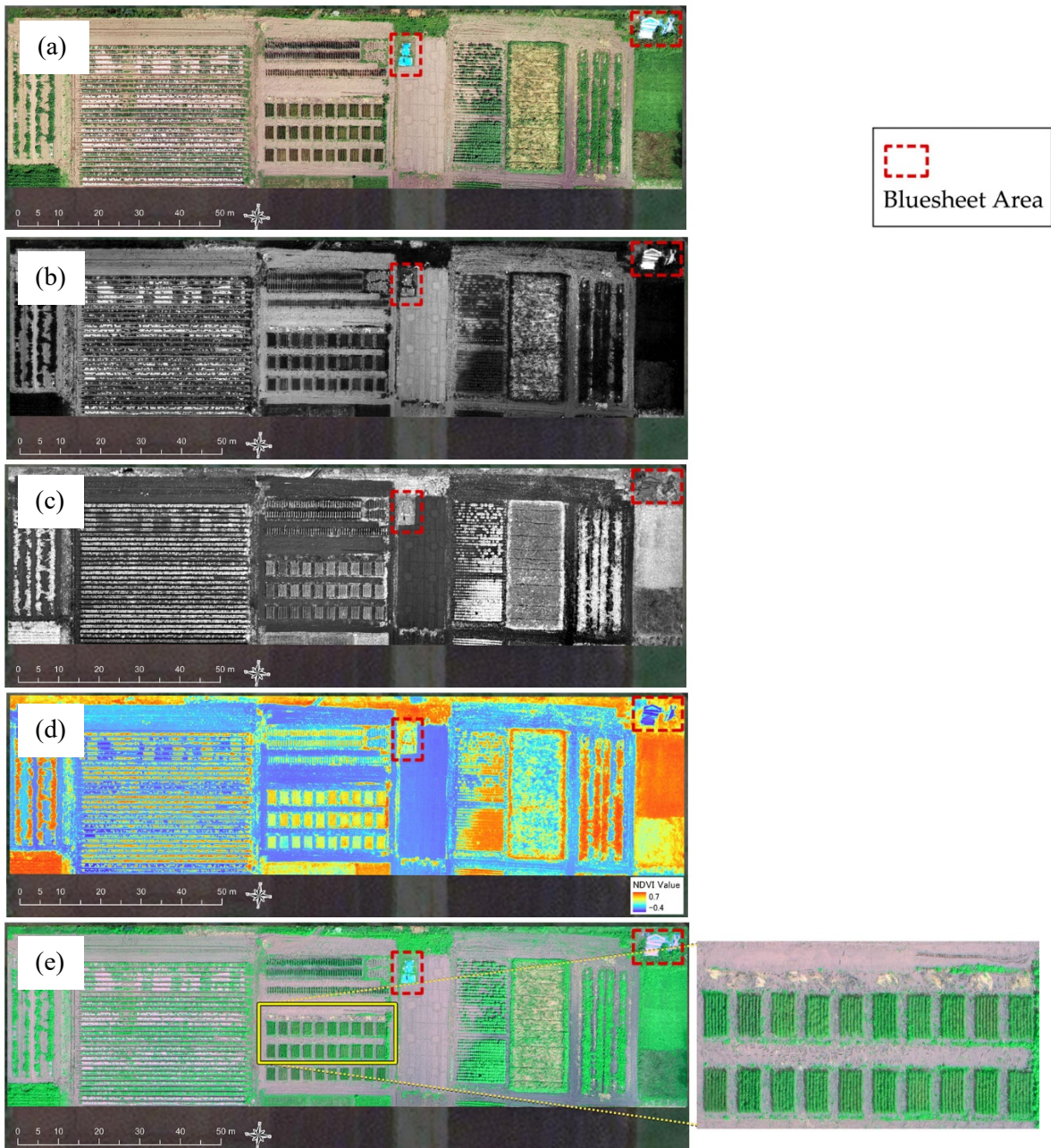
In contrast, as shown in **Figure 6.7(b)**, the red band orthomosaic could distinguish soil and weakened vegetation, but distinguishing between the weakened vegetation and the multi-sheet and metal was difficult because they all had a high reflectance rate of red light, as was distinguishing between the blue-sheet and soil because they both had an intermediate reflectance rate of red light.

As shown in **Figure 6.7(c)**, the vegetation area was clearly visible at the near-infrared orthomosaic, because the chlorophyll in healthy vegetation strongly reflects the near-infrared wavelength, and appears as fluorescence in the near-infrared image. Even for the weakened vegetation, a small amount of chlorophyll still produced a visible fluorescence. This fact makes the near-infrared band an important indicator for vegetation in the remote sensing field.

However, the objects other than vegetation have no significant reflectance characteristic at the near-infrared, which resulted in the similar appearance of soil, multi-sheet, metal, and blue-sheet in the near-infrared orthomosaic. Because NDVI is a normalized value of the difference between the reflectance of the red and near-infrared bands, the NDVI raster shows more features of different objects that have specific characteristics in terms of red or near-infrared band reflectance.

As shown in **Figure 6.7(d)**, the NDVI raster clearly distinguished between soil, vegetation, and multi-sheet and metal. However, the weakened vegetation and blue-sheet had similar intermediate NDVI values as that of soil because the former had a high reflectance at both the red and near-infrared bands, and the latter had a low reflectance at both bands. Based on these findings, the RGB and multispectral orthomosaics had both advantages and disadvantages for identifying different ground objects. Therefore, a mixed layer was prepared in eCognition Developer to maximize the strength of each kind of data. As shown in **Figure 6.6(e)**, different from the orthomosaic, the mixed layer clearly displayed the weakened vegetation, and different from the multispectral orthomosaics and NDVI, it also clearly displayed the objects with specific RGB values such as the blue-sheet.

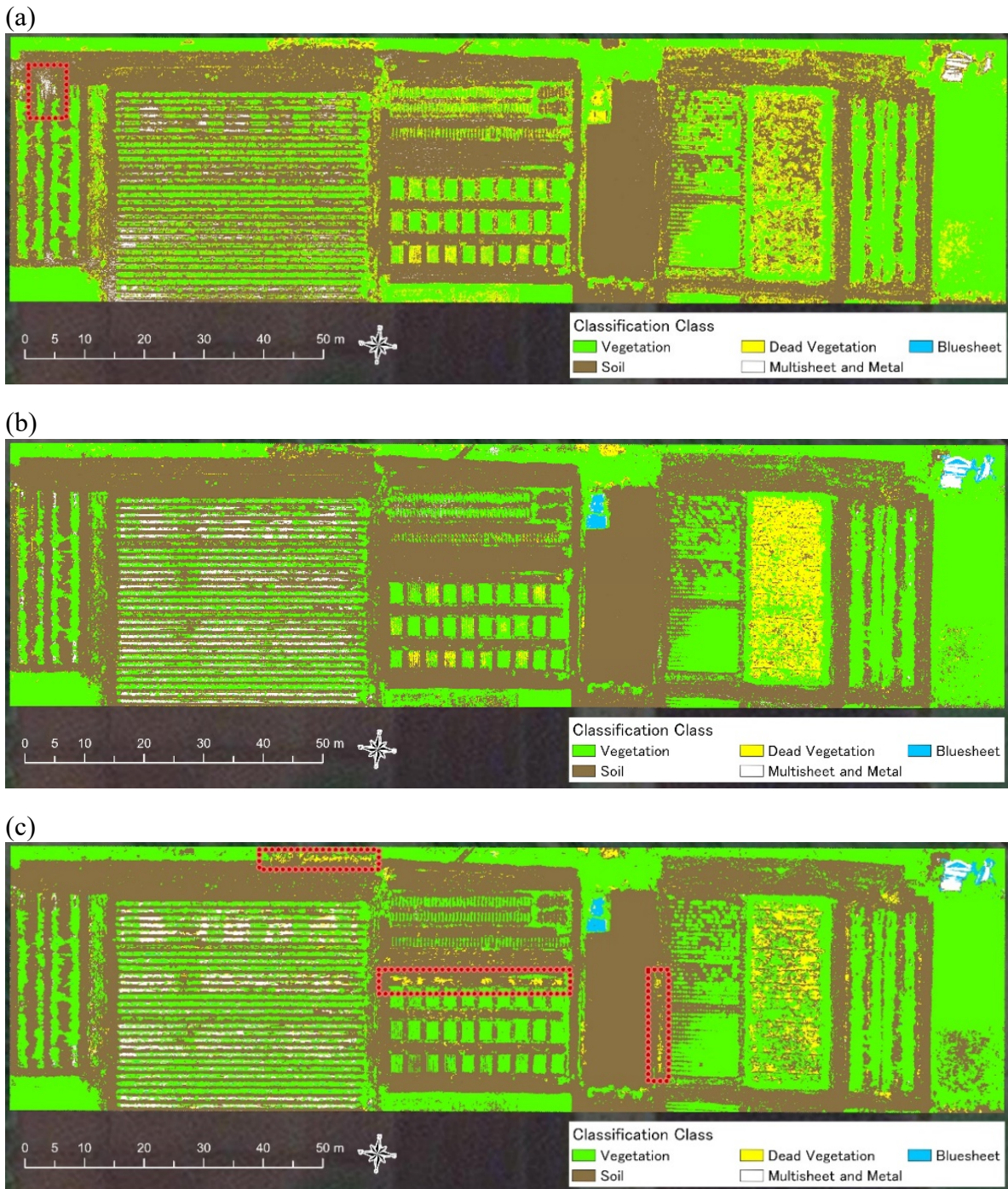




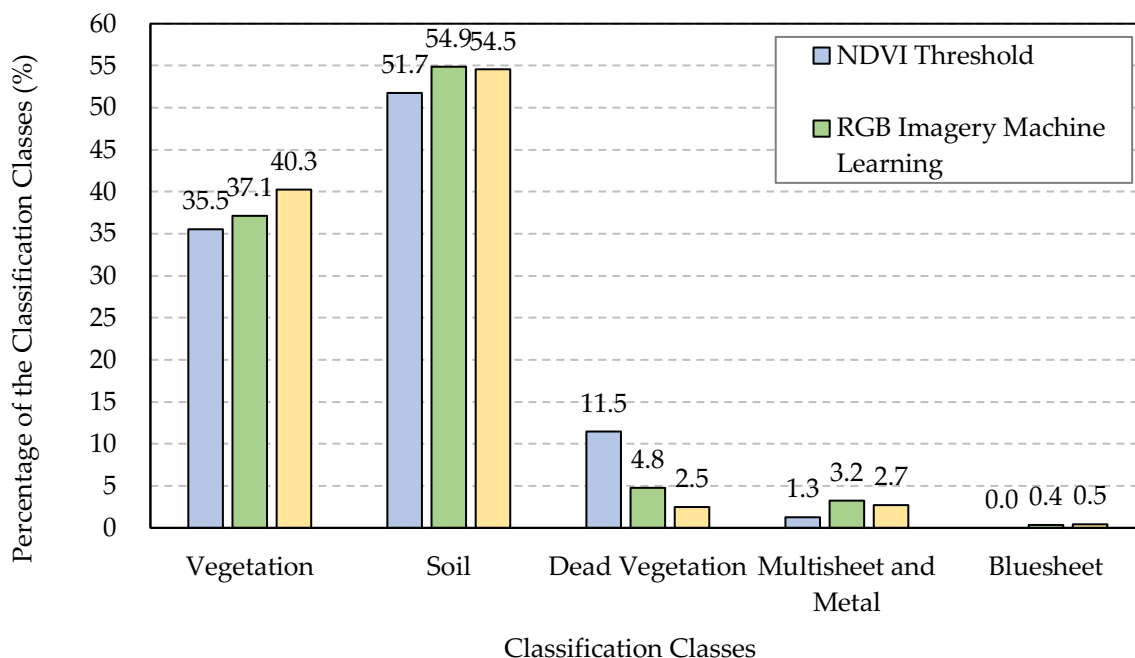
**Figure 6.7. Mapping products generated from the unmanned aerial vehicle (UAV) images: (a) Red-green-blue (RGB) orthomosaic; (b) Red band orthomosaic; (c) Near-infrared orthomosaic; (d) normalized difference vegetation index (NDVI) raster; (e) Mixed image in eCognition Developer**

### 6.3.2. Comparison of Classification Results

The classification results of the three methods are shown in **Figure 6.8**, and the Pixel percentage of the classes for each classification method is shown in **Figure 6.9**. Due to these results, the NDVI Threshold Method failed to identify the blue-sheets, and tend to classify the vegetation and soil as the weakened vegetation. In the opposite, the RGB Machine Learning Method classification result had the highest pixel percentage for the vegetation and the lowest pixel percentage for the weakened vegetation, showing the strength on identifying healthy vegetation and the weakness on identifying the weakened vegetation. On the other hand, as shown by the red square in **Figure 6.8(c)**, the OBIA method was able to identify the weakened vegetation which the RGB Machine Learning Method failed to recognize.



**Figure 6.8. Classification results: (a) Normalized difference vegetation index (NDVI) threshold method; (b) Red-green-blue (RGB) image-based machine learning method; (c) Object-based image analysis (OBIA) method**



**Figure 6.9. Pixel percentage of the classes for each classification method**

### 6.3.3. Accuracy Evaluation of the Classification Methods

The accuracies of the three methods were evaluated using the confusion matrix calculated with ArcGIS Pro. The confusion matrix (also known as error matrix) is a commonly used evaluation tool for classification verification. In the confusion matrix tables used in the present study, each row represents the classified results, whereas each column represents the reference results (the true value). For example, the first row of “Vegetation” in **Table 6.3** lists the values 279, 33, 6, 5, 5, and 328, which means that among all the 328 points that were classified as “Vegetation” by this method, 279 points were within the vegetation area of the study site, whereas 33 points were in the soil area, indicating they were misclassified. Similarly, the first column of “Vegetation” in **Table 6.3** lists the values 279, 6, 32, 0, 0, 317, meaning that among the 317 points that should have been classified as vegetation, only 279 points were correctly classified by this method, whereas six points were misclassified as soil. Three indicators were calculated based on the confusion matrix and are presented in Tables 4 to 6: the user’s accuracy, the producer’s accuracy, and the overall Kappa index. The user’s accuracy shows the false positive, meaning that the classification result was positive, whereas it should have been negative. For example, the user’s accuracy for “Vegetation” in **Table 6.3** was 0.851, meaning that among all the points that had been classified as vegetation by this

method, only 85.1% were correct. Similarly, the producer's accuracy shows the false negative, meaning that the classification result was negative, but the correct answer should have been positive. For example, the producer's accuracy for "Vegetation" in **Table 6.3** was 0.880, which means that among all the points that should have been classified as vegetation, only 88.0% was classified correctly by this method. The Kappa index, also known as Cohen's Kappa coefficient, is a statistical indicator used for conformance testing. The value of the Kappa index ranges between -1 and 1. The higher the Kappa index, the higher is the classification accuracy.

**Table 6.3(a)** presents the confusion matrix of the NDVI threshold method. The overall Kappa index of this method was 0.576, which is considered as "fair to good" [31]. The confusion matrix of the RGB image-based machine learning method is presented in **Table 6.3(b)**. The overall Kappa index of this method was 0.798, which is considered as "excellent". **Table 6.3(c)** presents the confusion matrix of the OBIA method. The overall Kappa index of this method was 0.793, which was close to that of the RGB image-based machine learning method and was also considered as "excellent".

**Table 6.3(a). Confusion matrix for the normalized difference vegetation index (NDVI) threshold method**

Class Name	Vegetation	Soil	Weakened Vegetation	Multi-sheet	Blue-sheet	Total	User_Accuracy	Kappa
Vegetation	279	33	6	5	5	328	0.851	
Soil	6	426	58	18	6	514	0.829	
Weakened vegetation	32	59	29	2	23	145	0.200	
Multisheet and Metal	0	6	1	6	0	13	0.462	
Bluesheet	0	0	0	0	0	0	0.000	
Total	317	524	94	31	34	1000	0.000	
Producer_accuracy	0.880	0.813	0.309	0.194	0.000	0.000	0.740	
Kappa								0.576

**Table 6.3(b). Confusion matrix for the red-green-blue (RGB) mage-based machine learning method**

Class Name	Vegetation	Soil	Weakened Vegetation	Multi-sheet	Blue-sheet	Total	User_Accuracy	Kappa
Vegetation	300	27	5	0	0	332	0.904	
Soil	11	486	50	7	0	554	0.877	
Weakened vegetation	4	10	36	0	0	50	0.720	
Multisheet and Metal	1	1	3	24	1	30	0.800	
Bluesheet	1	0	0	0	33	34	0.971	
Total	317	524	94	31	34	1000	0.000	
Producer_accuracy	0.946	0.927	0.383	0.774	0.971	0.000	0.879	
Kappa								0.798

**Table 6.3(c). Confusion matrix for the object-based image analysis (OBIA) method**

Class Name	Vegetation	Soil	Weakened Vegetation	Multi-sheet	Blue-sheet	Total	User_Accuracy	Kappa
Vegetation	311	43	21	6	0	381	0.816	
Soil	3	468	31	3	0	505	0.927	
Weakened vegetation	0	6	41	0	0	47	0.872	
Multisheet and Metal	2	5	1	21	1	30	0.700	
Bluesheet	1	2	0	1	33	37	0.892	
Total	317	524	94	31	34	1000	0.000	
Producer_accuracy	0.981	0.893	0.436	0.677	0.971	0.000	0.874	
Kappa								0.793

## 6.4 Discussion

As shown in **Figures 6.8(a)** and **6.9**, the NDVI threshold method could not detect the blue-sheet because it had the same NDVI value range as that of soil (-0.2 to 0.0). In addition, only a part of the multi-sheet in the field was successfully classified, whereas the remaining was classified as soil. This was because the multi-sheet had been installed in the field for more than two months by the time the aerial surveys were conducted, and the surface was covered by some soil or dust, which resulted in an NDVI close to that of soil. This result can also be observed in **Figure 6.8**. In the area surrounded by the red dotted line, soil was mistakenly determined as multi-sheet or metal. This was because the soil in that area had been stepped on by the surveyors, leaving behind footprints. The water content of the soil compacted by human weight was higher than that of the normal topsoil in the field, which decreased the NDVI value of the compacted area to a level lower than that of the threshold for multi-sheet and metal. This fact indicated that the NDVI value of various soils depends on the soil water content, and misclassification is possible when distinguishing soil and plastic or metal materials simply according to the NDVI threshold. Furthermore, the NDVI threshold method determined the vegetation edges to be weakened vegetation, although these parts were actually green leaves with good health, which can also be observed in **Figure 6.8**. This was because the ground resolution of the multispectral image was more than 6 cm, and the pixels at the edge of the vegetation had average NDVI values of both the vegetation and soil, which made them appear like the weakened vegetation. This suggested that despite the UAV multispectral image having a better ground resolution than the traditional aerial photos, there were still error values at the edge of the plant community. In contrast, as shown in **Figure 6.7(b)**, the RGB image-based machine learning method had a better performance than the former method. This method clearly detected the areas with blue-sheet, multi-sheet, and metal, and classified the compacted soil in the correct class despite the difference in soil water content. However, it still showed a disadvantage in detecting the weakened vegetation, because these areas had similar RGB values to those of soil, and the only standard for classification of this method was the RGB value. In contrast, as shown by the red dotted line in **Figure 6.7(c)**, the OBIA method successfully detected the area of the weakened vegetation which was misclassified by the former method. However, it still showed one disadvantage, which is the misclassification of some weakened vegetation as the normal vegetation class. **Figure 6.6** also reflects this trend of the OBIA method. This was because even though the plants belonged to the weakened vegetation class, the NDVI value might still be similar to that of the healthy vegetation when plant density is extremely high.

The NDVI Threshold Method achieved high accuracy in classifying vegetation and soil. The user's and producer's accuracies were above 0.80 for both classes. This suggested that the NDVI threshold was appropriate for identifying vegetation and soil. In contrast, the user's (0.200) and producer's (0.309) accuracies of the weakened vegetation class were both low. Furthermore, the user's accuracy was lower than the producer's accuracy, meaning that this

method had a tendency to falsely recognize other objects as weakened vegetation. Similarly, both the user's (0.462) and producer's (0.194) accuracies were low for the multi-sheet and metal class, and the user's accuracy was higher than the producer's accuracy. This means that the NDVI threshold method had a tendency to ignore the objects that should have been classified as multi-sheet or metal. Finally, both the user's and producer's accuracies were 0.000 for the blue-sheet class, meaning that the NDVI threshold method did not have the ability to identify the plastic material with a rough surface. Furthermore, a more precise threshold value for the classification can lead to a more accurate classification result. In this study and the previous studies, the threshold values were accurate to one decimal place. There is possibility that more specific discussions about the spectral signature of different objects can lead to a more accurate NDVI threshold value.

For the *RGB Machine Learning Method*, both the user's (0.904) and producer's (0.946) accuracies of the vegetation class were higher than 0.900, and both the user's (0.877) and producer's (0.927) accuracies were higher than 0.800, suggesting that this method had an extremely good performance in identifying vegetation and soil in this study area. The user's accuracy (0.720) of the weakened vegetation class was much higher than the producer's accuracy (0.383), meaning that the RGB image-based machine learning method tended to ignore the weakened vegetation. Similar to the observation and discussion presented in section 3.2, this result also demonstrated that this method had a disadvantage of mistakenly determining the weakened vegetation as soil. In contrast, both the user's (0.800) and producer's (0.774) accuracies of the multi-sheet and metal class were very high. Furthermore, the user's (0.971) and producer's (0.971) accuracies of the blue-sheet class were extremely high, meaning that this method could detect the plastic and metal materials with very high accuracy.

For the *OBIA Method*, similar to the former method, both the vegetation and soil classes had very high user's (0.816 and 0.927, respectively) and producer's (0.981 and 0.893, respectively) accuracies. The user's accuracy (0.872) was higher than the producer's accuracy (0.436) of the weakened vegetation class. This indicated that although the problem of ignoring the weakened vegetation also existed in the OBIA method, this method achieved a high accuracy at detecting the weakened vegetation, with the best performance among all the three methods. However, regarding the multi-sheet and metal and blue-sheet classes, the user's (0.700 and 0.892, respectively) and producer's (0.677 and 0.971, respectively) accuracies were lower than or equal to those of the former method, suggesting that although the OBIA could detect the plastic and metal materials with satisfactory accuracy, its performance was slightly inferior to that of the RGB image-based machine learning method. Additionally, in this study, the numbers of training sample for this method were limited to be consistent (on the pixel level) with the RGB imagery machine learning method for a better comparison. Higher classification accuracy can be achieved by using more training samples for both the RGB method and the OBIA method.



Based on these result, users of ground object classification such as societal stakeholders or researchers from different fields of agricultural and land resources, fisheries resources, forests, agroforestry, ecosystem services would have a clearer standard to decide the optimal classification methods to suit their requirements. Therefore, this study is thought to be helpful to the sustainable community development based on transdisciplinary integration of natural resource management systems. It is also important that community work together in the analysis of common UAV imagery to create transdisciplinary collaboration.

Integrated resource management are composed of multidisciplinary areas such as forests, agricultural lands, residential areas, lakes, marshes, and oceans that covers agricultural, land, water, forest, fisheries and tourism resources, agro ecology, protected areas, ecosystem-based approaches, human well-being, and integrated approaches for synergistic management of different resources. Although there has been many research dealing with resource management methods focusing on individual resources, there are not many research discussing evaluation methods that incorporate these resources represented by transdisciplinary approach in a cross-sectional manner. In addition to vegetation such as crops and trees, there are various objects such as plastics and metals wastes on the ground that are subject to resource management. Therefore, methods discussed in this study for ground object identification is expected to be an important indicator for societal stakeholders and researchers in employing UAVs identification methods for integrated resource management.

## **6.5 Conclusion of this chapter**

This study was conducted to see the applicability and accuracy of NDVI threshold, RGB Imaged based machine learning method and OBIA method using UAV for ground object identification. For this, vegetation, soil, weakened vegetation, blue-sheet, multi-sheet and metal were classified and accuracy of each method was determined.

According to the results of the study, the three classification methods discussed in the present study are based on different technical considerations and exhibited both advantages and disadvantages from certain perspectives.

1. According to the overall Kappa index, the RGB image-based machine learning method had the best performance in classifying all types of ground objects in the study area, whereas the OBIA method had a slightly lower overall accuracy and the NDVI threshold method had the lowest accuracy among the three methods.
2. On the other hand, considering practicality, the NDVI threshold method demands least input data which is only the NDVI raster of the field, and it was also the least time-consuming method and could provide an acceptable accuracy at determining the

vegetation, soil, plastic with smooth surface and the metal material, which made it a practical tool for land cover classification when a moderate accuracy was required.

3. Both the RGB image-based machine learning and OBIA methods were time- and labor-consuming owing to their requirement for precise training samples but had high accuracy classification results.
4. The RGB image-based machine learning method had better performance at detecting plastic and metal materials, which had bright RGB color, whereas the latter method had a higher accuracy at detecting the objects that were not very visually striking, such as the weakened vegetation.
5. The OBIA method had better performance at separating objects with similar RGB characteristics but different multispectral reflectance characteristics, such as the soil and the weakened vegetation.

As the conclusion of these results, at the field of agriculture and natural resource where vegetation and soil are the main objects for the classification, it is recommended to use the NDVI Threshold Method. It demands only the multispectral imagery data and has less requirement for the image analysis software and technique. At the field of rural or city environment management, where not only vegetation and soil but also the plastic and metal material are the main object for the classification, it is recommended to use the RGB Imagery Machine Learning Method. It only demands the RGB imagery data, and could achieve high accuracy with precise imagery analysis with the geographic information system software. Finally, when both the RGB and the multispectral imagery data are available, it is recommended to use the OBIA Method, which could achieve high accuracy at identifying different objects with the similar visual appearance.

The limitation of this study is that the categories of the ground objects used in this study were not comprehensive enough to cover every kind of object which can appear at the agricultural or rural area. With discussing the spectral characteristics of more objects, the optimal classification parameters such as the NDVI threshold value and the segmentation parameter for the OBIA method for more objects can be determined, which eventually leading to a higher classification accuracy.

### **Reference of this chapter**

1. Hunt Jr, ER, Daughtry CS. What good are unmanned aircraft systems for agricultural remote sensing and precision agriculture?. *Int J Remote Sens.* 2018;39(15-16):5345-5376.

2. Godfrey L, Nahman A, Yonli AH, et al. Africa waste management outlook. 2018. <https://stg-wedocs.unep.org/handle/20.500.11822/25514>.
3. Vongdala N, Tran H-D, Xuan TD, et al. Heavy metal accumulation in water, soil, and plants of municipal solid waste landfill in Vientiane, Laos. *Int J Environ Res Public Health*. 2018;16(1). doi:10.3390/ijerph16010022.
4. Wiedinmyer C, Yokelson RJ, Gullett BK. Global emissions of trace gases, particulate matter, and hazardous air pollutants from open burning of domestic waste. *Environ Sci Technol*. 2014;48(16):9523-9530.
5. Ferronato N, Torretta V. Waste mismanagement in developing countries: A review of global issues. *Int J Environ Res Public Health*. 2019;16(6). doi:10.3390/ijerph16061060.
6. Gutberlet J, Baeder AM. Informal recycling and occupational health in Santo André, Brazil. *Int J Environ Health Res*. 2008;18(1):1-15.
7. Andrady AL. Microplastics in the marine environment. *Mar Pollut Bull*. 2011;62(8):1596-1605.
8. Scarlat N, Motola V, Dallemand JF, Monforti-Ferrario F, Mofor L. Evaluation of energy potential of municipal solid waste from African urban areas. *Renew Sustain Energy Rev*. 2015;50:1269-1286.
9. Wilson DC, Rodic L, Modak P, et al. Global waste management outlook. (Wilson DC, ed.). UNEP; 2015. ISBN:9789280734799.
10. Steduto P, Hsiao TC, Raes D, et al. AquaCrop—The FAO crop model to simulate yield response to water: I. Concepts and underlying principles. *Agron J*. 2009;101(3):426-437.
11. Bausch WC, Neale CM. Crop coefficients derived from reflected canopy radiation: a concept. *Trans ASAE*, 1987;30(3):703-0709.
12. Silleos NG, Alexandridis TK, Gitas IZ, et al. Vegetation indices: advances made in biomass estimation and vegetation monitoring in the last 30 years. *Geocarto Int*. 2006;21(4):21-28.
13. Purevdorj TS, Tateishi R, Ishiyama T, et al. Relationships between percent vegetation cover and vegetation indices. *Int J Remote Sens*. 1998;19(18):3519-3535.
14. Hirata Y. Uses of high spatial resolution satellite data to forest monitoring. *J Jpn For Soc*. 2009;91(2):136-146.

15. Corradini F, Bartholomeus H, Lwanga EH, et al. Predicting soil microplastic concentration using vis-NIR spectroscopy. *Sci Total Environ.* 2019;650:922932.
16. Putra IPWS, Putra IKGD, Bayupati IPA, et al. Application of mangrove forest coverage detection in Ngurah Rai Grand Forest Park using NDVI transformation method. *J Theor Appl Inf Technol.* 2015;80(3):521.
17. Singh P, Javeed O. NDVI based assessment of land cover changes using remote sensing and GIS (A case study of Srinagar district, Kashmir). *SAFER.* 2020
18. Hashim H, Abd Latif Z, Adnan N. Urban vegetation classification with NDVI threshold value method with very high resolution (VHR) Pleiades imagery. *Int Arch Photogramm Remote Sens Spat Inf Sci.* 2019;42:237-240.
19. El-Gammal MI, Ali RR, Samra RA. NDVI threshold classification for detecting vegetation cover in Damietta governorate, Egypt. *Am J Sci.* 2014;10(8):108-113.
20. Hassan FM, Lim HS, Jafri MM. CropCam UAV for land use/land cover mapping over Penang Island, Malaysia. *Pertanika J Sci Technol.* 2011;19(S):69-76.
21. Hulet A, Roundy BA, Petersen SL, et al. Cover estimations using object-based image analysis rule sets developed across multiple scales in pinyon-juniper woodlands. *Rangel Ecol Manag.* 2014;67(3):318-327.
22. Jacquin A, Misakova L, Gay M. A hybrid object-based classification approach for mapping urban sprawl in periurban environment. *Landsc Urban Plan.* 2008;84(2):152-165.
23. Ventura D, Bonifazi A, Gravina MF, et al. Mapping and classification of ecologically sensitive marine habitats using unmanned aerial vehicle (UAV) imagery and object-based image analysis (OBIA). *Remote Sens.* 2018;10(9):1331.
24. Hamylton SM, Morris RH, Carvalho RC, et al. Evaluating techniques for mapping island vegetation from unmanned aerial vehicle (UAV) images: Pixel classification, visual interpretation and machine learning approaches. *Int J Appl Earth Obs Geoinf.* 2020;89:102085.
25. Shin JI, Seo WW, Kim T, et al. Using UAV multispectral images for classification of forest burn severity—A case study of the 2019 Gangneung forest fire. *Forests.* 2019;10(11):1025.
26. Natesan S, Armenakis C, Benari G, et al. Use of UAV-borne spectrometer for land cover classification. *Drones.* 2018;2(2):6.

27. Ahmed OS, Shemrock A, Chabot D, et al. Hierarchical land cover and vegetation classification using multispectral data acquired from an unmanned aerial vehicle. *Int J Remote Sens.* 2017;38(8-10):2037-2052.
28. Sarron J, Malézieux É, Sané CAB, et al. Mango yield mapping at the orchard scale based on tree structure and land cover assessed by UAV. *Remote Sens.* 2018;10(12):1900.
29. Brovkina O, Cienciala E, Surový P, et al. Unmanned aerial vehicles (UAV) for assessment of qualitative classification of Norway spruce in temperate forest stands. *Geo Spat Inf Sci.* 2018;21(1):12-20.
30. Yang B, Hawthorne TL, Torres H, et al. Using object-oriented classification for coastal management in the east central coast of Florida: A quantitative comparison between UAV, satellite, and aerial data. *Drones.* 2019;3(3):60.
31. Lanthier, Y., Bannari, A., Haboudane, D., Miller, J. R., & Tremblay, N. (2008, July). Hyperspectral data segmentation and classification in precision agriculture: A multi-scale analysis. In *IGARSS 2008-2008 IEEE International Geoscience and Remote Sensing Symposium* (Vol. 2, pp. II-585). IEEE.
32. Lebourgeois, V., Dupuy, S., Vintrou, É., Ameline, M., Butler, S., & Bégue, A. (2017). A combined random forest and OBIA classification scheme for mapping smallholder agriculture at different nomenclature levels using multisource data (simulated Sentinel-2 time series, VHRS and DEM). *Remote Sensing*, 9(3), 259.
33. Zheng, Y. Y., Kong, J. L., Jin, X. B., Wang, X. Y., Su, T. L., & Zuo, M. (2019). CropDeep: the crop vision dataset for deep-learning-based classification and detection in precision agriculture. *Sensors*, 19(5), 1058.
34. Fleiss JL, Cohen J, Everit, BS. Large sample standard errors of kappa and weighted kappa. *Psychol Bull.* 1969;72(5):323.
35. Sannigrahi, S., Basu, B., Basu, A. S., & Pilla, F. (2022). Development of automated marine floating plastic detection system using Sentinel-2 imagery and machine learning models. *Marine Pollution Bulletin*, 178, 113527.
36. Biermann, L., Clewley, D., Martinez-Vicente, V., & Topouzelis, K. (2020). Finding plastic patches in coastal waters using optical satellite data. *Scientific reports*, 10(1), 1-10.
37. Akbar, T.A.; Hassan, Q.K.; Ishaq, S.; Batool, M.; Butt, H.J.; Jabbar, H. Investigative Spatial Distribution and Modelling of Existing and Future Urban Land Changes and Its Impact on Urbanization and Economy. *Remote Sens.* **2019**, 11, 105.

38. Yacouba, D., Guangdao, H., & Xingping, W. (2009). Assessment of land use cover changes using NDVI and DEM in Puer and Simao counties, Yunnan Province, China. *World rural observations*, 1(2), 1-11.
39. Ehsan, S., & Kazem, D. (2013). Analysis of land use-land covers changes using normalized difference vegetation index (NDVI) differencing and classification methods. *African Journal of Agricultural Research*, 8(37), 4614-4622.
40. Govender, M., Chetty, K., & Bulcock, H. (2007). A review of hyperspectral remote sensing and its application in vegetation and water resource studies. *Water Sa*, 33(2), 145-151.
41. Yule, I., & Pullanagari, R. (2012). Optical sensors to assist agricultural crop and pasture management. In *Smart Sensing Technology for Agriculture and Environmental Monitoring* (pp. 21-32). Springer, Berlin, Heidelberg.
42. Sannigrahi, S., Basu, B., Basu, A. S., & Pilla, F. (2022). Development of automated marine floating plastic detection system using Sentinel-2 imagery and machine learning models. *Marine Pollution Bulletin*, 178, 113527.
43. Ramírez-Rincón, J. A., Ares-Muzio, O., Macias, J. D., Estrella-Gutiérrez, M. A., Lizama-Tzec, F. I., Oskam, G., & Alvarado-Gil, J. J. (2018). On the use of photothermal techniques for the characterization of solar-selective coatings. *Applied physics A*, 124(3), 1-9.
44. Kelley, C. S., Thompson, S. M., Gilks, D., Sizeland, J., Lari, L., Lazarov, V. K., ... & Dumas, P. (2017). Spatially resolved variations in reflectivity across iron oxide thin films. *Journal of Magnetism and Magnetic Materials*, 441, 743-749.

## Chapter 7 Conclusion and Recommendations

On completion of the discussion, the following conclusions can be drawn: first, to optimally practice direct georeferenced in farmlands, a lower aspect ratio of the GCP distribution is recommended to achieve better accuracy. When there are more than six available GCPs, the GDI is the proper factor to describe the GCP calibration ability. The higher the GDI, the higher the accuracy. According to the concept of GDI, the optimal distribution of GCPs can reduce the necessary number of GCPs to achieve a certain accuracy, and by which improve the efficiency of UAV photogrammetric surveys. After discussed the optimal way to geocalibrate the aerial products, we have developed a precise evaluation method for farmlands based on crop plant height, vegetation canopy cover, and vegetation index using UAV aerial images. At chapter 3, we verified and compared the commonly used DSM plant height method for different crops, and found out that: The DSM value should not be used to represent the plant height directly, but should use the regression model for different crops with special plant shapes. At chapter 4, we compared the DSM method and the point cloud method on estimating both plant height and above-ground canopy volume, and found out that: Point could provide more accurate plant height at specific position than DSM, However, when it comes to above ground biomass estimation, the two kinds of data provide the same performance. At chapter 5, we discussed the relationship between NDVI and canopy cover under different ground resolution, and found out that: There is a strong correlation between NDVI and canopy cover value, while the various materials other than vegetation and soil have a significant influence on their relationship, suggesting that identification of the ground objects is important when conducting precise evaluation of a farmland. And finally, at chapter 6, we compared three classification methods on identifying ground objects in the farmland, and found out that: The NDVI threshold methods is the most efficient, and both the RGB method and the OBIA method provide higher accuracy. These results are thought to contribute greatly to the development of the precise evaluation of the farmland. The novelty of these topics are: Developed an original index to evaluate GCP setting by both number and spatial distribution; Unraveled the reason for the deviation between DSM-derived plant height and reference value, and suggested method of moderation; Discussed the difference in restricting crop structure by different data types, and suggested the proper use for each method; Verified the linear correlation between NDVI and CC sensed by UAV under different resolutions and found out the error factor when monitoring vegetation index by UAV; and Applied the land-use classification methods on ground objects identification at farmland, and suggested the proper methods for identifying objects made from different materials.

By these results, we were able to answer the questions at the introduction. Finally, the results suggested by this research could be summarized as the integrated management flow chart. RGB imagery obtained by UAV could be used to construct DSM data and point cloud data, which are useful to monitor the crop status during the early growth stage by calculating

plant height or canopy volume. On the other hand, during the later growth stage, when the plant height stops to increase, the canopy cover and NDVI calculated by multispectral imagery obtained by UAV is more qualified for crop growth monitoring. Moreover, ground object identification discussed by this research could not only increase the accuracy when evaluating the crop status using canopy cover or NDVI, but also contribute to a better farmland management strategy and environment. This integrate management method for crop growth assessment and farmland management based on multiple kind of data types and analysis methods is thought to be the novelty of this research.



## Appendix

<b>Acronyms</b>	<b>Complete Expression</b>
UAV	Unmanned Aerial Vehicle
GPS	Global Positioning System
GCP	Ground Control Point
SfM	Structure from Motion
PPK	Post Processing Kinematic
RTK	Real Time Kinematic
GNSS	Global Navigation Satellite System
NRTK	Network Real Time Kinematic
GAM	Generalized Additive Model
RMSE	Root Mean Square Error
MAE	Mean Absolute Error
DEM	Digital Elevation Model
DSM	Digital Surface Model
GDI	GCP Distribution Index
STDEV	Standard Deviation
RMSPE	Root Mean Squared Percentage Error
JGD	Japanese Geodetic Datum
WGS	World Geodetic System
CSM	Crop Surface Model
PC	Point Cloud
DTM	Digital Terrain Model
NDVI	Normalized Difference Vegetation Index
CC	Canopy Cover
LAI	Leaf Area Index

FAO	Food and Agriculture Organization (of the United Nations)
ANCOVA	Analysis of Covariance
OBIA	Object-based Image Analysis
GEOBIA	Geographic Object-Based Image Analysis
AGH	Above Ground Height
GSD	Ground Sampling Distance